AD_____

AWARD NUMBER: DAMD17-02-1-0033

TITLE: Angiogenesis and Invasiveness in Prostate Cancer Detected with High Spectral and Spatial Resolution MRi

PRINCIPAL INVESTIGATOR: Greg Karczmar, Ph.D.

CONTRACTING ORGANIZATION: The University of Chicago
Chicago, IIllinois 60637

REPORT DATE: July 2006

TYPE OF REPORT: Final

PREPARED FOR: U.S. Army Medical Research and Materiel Command
Fort Detrick, Maryland 21702-5012

# REPORT DOCUMENTATION PAGE

*Form Approved*
*OMB No. 0704-0188*



| **1. REPORT DATE** *(DD-MM-YYYY)* | **2. REPORT TYPE** | **3. DATES COVERED** *(From - To)* |
|---|---|---|
| 01-07-2006 | Final | 24 Dec 2001 – 23 Jun 2006 |

**4. TITLE AND SUBTITLE**

Angiogenesis and Invasiveness in Prostate Cancer Detected with High Spectral and Spatial Resolution MRi

**5a. CONTRACT NUMBER**

**5b. GRANT NUMBER**
DAMD17-02-1-0033

**5c. PROGRAM ELEMENT NUMBER**

**6. AUTHOR(S)**

Greg Karczmar, Ph.D.

E-Mail: gskarczm@uchicago.edu

**5d. PROJECT NUMBER**

**5e. TASK NUMBER**

**5f. WORK UNIT NUMBER**

**7. PERFORMING ORGANIZATION NAME(S) AND ADDRESS(ES)**

The University of Chicago
Chicago, Illlinois 60637

**8. PERFORMING ORGANIZATION REPORT NUMBER**

**9. SPONSORING / MONITORING AGENCY NAME(S) AND ADDRESS(ES)**
U.S. Army Medical Research and Materiel Command
Fort Detrick, Maryland 21702-5012

**10. SPONSOR/MONITOR'S ACRONYM(S)**

**11. SPONSOR/MONITOR'S REPORT NUMBER(S)**

**12. DISTRIBUTION / AVAILABILITY STATEMENT**
Approved for Public Release; Distribution Unlimited

**13. SUPPLEMENTARY NOTES**

**14. ABSTRACT**

Background: We propose to develop new MR methods to improve early and accurate detection of prostate cancer, and guide treatment of the cancer. Although conventional MRI has high sensitivity, its specificity has been disappointing. New more specific and sensitive MRI methods would have a significant impact on clinical management of prostate cancer. Previous work in this laboratory showed that high spectral and spatial resolution (HiSS) MRI improves image quality and detection of the effects of contrast agents. HiSS images can be acquired with clinically acceptable run times by using frequency resolved echo planar methods to obtain detailed spectra of the water and fat resonances associated with each image voxel. We will test the hypothesis that: Contrast enhanced HiSS MRI increases sensitivity to angiogenesis and invasiveness of prostate cancer. As a result HiSS MRI can accurately distinguish metastatic from non-metastatic cancer based on detailed scans of the primary tumor.

**15. SUBJECT TERMS**
No subject terms provided

| **16. SECURITY CLASSIFICATION OF:** | | | **17. LIMITATION OF ABSTRACT** | **18. NUMBER OF PAGES** | **19a. NAME OF RESPONSIBLE PERSON** |
|---|---|---|---|---|---|
| **a. REPORT** | **b. ABSTRACT** | **c. THIS PAGE** | | | USAMRMC |
| U | U | U | UU | 71 | **19b. TELEPHONE NUMBER** *(include area code)* |

## Table of Contents

**INTRODUCTION:** The goal of this project was to develop and test a new approach to MR imaging which provides a much more comprehensive and accurate image, and therefore improves our ability to distinguish aggressive from non-aggressive lesions. The basis of the method is that it provides a large amount of new information, by detecting the detailed structure of the water signal that is used to produce all MR images. This information is not available in conventional MR images. We can use these new data to better define the edges and the internal structures of prostate tumors, to detect smaller lesions, and to get more detail about the blood supply of the tumor and if and how the tumor invades surrounding normal tissue.

To test this new method for imaging prostate cancer, we proposed two related sets of experiments:

- First, we proposed to use the new method to compare experimental animal models of prostate cancer that are metastatic (aggressive) with tumors that are not metastatic.
- Second, we proposed to test the method for imaging human prostate.

A summary of the statement of work is as follows:

**1. Develop high spectral and spatial resolution (HiSS) magnetic resonance imaging (MRI):** Improve speed of data acquisition and data processing.

**2. CAD (computer-aided diagnosis):** Use CAD methods to improve diagnostic utility of high spectral and spatial resolution data.

**3. Comparison of metastatic and non-metastatic rodent tumors:** Test ability of HiSS MRI combined with conventional MRI methods to distinguish between metastatic and non-metastatic rodent tumors.

**4. Comparison of HiSS and conventional MR imaging:** Determine whether HiSS has advantages relative to conventional imaging.

**5. Studies of orthotopic prostate tumors:** Use HiSS combined with conventional MRI to image orthotopic rodent tumors.

**6**. **Studies of human prostate cancer:** Determine whether HiSS produces useful images of human prostate.

**BODY:** During the no-cost extension period, we completed most of the specific aims of the proposal. We did the following work on each specific aim:

**SOW1**: HiSS was implemented on both research and clinical scanners. We developed new approaches to acquiring and processing spectral/spatial data that improve image quality and reduce artifacts. These approaches are described in published papers (see below) as well as manuscripts in progress.

**SOW2**. We worked with Dr. Jiang and his graduate student to apply neural network analysis to HiSS datasets. This resulted in improved separation of benign and malignant rodent prostate tumors. The work was presented at the RSNA.

**SOW3.** HiSS distinguished reliably between metastatic and non-metastatic rodent prostate cancer. This was described in a published paper (Fan et al, MRM, 2001).

**SOW4.** We demonstrated quantitatively that HiSS provides improved fat suppression and improved image contrast compared to conventional imaging. This work was published (see below).

**SOW5.** We used HiSS combined with conventional MRI to produce high quality images of orthotopically implanted rodent prostate cancer. During the final year of funding, we used HiSS to image 'naturally occurring' rodent prostate cancer in transgenic mice. To our knowledge, these are the first MR images of early rodent prostate cancer. We are currently pursuing use of this method to study natural progression of prostate cancer in this model.

The figure below shows the prostate of an approximately 20 week old mouse. The images are a series of different slices through the prostate and clearly discriminate the enlarged prostate from the surrounding other tissue types (red arrows). Green arrows point to abnormal tissue growth likely originating from the enlarged prostate.

**SOW6**. We produced the first images of the human prostate on a clinical 1.5 Tesla MRI scanner.

**KEY RESEARCH ACCOMPLISHMENTS:** Bulleted list of **key** research accomplishments emanating from this research

- We have demonstrated how to implement high resolution spatial/spectral imaging on clinical scanners 1.5 Tesla scanners and also a 4.7 Tesla research scanner for studies of animal models of prostate cancer.

On our 1.5 Tesla scanner we implemented a high spectral and spatial resolution protocol based on echo planar spectroscopic imaging. The pulse sequence was able to acquire data with spatial resolution of up to 750 microns in-plane in a 2 mm thick slice, and spectral resolution of up to 2.5 Hz.

On our 4.7 Tesla scanner we programmed an EPSI sequence that can acquire data with adequate signal-to-noise ratio at spatial resolution as high as 150 microns in-plane in a 500 micron thick slice, and spectral resolution of 5 Hz.

We are now working with laboratories at other institutions (UCSF, University of Arizona at Tucson, NIH) to help them implement this technology. We also have a research agreement with Philips Medical systems to implement routine clinical applications of this technology.

Details regarding the performance of the pulse sequence are provided in the attached manuscripts, especially Du et al (NMR in Biomedicine, 2005), Medved et al (Magnetic Resonance in Medicine, 2004), and Foxley et al (Manuscript in preparation, attached).

- We demonstrated that HiSS enhances the ability of MRI to distinguish between metastatic and non-metastatic lesions based on quantitative measures of image texture, sharpness of lesion boundaries, and contrast media uptake. Experiments were performed to evaluate use of high resolution spectroscopic imaging (SI) to discriminate between metastatic and non-metastatic rodent Dunning prostate tumors. SI datasets were obtained at 4.7 Tesla with in-plane resolution of 350-500 microns in a single 1.0 mm slice, and 6-8 Hz spectral resolution, before and after I.V.

injection of an iron oxide contrast agent. Images of water signal peak height in non-metastatic tumors were smoother in the tumor interior than images of metastatic tumors ($p < .004$ by T-test) before contrast media injection. This difference was stronger in contrast enhanced images ($p < .0004$). In addition, the boundary between the tumor and muscle was more clearly demarcated in non-metastatic than metastatic tumors. Combinations of image texture, tumor edge morphology, and changes in $T_2^*$ following contrast media injection improved discrimination between metastatic and non-metastatic tumors. (Details are provided in Fan et al, MRM, 2001; Fan et al, MRM, 2004)

- We obtained the first HiSS and conventional images of orthotopically implanted prostate cancer in mice and naturally occurring early prostate cancer in a transgenic mouse. This work demonstrated qualitative and quantitative advantages in HiSS images relatively to conventional MRI, including increased image texture, edge delineation, and sensitivity to contrast agents.

The most recent work – described in a manuscript in progress - involved early prostate cancer in transgenic mice. Simian virus large T antigen (SV40 TAg) transgenic mice with ages between 29 and 38 weeks were imaged using echo planar spectroscopic imaging (EPSI), gradient echo (GE), and spin echo (SE) pulse sequences. Water peak-height images produced from the maximum signal intensity of each small voxel's water spectrum from HiSS datasets showed greater mean signal and contrast-to-noise ratios ($41 \pm 9$ and $15 \pm 7$) than both GE ($21 \pm 7$ and $5 \pm 3$) and SE ($19 \pm 4$ and $8 \pm 4$) images over the segmented prostate. Water peak height images showed greater morphological detail in the prostate as determined by use of local binomial patter texture analysis. The borders of the prostate were more clearly delineated in HiSS images. The mean tumor area was measured and found to be smaller ($13.55 \pm 2.46$ mm$^2$) in younger mice ($30.3 \pm 2.3$ weeks) than in older mice ($25.02 \pm 10.57$ mm$^2$, $36.8 \pm 1.0$ weeks). The use of a partially deuterated water filled catheter inserted in the mouse rectum minimized the potentially prostate occluding blooming artifact in the PH image associated with the differing magnetic susceptibility between tissue and the air in the colon. The improved imaging metrics show that HiSS has potential for improving clinical imaging for the detection of human prostate cancer. This could aid in early detection, staging, and treatment design. This work is described in attached publications (Du et al, NMR in Biomedicine, 2005; Foxley et al, manuscript in progress).

- We obtained the first HiSS images of human prostate. These images were significantly improved relative to conventional MRI in terms of image contrast and fat suppression. The image below shows a HiSS water peak height image of normal human prostate.

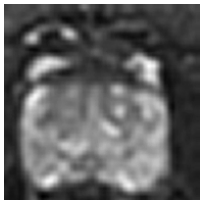

- Several ideas emanating from the research have been submitted for patents. This includes Fourier component imaging – a new approach to improving contrast in MR images. The invention proposes a new approach to MRI derived from our work on high spectral and spatial resolution imaging. We propose that images generated from Fourier Components of the water resonance in each small image voxel can provide important functional and anatomic information that can improve diagnostic accuracy. This work has been submitted as a provisional patent #60787446. More details concerning Fourier component imaging are in an attached paper (Medved et al, Magnetic Resonance in Medicine 2004).

**REPORTABLE OUTCOMES:**

**Published papers during the funding period that describe work supported entirely or partially by this funding:**

**New Publications on HiSS MRI supported entirely or in partby DAMD funding:**

1) W Du, YP Du, X Fan, MA Zamora, and GS Karczmar. Reduction of spectral ghost artifacts in high-resolution echo-planar spectroscopic imaging of water and fat resonances. Magn Reson Med, 49(6):1113-20, June 2003.

2) M Medved, W Du, MA Zamora, X Fan, OI Olopade, PM MacEneaney, G Newstead, and GS Karczmar. The effect of varying spectral resolution on the quality of high spectral and spatial resolution magnetic resonance images of the breast. J Magn Reson Imaging. 2003 Oct;18(4):442-8. Erratum in: J Magn Reson Imaging,18(6):750, Dec 2003.

3) M Medved, G Newstead, X Fan, W Du, Y Du, P MacEneaney, RM Culp, F Kelcz, O Olopade, M Zamora, G Karczmar. Fourier Components of Inhomogeneously Broadened Water Resonances in Breast: A New Source of MRI Contrast. Magn Reson Med **52:** 193-196 (2004).

4) X Fan, M Medved, JN River, M Zamora, C Corot, P Robert, P Bourrinet, M Lipton, RM Culp, and **GS Karczmar**. New model for analysis of dynamic contrast-enhanced MRI data distinguishes metastatic from nonmetastatic transplanted rodent prostate tumors. Magnetic Resonance in Medicine **51**:487-94, 2004.

5) W Du, X Fan, S Foxley, M Zamora, J River, R Culp, **GS Karczmar**. Comparison of high resolution echo-planar spectroscopic imaging with conventional MR imaging of prostate tumors in mice. NMR in Biomedicine **18:** 285 – 292, 2005.

6) W Du, GS **Karczmar,** S Uftring, YP Du. Anatomic and functional brain imaging using high resolution echo-planar spectroscopic imaging at 1.5 Tesla. NMR in Biomedicine **18:** 235 – 241, 2005.

7) X Fan, M Medved, S Foxley, JN River, M Zamora, **GS Karczmar**, C Corot, P Robert, P Bourrinet. Multi-slice dynamic contrast-enhanced MRI using P760 distinguishes between metastatic and non-metastatic rodent prostate tumors. MAGMA, **19**: 15 -21, 2006.

8) S Foxley, X Fan, S Hamad-Arkani, M Zamora, E Markiewicz, and Greg Karczmar. High spectral and spatial resolution improves MR images of early prostate cancers in SV40 Tag mice. Manuscript in progress

**Patent application:** Novel functional and anatomic contrast derived from Fourier Components of the water resonance. Provisional Patent #60787446

**Degrees obtained for work supported by this award;**

Weiliang Du, PhD. awarded December, 2003.

Sean Foxley, Ph.D. expected in 2007.

Sunny Arkani Hammed, M.A.; Ph.D. expected in 2008.

**Funding awarded based on work supported by this award**; Because of the success of the pilot work funded by this grant, applications for continued support from the NIH have been successful. An RO1 grant– supporting continued development of HiSS technology – has been funded by NIBIB - 1 R01 EB003108-01. An RO1 application to the NCI to support clinical evaluation of HiSS in women was also funded. A Shared Instrumentation grant for purchase of a 9.4 Tesla small bore scanner was funded. An R21/R33 proposal to pursue use of HiSS to image tumor angiogenesis was funded.

**Dissemination of HiSS Technology;** Several institutions are interested in HiSS technology as a result of our work in this area. These laboratories include Dr. Alan Koretsky's laboratory at NIH, Dr. Robert Gillies laboratory at the University of Arizona at Tucson, Dr. Fred Kelcz's mammography service at the University of Wisconsin, Madison, and Dr. Nola Hylton's group at the University of California at San Francisco. We are helping these groups to implement technology developed as part of this award.

**CONCLUSIONS:** We are grateful for the support of the Army Prostate Cancer Research program. This work has significantly advanced the development of a new approach to MRI that incorporates high resolution spectral information. The results of this work can be applied not only to detection of prostate cancer but also to breast cancer and other pathologies.

We have received funding from the NIH that will allow to continue this work. Thus we believe that the funding from the Army has successfully advanced this technology so that this research can receive long-term support from the NIH. In addition this method has been incorporated into many clinical scans at the University of Chicago on a research basis. We believe that this new technology will have significant benefits for patients.

NMR IN BIOMEDICINE
*NMR Biomed.* 2005;**18**:285–292
Published online 22 June 2005 in Wiley InterScience (www.interscience.wiley.com). DOI:10.1002/nbm.954

# Comparison of high-resolution echo-planar spectroscopic imaging with conventional MR imaging of prostate tumors in mice

**Weiling Du, Xiaobing Fan, Sean Foxley, Marta Zamora, Jonathan N. River, Rita M. Culp and Gregory S. Karczmar***

Department of Radiology, University of Chicago, Chicago, IL 60637, USA

*Received 27 September 2004; Revised 20 December 2004; Accepted 21 December 2004*

ABSTRACT: High spectral and spatial resolution (HiSS) MRI of rodent tumors has previously been performed using conventional spectroscopic imaging to obtain images with improved contrast and anatomic detail. The work described here evaluates the use of much faster echo-planar spectroscopic imaging (EPSI) to acquire HiSS data from rodent tumor models of prostate cancer. A high-resolution EPSI pulse sequence was implemented on a 4.7 T Bruker scanner. Three-dimensional EPSI data were Fourier-transformed along the *k*-space and temporal (free-induction decay) axes to produce detailed water and fat spectra associated with each small image voxel. The data were used to generate images of spectral parameters, e.g. peak-height images for each small voxel. Two variants of EPSI were performed; gradient-echo or spin-echo excitation with EPSI readout. These imaging methods were tested in commonly used rodent prostate cancers, including seven mice implanted with non-metastatic AT2.1 ($n = 3$) and metastatic AT3.1 ($n = 4$) prostate tumors on the hind leg, and 10 mice implanted with LNCaP prostate cancers *in situ*. The peak-height images derived from EPSI datasets provide more detailed tumor anatomy, improved signal-to-noise and contrast-to-noise ratios compared with the gradient-echo or spin-echo images at all echo times. The results suggest that HiSS MRI data from small animal models of prostate cancer can be acquired using EPSI, and that this approach improves imaging of heterogeneous tissue and vascular environments inside the tumors compared with conventional MR techniques. Copyright © 2005 John Wiley & Sons, Ltd.

KEYWORDS: prostate cancer; MRI; echo-planar spectroscopic imaging; tumor; mouse; spectral/spatial imaging

## INTRODUCTION

Prostate cancer is the second leading cause of cancer death in men following lung cancer.[1] With development of better technology, MRI has increasingly been used for its diagnosis. Prostate cancer is usually detected in MR images based on $T_2/T_2^*$ contrast.[2] Malignancy is seen as an island of low signal intensity surrounded by high signal intensity from benign peripheral tissue.[3] However, $T_2$-weighted MR images require a long echo time (*TE*), in order to obtain sufficient contrast between the tumor and surrounding normal tissues. The resulting low signal-to-noise ratio (SNR) and loss of image definition impede early detection, accurate measurement of tumor volume and the characterization of tumor invasiveness.[4]

To improve the morphological imaging of prostate cancers, various MR techniques have been proposed.[5–7] Recently, diffusion MRI has been demonstrated to increase tumor-to-normal tissue contrast in rodents[8] and humans,[9] compared with $T_2$-weighted MRI. An alternative approach is to use high resolution spectroscopic imaging methods, i.e. sampling the free-induction decay (FID) to produce a detailed proton spectrum of water and fat for each voxel to obtain improved functional and anatomic images. Very high spatial resolution is possible using EPSI because the water and fat resonances are imaged, rather than the relatively low concentrations of metabolites that are more common targets for spectroscopic imaging.[11,17,23] Sarkar *et al*. have successfully used echo-planar spectroscopic imaging (EPSI) to improve anatomic imaging of the human pelvis and joints.[11] Work from this laboratory demonstrated improved anatomical and functional imaging of rodent tumors[12–15] and human breast[16–18] with high spectral and spatial resolution (HiSS).[19,20] Yang *et al*. demonstrated that both SNR and $T_2^*$ contrast can be increased in MR images of cerebral

**Correspondence to:* G. S. Karczmar, University of Chicago, Department of Radiology, MC2026, 5841 S. Maryland Ave, Chicago, IL 60637, USA.
E-mail: gskarczm@uchicago.edu
*Contract/grant sponsor:* National Cancer Institute; *contract/grant number:* 1 R21 CA089408.
*Contract/grant sponsor:* Department of Defense; *contract/grant number:* DAMD17-02-1-0033.

**Abbreviations used:** gEPSI, gradient echo excitation EPSI readout pulse sequence; sEPSI, spin echo excitation EPSI readout pulse sequence; HiSS, high spectral and spatial resolution; CSI, conventional spectroscopic imaging; PH, peak–height; PF, peak–frequency.

vasogenic edema and brain functional activity, by using a variant of EPSI.[10]

Although HiSS EPSI has been shown to work well for imaging patients on whole body scanners, requirements for small animal imaging are somewhat different. Much higher spatial resolution is typically required and, since small animals are generally imaged at high field, limited spectral bandwidth can be a problem. Previous HiSS images of rodent tumors were acquired using conventional spectroscopic imaging with long run times and/or limited spatial resolutions.[12,13] The purpose of the work reported here was to implement and evaluate high spectral and spatial resolution MRI using EPSI[21,22] in small animal models. Commonly used rodent tumor models of prostate cancer were imaged at 4.7 T. Specifically, HiSS images of prostate tumors implanted in the hind legs of nude mice were compared with gradient-echo (GRE), spin-echo (SE), and high resolution conventional spectroscopic imaging (CSI) images. In addition, carcinomas surgically implanted in the prostates of nude mice were imaged.

## MATERIALS AND METHODS

### Animal preparation

All procedures were performed according to protocols approved by the Institutional Animal Care and Use Committee and were in compliance with the Animal Welfare Act and NIH Guide for the Care and Use of Laboratory Animals. Non-metastatic AT2.1 ($n = 3$) or highly metastatic AT3.1 ($n = 4$) Dunning R-3327 rat prostate tumor cells were implanted subcutaneously in the hind limbs of nude mice. LNCap-C4-2 ($n = 10$) metastatic human prostate cancer cells were surgically implanted in the prostate glands of nude mice. Tumors were imaged approximately 2 weeks after inoculation with diameters ranging from 0.3 to 0.8 cm.

### MRI

During the MR experiments, mice were anesthetized with 2% isoflurane gas mixed with medical air (2 l/min) and oxygen (0.2 l/min) delivered through a mask. The temperature of mice bearing leg tumors was maintained by blowing warm air into the bore of the magnet and measured with a rectal temperature probe (Fisher Scientific, Springfield, NJ, USA). Mice bearing prostate tumors *in situ* were laid supine in a cradle and then put into a 'body' coil. All mice were immobilized on a Plexiglas board with vet wrap and tape.

Imaging was performed with a 33 cm horizontal bore, 4.7 T MR scanner (Omega; GE/Bruker, Fremont, CA, USA) with 20 cm bore self shielded gradient coils (maximum gradient strength 100 mT/m). Birdcage coils were used for excitation and detection for tumors implanted in the leg and *in situ*. After scout images were obtained and the tumor location was determined, a localized shim was performed on a single 3 mm slice through the tumor. This yielded a water resonance from the slice with a linewidth of 60–100 Hz. A 1 mm thick slice was chosen in the middle of the shimmed slice for subsequent EPSI and conventional MRI imaging.

**EPSI.** Two variants of the EPSI pulse sequence were implemented: gradient-echo or spin-echo excitation with EPSI readout, referred to as gEPSI and sEPSI, respectively. The two EPSI sequences are identical except with respect to the excitation of the first echo of the gradient recalled echo train. A slice-selective 'soft' 90° RF pulse and a non-selective 'hard' 180° RF pulse were used in sEPSI, while a single RF pulse at the Ernst angle was used in gEPSI. The matrix size was 128 in the readout direction, and either 128 or 256 in the phase-encoding direction. This allowed for in-plane resolution of $\sim$200 μm in the readout direction and $\sim$200 or $\sim$100 μm in the phase-encoding direction over a $\sim$24 mm field-of-view (FOV). The spectral data was collected using an oscillating 32 lobe gradient echo train in the readout direction for each step of phase encoding. The echo time (*TE*) for the first echo in the echo train was 7 ms for gEPSI and 11 ms for sEPSI. The longer *TE* for sEPSI was necessary because of the inclusion of the 180° pulse and spoiling gradients placed symmetrically around it. The repetition time (*TR*) was 1 s for both EPSI sequences, resulting in a total acquisition time of 2 min or 4 min per acquisition (for 128 or 256 phase encoding steps, respectively). Reconstruction of spectral/spatial data (described elsewhere[17]) resulted in water spectra with resolutions of 7.4 Hz and bandwidths of 237 Hz in each voxel. The modulus water spectra were quantified to form various spectral parameter images. For example, the peak-height (PH) image was generated using the highest spectral intensity in each voxel.

**Conventional imaging.** GRE, SE and CSI images were obtained through the same 1 mm slice, at the same spatial resolution, and with the same FOV as in both types of EPSI images. $T_2/T_2^*$ weighting in GRE and SE images were varied by starting with *TE*s of 7 and 11 ms, respectively, and then incrementing *TE* by 4.2 ms for each subsequent scan until a maximum *TE* of 41 ms was reached. *TR* was 1 s for all GRE and SE images. CSI with phase encoding in both spatial dimensions was performed with a receiver bandwidth of 1000 Hz and spectral resolution of 7.8 Hz. The acquisition time for CSI was 38 min with a matrix size of $128_x \times 128_y \times 128_{\text{frequency}}$ and a *TR* of 140 ms. Image processing and data analysis was performed using IDL software (Research Systems Inc., Boulder CO, USA).

## RESULTS

### Comparison of GRE and SE with EPSI

Figure 1 shows two GRE (a1, a2) and SE (b1, b2) images with varying *TE*s (11 and 41 ms, respectively), a proton-density weighted image (c1) taken from the first echo of an sEPSI acquisition, and a sEPSI PH image (c2). The gradient echo images have higher SNR at short *TE* (a1) than at longer *TE* (a2), but poorer contrast both inside the tumor and between the tumor and the surrounding muscle. The spin echo images have poorer contrast at short *TE* (b1) than at long *TE* (b2) between the tumor and the surrounding muscle, but under both conditions show relatively poor contrast in the tumor compared with the GE images. Moreover, the SNR in both SE images are lower than in either of the GE images. The sEPSI images have improved SNR and contrast compared with both GRE and SE images. This results in improved anatomic detail and texture. Further information can be retrieved from the sEPSI dataset using the first echo in the EPSI dataset to produce an approximately proton-density weighted image. For example, improved delineation of the top of the tumor, which appears dark in the sEPSI PH image owing to short $T_2^*$, but can be visualized using the first echo image. Alternatively, the FID in each voxel can be filtered to emphasize early echoes.

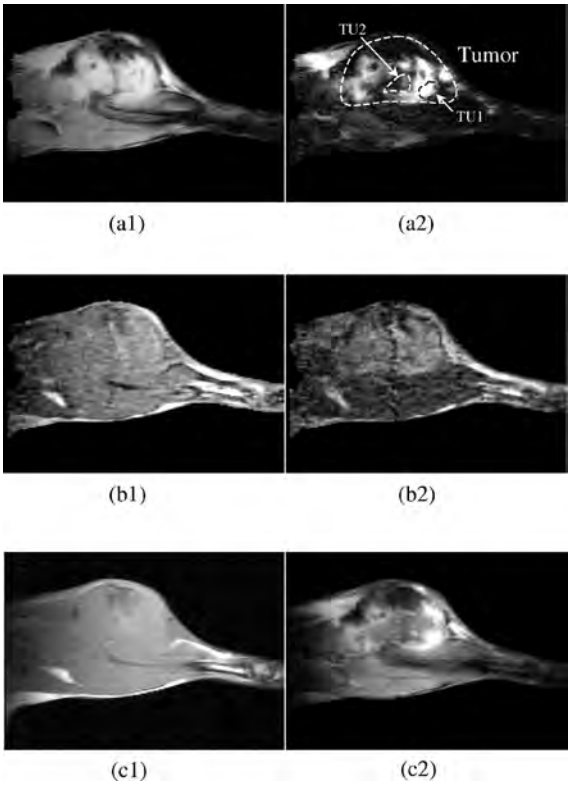


**Figure 1.** Sagittal images of the hind leg of a mouse implanted with an AT3.1 prostate tumor. Top: GRE images acquired at $TE = 11$ ms (a1) and 41 ms (a2); middle: SE images acquired at $TE = 11$ ms (b1) and 41 ms (b2); bottom: sEPSI first echo image (c1) and sEPSI PH image (c2). All images were obtained with $TR = 1$ s

Quantitative comparison between sEPSI images and GRE images supports the subjectively observed increases in both SNR and CNR in EPSI. SNR is calculated in a tumor ROI ('TU1' in Fig. 1) and CNR is calculated from two tumor ROIs ('TU1' vs 'TU2' in Fig. 1). As would be expected, the maximum SNR of $53 \pm 7$ occurred in gradient echo images with the shortest *TE*: 7 ms. The SNR in the representative sEPSI PH image shown in Fig. 1 is $78 \pm 6$. A maximum CNR of $39 \pm 11$ occurred in the GRE image at a *TE* of 11 ms; the CNR is $65 \pm 8$ in the sEPSI PH image. These differences in SNR or CNR between the sEPSI PH image and the GRE images are much greater than the noise.

### Comparison of EPSI with CSI

The HiSS images obtained with gEPSI and with its slower counterpart, CSI, show very similar contrast between the tumor and normal tissues (left and right columns of Fig. 2, respectively). Measured over tumor and muscle ROIs in Fig. 4(b) ('TU1' and 'M', respectively), the ratio between averaged tumor intensity and average muscle intensity is $2.67 \pm 0.28$ in the gEPSI PH image and $2.38 \pm 0.23$ in the CSI PH image. The SNR in the tumor region-of-interest (ROI) is $72.0 \pm 6.3$ in the gEPSI PH image and $78.4 \pm 5.0$ in the CSI PH image (SNR values and ratios reported are mean $\pm$ standard deviation).

Figure 2 also compares the spectra of water and fat obtained with gEPSI and CSI. Spectra were selected from six representative voxels: 'P1', 'P2' and 'P3' are from muscle, femur and the interface between muscle and skin; 'P4', 'P5' and 'P6' are from tissue inside the tumor, a vasculature network inside the tumor and the tumor rim, respectively. The gEPSI spectra generally resemble the CSI spectra: they provide similar resonance frequencies and linewidths. This is further supported by peak frequency (PF) maps in Fig. 3 (a, CSI; b, gEPSI). The two maps show similar variations of peak frequency location across the leg and tumor as determined by the water peak in the spectrum from each voxel. This is indicative of variations in $B_0$ across the imaging plane. Because the spectra were limited to a finite number of bins, changes in PF greater than approximately $\pm 122$ Hz are subject to fold-back along the frequency axis. This leads to sudden transitions from bright to dark, particularly at the edges of the leg where there are large frequency changes. Close examination of the peak frequency images shows intensity variations at the rim of the tumor, as well as subtle features that may correspond to blood vessels. These features presumably reflect differences in magnetic susceptibility between tumor, blood and normal tissue.

Advantages of the CSI spectra over the gEPSI spectra are noticeable. The larger bandwidth (1000 Hz in CSI vs

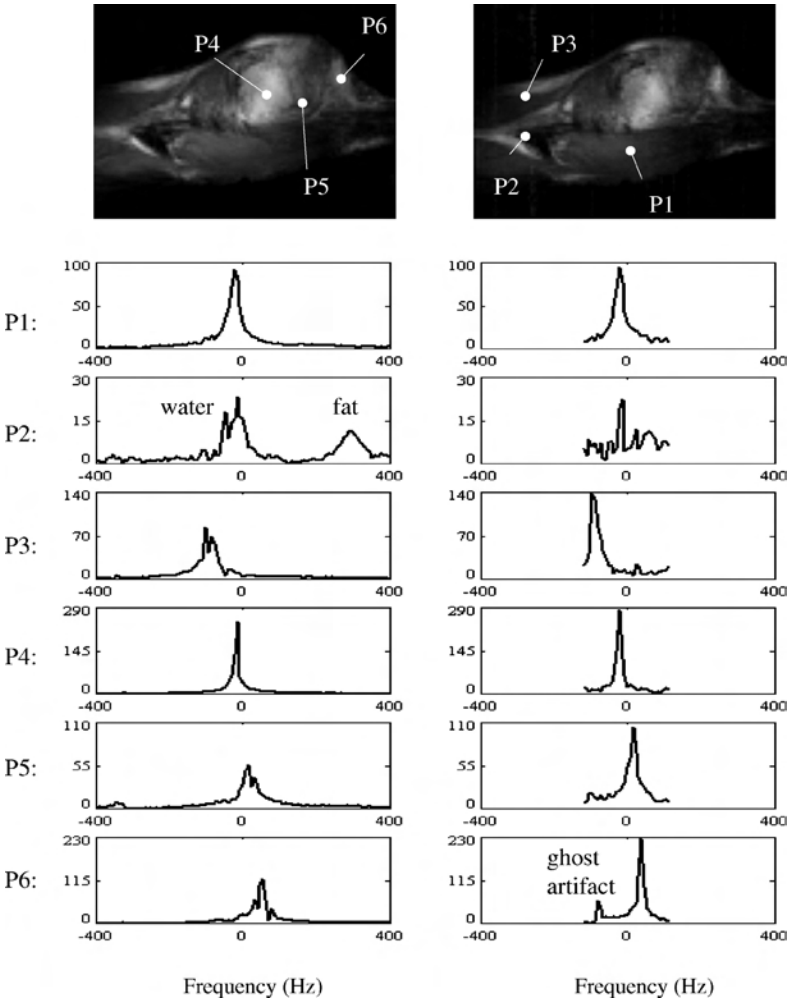


**Figure 2.** PH image and selected spectra obtained from phase-encoded CSI (left column), or from EPSI (right column). Spectra are selected from three points (P1, P2, P3) outside the tumor and three points inside (P4, P5) or on the edge (P6) of the tumor

237 Hz in gEPSI) is desirable for separating the fat and water resonances (see the CSI spectrum at 'P2'). Aliasing due to the limited bandwidth in gEPSI spectra can sometimes cause distortion in the spectral line shape (e.g. gEPSI spectrum at 'P2'). Details of the water proton spectra are clearly visible in the CSI spectra. For example, the CSI spectra at 'P5' and 'P6' show resolved components, which may reflect intravoxelar inhomogeneity of magnetic susceptibility due to tissue and/or vascular compartmentation. These features are not

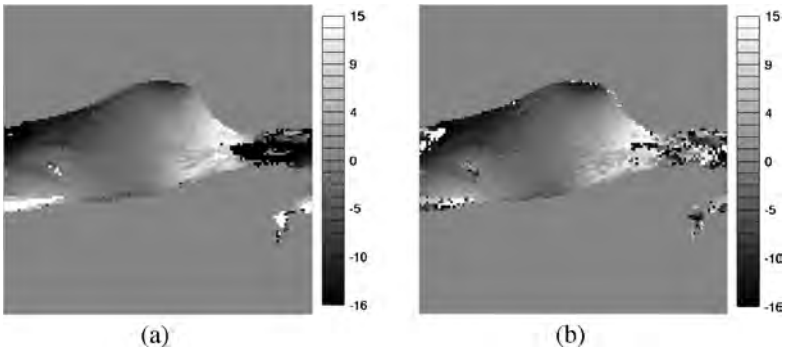


**Figure 3.** Peak frequency images derived from (a) CSI and (b) gEPSI acquisitions for the tumor shown in Fig. 2. Each step is 7.4 Hz

 

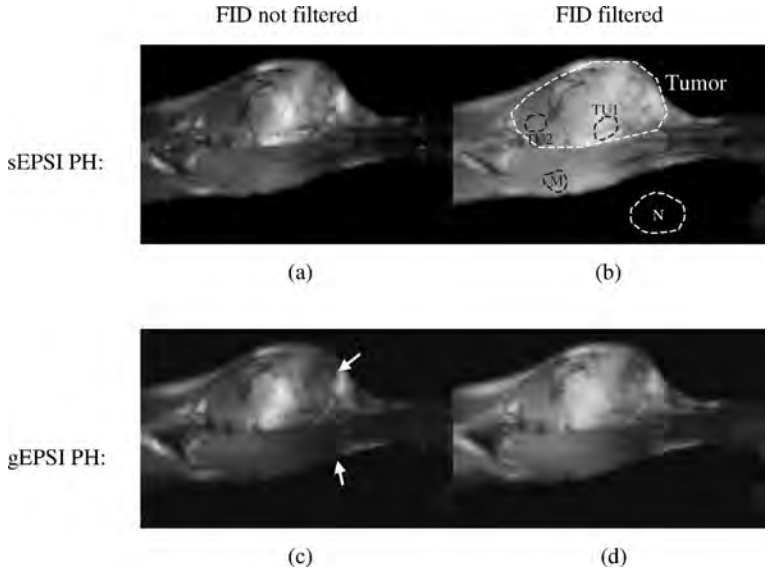


**Figure 4.** EPSI PH images of the right hind leg of a mouse bearing an AT3.1 prostate tumor. Images were obtained with a sEPSI pulse sequence (upper row) or a gEPSI pulse sequence (lower row), and without (left column) or with (right column) filtering the FIDs to improve SNR. Labeled regions in (b) were used for the measurements of SNR and CNR in these images, in particular, 'TU1' for a high intensity area in the tumor, 'TU2' for an intermediate intensity area in the tumor, 'M' for surrounding muscle, and 'N' for the noise background

clearly depicted in the corresponding gEPSI spectra. This may be due to eddy currents generated by the time dependent gradients that are turned on during the FID. There are residual ghost artifacts in some gEPSI spectra (e.g. in P6), even after a post-processing algorithm was applied[24] to correct for them. Their presence in the gEPSI spectra impedes accurate quantitation of the true water resonance.

## gEPSI and sEPSI

PH images generated with sEPSI and gEPSI are compared in Fig. 4. The two PH images obtained without filtering the FIDs [Fig. 4(a) and 4(c)] are highly $T_2^*$-weighted, with high intensity in a portion of the tumor and in the skin, compared with the neighboring muscle tissues. Networks of vessels inside the tumor are clearly depicted in both images. The image contrast between different areas inside the tumor and between the tumor and muscle, for example, is higher in the gEPSI PH image than in the sEPSI PH image. On the other hand, local $B_0$ field inhomogeneities [arrows in Fig. 4(c)] caused significant signal losses in the gEPSI PH image.

When the FIDs in each voxel are apodized with a half-Gaussian filter ($\sigma = 25$ ms), the SNR is improved but the image contrast is compromised in the resulting PH images [Fig. 4(a) vs (b), (c) vs (d)]. This is also illustrated with quantitative SNR and CNR results in Table 1.

Figure 5 shows the PH images synthesized from four sEPSI studies of orthotopic murine prostate cancers. The carcinoma in Fig. 5(a) shows intermediate intensity and is surrounded by a thick, low intensity rim. In Fig. 5(b), the cancer has intermediate intensity in most areas and high

**Table 1. Results of SNR and CNR in the EPSI PH images shown in Fig. 4**

| | | Non-filtered FID | | Filtered FID | |
|---|---|---|---|---|---|
| | | sEPSI PH | gEPSI PH | sEPSI PH | gEPSI PH |
| SNR[a] | TU1 | $44.0 \pm 5.3$ | $71.9 \pm 6.3$ | $45.0 \pm 2.3$ | $77.3 \pm 2.1$ |
| | TU2 | $13.3 \pm 1.4$ | $19.2 \pm 3.5$ | $21.4 \pm 2.4$ | $32.3 \pm 4.5$ |
| CNR[b] | TU1-M | $20.0 \pm 5.3$ | $45.0 \pm 6.5$ | $11.9 \pm 2.4$ | $36.0 \pm 2.5$ |
| | Tu1-Tu2 | $30.7 \pm 5.5$ | $52.8 \pm 7.2$ | $23.6 \pm 3.3$ | $45.0 \pm 4.9$ |

All values are reported as the mean $\pm$ the standard deviation.
[a] SNR is the averaged image intensity in a tumor ROI ('TU1' or 'TU2' in Fig. 3) relative to the RMS level measured in noise ROI ('N' in Fig. 4).
[b] CNR is the difference between the averaged image intensities in two ROIs relative to the noise level. $CNR_{TU1\text{-}M}$ represents CNR between the tumor ('TU1') and the muscle ('M') and $CNR_{TU1\text{-}TU2}$ represents intra-tumor CNR.

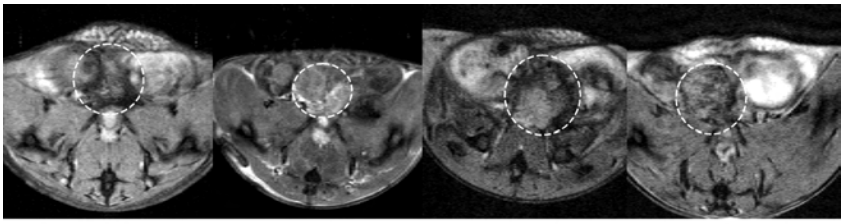


**Figure 5.** sEPSI peak height images of tumor-bearing mice. (a1–a4) Axial slices through mice prostates with LNCaP tumors (marked approximately with circles)

intensity in some isolated regions. The variation in image intensity is clearly seen in other carcinomas as well [Fig. 5(c) and (d)]. The orthotopic tumors tend to be diffuse because they follow the convoluted structure of the mouse prostate, and the PH images show their internal structures. The location of the tumors in the MR images was verified on autopsy by visual examination of the prostate.

## DISCUSSION

These results demonstrate that SNR and CNR are improved in the images of prostatic tumors in mice obtained with EPSI, compared with those obtained with conventional GRE and SE MR methods. As the figures demonstrate, the boundaries and internal textures of tumors are more clearly delineated. This improvement comes from acquisition of MR signals at various times along the FID. If a mono-exponential model of the FID is assumed in each voxel, the PH of the spectrum is an average of the FID signals sampled at various times, according to the Fourier theorems. Therefore, PH provides a statistically powerful measure of $T_2^*$. HiSS imaging has greater advantages when the water resonance is inhomogeneously broadened. In this case, the various components of the water resonance destructively interfere with one another when conventional imaging methods are used, and this degrades image quality. In HiSS MRI, individual Fourier components of the water resonance can be imaged; this avoids image distortion due to destructive interference, and provides strong $T_2^*$ contrast with improved anatomic detail. In the experiments described here, the Fourier component of the water resonance with largest amplitude was used to produce water peak height images that were improved compared to conventional images. Other Fourier components of the water resonance can also be used to produce images with novel contrast.[35]

The present results demonstrate spectrally inhomogeneous broadening of the water resonance in small voxels in the prostate and its surrounding tissues. The CSI data that served as a 'gold standard' in this study[33] show complicated water resonances with multiple components from voxels with dimensions of $\sim 200 \times 200 \times 1000\,\mu m$ (Fig. 2 spectra from 'P2', 'P3', 'P5' and 'P6'). The multiple resolved components of the water signal usually reflect differences in magnetic susceptibility among subvoxelar environments.[25–27] For example, deoxyhemoglobin in small venules within an image voxel can produce resolved components of the water signal.[28–30] In such cases, destructive interference between the various components of the water resonance causes signal loss and distortion in conventional MRI where FID data are used (i.e. either single or multiple echoes). HiSS MRI detects the details of the water resonance lineshape (for example, multiple or asymmetric resonances) that reflect the presence of multiple sub-voxel compartments, and these features are used to produce image contrast and show detailed anatomy.[17] The resonance frequency of the water peak, as well as frequencies of other resolvable components of the water signal may provide an additional useful source of contrast, as suggested by the 'peak frequency images' in Fig. 3. Thus, HiSS may provide improved sensitivity to the complicated microenvironment of prostate cancer.[32,34]

In the present experiments the water resonance line shapes from EPSI datasets are often asymmetrical, suggesting the presence of multiple components. However, EPSI does not show the well-resolved spectral features that are evident in the corresponding CSI data. This may be due to eddy currents produced by the oscillating readout gradients that can distort and broaden water lines. However, this does not reflect an inherent limitation of EPSI but rather the fact that the console and imaging gradients used for these experiments were old and not state-of-the-art. It has been demonstrated that, with newer equipment (a GE SIGNA™ 1.5 T whole-body clinical scanner equipped with high-performance self-shielded gradient coils), EPSI data can be acquired at very high spectral and spatial resolution without distortion of water spectra from small voxels.[17,18] The data acquired from human breast with modern scanners often show complicated water spectra with multiple components in small voxels.[17,18] It is likely that, with improved equipment, results of similar quality can be obtained for rodent prostate cancers.

In this study, we used two EPSI methods: gEPSI and sEPSI. The results suggest that, in general, the two methods produce PH images of similar quality. As with conventional imaging, the spin echo method is preferable

 

when there are significant macroscopic $B_0$ gradients, while the gradient echo method often provides improved contrast and SNR. In spectroscopic imaging, the spin echo method has additional advantages when phased spectra are desired, since the beginning of the FID can be measured.

In summary, two types of EPSI methods, gEPSI and sEPSI, have been tested for high spatial/spectral resolution imaging of prostate cancers in mice. The results demonstrate that both EPSI methods produce images of prostate tumors with improved SNR and $T_2$* contrast over the conventional single-echo GRE or SE imaging. The improved image quality and the efficient data acquisition using EPSI suggest that it would be useful for clinical imaging of prostate cancer in humans, as well as for imaging prostate cancer in rodents.

## Acknowledgements

This work was supported by the National Cancer Institute (1 R21 CA089408) and the Department of Defense (DAMD17-02-1-0033). G.S.K. is grateful to the American Cancer Society volunteers in the Chicago area for their support and encouragement.

## REFERENCES

1. Parkin DM, Pisani P, Ferlay J. Estimates of the worldwide incidence of 25 major cancers in 1990. *Int. J. Cancer* 1999; **80**: 827–841.
2. Rifkin MD. MRI of the prostate. *Crit. Rev. Diagn. Imag*. 1990; **31**: 223–262.
3. Schiebler ML, Tomaszewski JE, Bezzi M, Pollack HM, Kressel HY, Cohen EK, Altman HG, Gefter WB, Wein AJ, Axel L. Prostatic carcinoma and benign prostatic hyperplasia: correlation of high-resolution MR and histopathologic findings. *Radiology* 1989; **172**: 131–137.
4. Carter HB, Brem RF, Tempany CM, Yang A, Epstein JI, Walsh PC, Zerhouni EA. Nonpalpable prostate cancer: detection with MR imaging. *Radiology* 1991; **178**: 523–525.
5. Huch Boni RA, Boner JA, Lutolf UM, Trinkler F, Pestalozzi DM, Krestin GP. Contrast-enhanced endorectal coil MRI in local staging of prostate carcinoma. *J. Comput. Assist Tomogr.* 1995; **19**: 232–237.
6. Turnbull LW, Buckley DL, Turnbull LS, Liney GP, Knowles AJ. Differentiation of prostatic carcinoma and benign prostatic hyperplasia: correlation between dynamic Gd-DTPA-enhanced MR imaging and histopathology. *J. Magn. Reson. Imag*. 1999; **9**: 311–316.
7. Swanson MG, Vigneron DB, Tran TK, Sailasuta N, Hurd RE, Kurhanewicz J. Single-voxel oversampled J-resolved spectroscopy of *in vivo* human prostate tissue. *Magn. Reson. Med*. 2001; **45**: 973–980.
8. Song SK, Qu Z, Garabedian EM, Gordon JI, Milbrandt J, Ackerman JJ. Improved magnetic resonance imaging detection of prostate cancer in a transgenic mouse model. *Cancer Res*. 2002; **62**: 1555–1558.
9. Gibbs P, Tozer DJ, Liney GP, Turnbull LW. Comparison of quantitative $T_2$ mapping and diffusion-weighted imaging in the normal and pathologic prostate. *Magn. Reson. Med*. 2001; **46**: 1054–1058.
10. Yang QX, Demeure RJ, Dardzinski BJ, Arnold BW, Smith MB. Multiple echo frequency-domain image contrast: improved signal-to-noise ratio and $T_2$ ($T_2^*$) weighting. *Magn. Reson. Med*. 1999; **41**: 423–428.
11. Sarkar S, Heberlein K, Metzger GJ, Zhang X, Hu X. Applications of high-resolution echoplanar spectroscopic imaging for structural imaging. *J. Magn. Reson. Imag*. 1999; **10**: 1–7.
12. Oikawa H, Al-Hallaq HA, Lewis MZ, River JN, Kovar DA, Karczmar GS. Spectroscopic imaging of the water resonance with short repetition time to study tumor response to hyperoxia. *Magn. Reson. Med*. 1997; **38**: 27–32.
13. Al-Hallaq HA, Zamora M, Fish BL, Farrell A, Moulder JE, Karczmar GS. MRI measurements correctly predict the relative effect of tumor oxygenating agents on hypoxic fraction in rodent BA1112 tumors. *Int. J. Radiat. Oncol. Biol. Phys*. 2000; **47**: 481–488.
14. Karczmar GS, Fan X, Al-Hallaq HA, Zamora M, River JN, Rinker-Schaeffer C, Zaucha M, Tarlo K, Kellar K. Uptake of a superparamagnetic contrast agent imaged by MR with high spectral and spatial resolution. *Magn. Reson. Med*. 2000; **43**: 633–639.
15. Fan X, River JN, Zamora M, Tarlo K, Kellar K, Rinker-Schaeffer C, Karczmar GS. Differentiation of non-metastatic and metastatic rodent prostate tumors with high spectral and spatial resolution MRI. *Magn. Reson. Med*. 2001; **45**: 1046–1055.
16. Kovar DA, Al-Hallaq HA, Zamora MA, River JN, Karczmar GS. Fast spectroscopic imaging of water and fat resonances to improve the quality of MR images. *Acad. Radiol*. 1998; **5**: 269–275.
17. Du W, Du YP, Bick U, Fan X, MacEneaney PM, Zamora MA, Medved M, Karczmar GS. Breast MR Imaging with high spectral and spatial resolutions: preliminary experience. *Radiology* 2002; **224**: 577–585.
18. Medved M, Du W, Zamora M, Fan X, Olopade F, MacEneaney PM, Newstead G, Karczmar GS. The effect of varying spectral resolution on the quality of high spectral and spatial resolution magnetic resonance images of the breast. *J. Magn. Reson. Imag*. 2003; **18**: 442–448.
19. Brown TR, Kincaid B, Ugurbil K. NMR chemical shift imaging in three dimensions. *Proc. Natl. Acad. Sci. USA* 1982; **79**: 3523.
20. Zakian KL, Eberhardt S, Hricak H, Shukla-Dave A, Kleinman S, Muruganandham M, Sircar K, Kattan MW, Reuter VE, Scardino PT, Koutcher JA. Transition zone prostate cancer: metabolic characteristics at $^1$H MR spectroscopic imaging—initial results. *Radiology* 2003; **229**: 241–247.
21. Mansfield P. Spatial mapping of the chemical shift in NMR. *Magn. Reson. Med*. 1984; **1**: 370–386.
22. Posse S, Tedeschi G, Risinger R, Ogg R, Le Bihan D. High speed $^1$H spectroscopic imaging in human brain by echo planar spatial-spectral encoding. *Magn. Reson. Med*. 1995; **33**: 34–40.
23. Kuroda K, Mulkern RV, Oshio K, Panych LP, Nakai T, Moriya T, Okuda S, Hynynen K, Joles FA. Temperature mapping using the water proton chemical shift: self-referenced method with echo-planar spectroscopic imaging. *Magn. Reson. Med*. 2000; **43**: 220–225.
24. Du W, Du YP, Fan X, Zamora MA, Karczmar GS. Reduction of spectral ghost artifacts in high-resolution echo-planar spectroscopic imaging of water and fat resonances. *Magn. Reson. Med*. 2003; **49**: 1113–1120.
25. Boxerman JL, Hamberg LM, Rosen BR, Weisskoff RM. MR contrast due to intravascular magnetic susceptibility perturbations. *Magn. Reson. Med*. 1995; **34**: 555–566.
26. Kiselev VG, Posse S. Analytical theory of susceptibility induced NMR signal dephasing in a cerebrovascular network. *Phys. Rev. Lett*. 1998; **81**: 5696–5699.
27. Zhong K, Li X, Shachar-Hill Y, Picart F, Wishnia A, Springer CSJ. Magnetic susceptibility shift selected imaging (MESSI) and localized (1)H(2)O spectroscopy in living plant tissues. *NMR Biomed*. 2000; **13**: 392–397.
28. Yablonskiy DA, Haacke EM. Theory of NMR signal behavior in magnetically inhomogeneous tissues: the static dephasing regime. *Magn. Reson. Med*. 1994; **32**: 749–763.
29. Fan X, Du W, MacEneaney PM, Zamora M, Karczmar GS. Structure of the water resonance in small voxels in rat brain detected with high spectral and spatial resolution MRI. *J. Magn. Reson. Imag*. 2002; **16**: 547–552.
30. Al-Hallaq HA, Fan X, Zamora M, River JN, Moulder JE, Karczmar GS. Spectrally inhomogeneous BOLD contrast changes detected in rodent tumors with high spectral and spatial resolution MRI. *NMR Biomed*. 2002; **15**: 28–36.

 

31. Twieg DB, Meyerhoff DJ, Hubesch B, Roth K, Sappey-Marinier D, Boska MD, Gober JR, Schaefer S, Weiner MW. Phosphorus-31 magnetic resonance spectroscopy in humans by spectroscopic imaging: localized spectroscopy and metabolite imaging. *Magn. Reson. Med*. 1989; **12**: 291–305.
32. Dennie J, Mandeville JB, Boxerman JL, Packard SD, Rosen BR, Weisskoff RM. NMR imaging of changes in vascular morphology due to tumor angiogenesis. *Magn. Reson. Med*. 1998; **40**: 793–799.
33. Al-Hallaq HA, River JN, Zamora M, Oikawa H, Karczmar GS. Correlation of magnetic resonance and oxygen microelectrode measurements of carbogen-induced changes in tumor oxygenation. *Int. J. Radiat. Oncol. Biol. Phys*. 1998; **41**: 151–159.
34. Tennant TR, Kim H, Sokoloff M, Rinker-Schaeffer CW. The Dunning model. *Prostate* 2000; **43**: 295–302.
35. Medved M, Newstead GM, Fan X, Du W, Du YP, MacEneaney PM, Culp RM, Kelcz F, Olopade OI, Zamora MA, Karczmar GS. Fourier components of inhomogeneously broadened water resonances in breast: a new source of MRI contrast. *Magn. Reson. Med.* 2004; **52**: 193–196.

 

Dear Xiaobing Fan,

Here are the electronic proofs of your article.

- You can submit your corrections **online** or by **fax**. Together with your proof corrections you must return the *Copyright Transfer Statement* to complete the proof process.
- **Print out** the *proof*. (If you do not already have Acrobat Reader, just download it from http://www.adobe.com.)
- Check the metadata sheet to make sure that the header information, especially author names and the corresponding affiliations are correctly shown.
- Check that the text is complete and that all figures, tables and their legends are included. Also check the accuracy of special characters, equations, and electronic supplementary material if applicable. If necessary refer to the *Edited manuscript*.
- The publication of inaccurate data such as dosages and units can have serious consequences. Please take particular care that all such details are correct.
- Please **do not** make changes that involve only matters of style. We have generally introduced forms that follow the journal's style. Substantial changes in content, e.g., new results, corrected values, title and authorship are not allowed without the approval of the responsible editor. In such a case, please contact the Editorial Office and return his/her consent together with the proof.
- For **online** submission please insert your corrections in the online correction form [available in your eProof webpage]. Always indicate the line number to which the correction refers.
- For **fax** submission, please ensure that your corrections are clearly legible. Use a fine black pen and write the correction in the margin, not too close to the edge of the page.
- The cover sheets (including the *Copyright Transfer Statement* and the *Offprint Order Form*) can either be scanned and sent electronically or sent by fax.
- If we do not receive your corrections within 48 hours, we will send you a reminder.

**Please note**

Your article will be published **Online First** approximately one week after receipt of your corrected proofs. This is the **official first publication** citable with the DOI. **Further changes are, therefore, not possible.**

After online publication, subscribers (personal/institutional) to this journal will have access to the complete article via the DOI using the URL: http://dx.doi.org/[DOI].

If you would like to know when your article has been published online, take advantage of our free alert service. For registration and further information go to: http://www.springerlink.com.

Due to the electronic nature of the procedure, the manuscript and the original figures will only be returned to you on special request. When you return your corrections, please inform us if you would like to have these documents returned.

The **printed version** will follow in a forthcoming issue.

# Fax to: +44 870 622 1325 (UK)/ +44 870 762 8807(UK)

Springer

**From:** SHEELA. S
**6&7, 5th Street, Radhakrishnan Salai, Chennai, Tamil Nadu, India – 600 004**

**Re:** Magnetic Resonance Materials in Physics, Biology and Medicine DOI: 10.1007/s10334-005-0022-y
Multi-slice dynamic contrast-enhanced MRI using P760 distinguishes between metastatic and non-metastatic rodent prostate tumors

**Authors:** Xiaobing Fan · Milica Medved · Sean Foxley · Jonathan River · Marta Zamora · Gregory Karczmar · Claire Corot · Philippe Robert · Philippe Bourrinet

## I. Permission to publish

Dear SHEELA. S,

I have checked the proofs of my article and

- ❑ I have **no corrections.** The article is ready to be published without changes.
- ❑ I have **a few corrections.** I am enclosing the following pages:
- ❑ I have made **many corrections.** Enclosed is the **complete article.**

## II. Offprint order

- ❑ Offprint order enclosed
- ❑ I do not wish to order offprints

Remarks:

**Date / signature** _____

## III. Copyright Transfer Statement (sign only if not submitted previously)

The copyright to this article is transferred to ESMRMB
(for U.S. government employees: to the extent transferable) effective if and when the article is accepted for publication. The author warrants that his/her contribution is original and that he/she has full power to make this grant. The author signs for and accepts responsibility for releasing this material on behalf of any and all co-authors. The copyright transfer covers the exclusive right to reproduce and distribute the article, including reprints, translations, photographic reproductions, microform, electronic form (offline, online) or any other reproductions of similar nature.

An author may self-archive an author-created version of his/her article on his/her own website and his/her institution's repository, including his/her final version; however he/she may not use the publisher's PDF version which is posted on www.springerlink.com. Furthermore, the author may only post his/her version provided acknowledgement is given to the original source of publication and a link is inserted to the published article on Springer's website. The link must be accompanied by the following text: "The original publication is available at www.springerlink.com."

The author is requested to use the appropriate DOI for the article (go to the Linking Options in the article, then to OpenURL and use the link with the DOI). Articles disseminated via www.springerlink.com are indexed, abstracted and referenced by many abstracting and information services, bibliographic networks, subscription agencies, library networks, and consortia.

After submission of this agreement signed by the corresponding author, changes of authorship or in the order of the authors listed will not be accepted by Springer.

**Date / Author's signature** _____

Journal: *Magnetic Resonance Materials in Physics, Biology and Medicine*
10.1007/s10334-005-0022-y

# Offprint Order Form

- To determine if your journal provides free offprints, please check the journal's instructions to authors.
- If you do not return this order form, we assume that you do not wish to order offprints.
- If you order offprints **after** the issue has gone to press, costs are much higher. Therefore, we can supply offprints only in quantities of 300 or more after this time.
- For orders involving more than 500 copies, please ask the production editor for a quotation.

**Please enter my order for:**

| Pages | 1-4 | 1-4 | 5-8 | 5-8 | 9-12 | 9-12 | 13-16 | 13-16 | 17-20 | 17-20 | 21-24 | 21-24 | 25-28 | 25-28 | 29-32 | 29-32 |
|---|---|---|---|---|---|---|---|---|---|---|---|---|---|---|---|---|
| Copies | EUR | USD | EUR | USD | EUR | USD | EUR | USD | EUR | USD | EUR | USD | EUR | USD | EUR | USD |
| ❑ 50 | 250,00 | 275,00 | 300,00 | 330,00 | 370,00 | 405,00 | 430,00 | 475,00 | 500,00 | 550,00 | 525,00 | 575,00 | 575,00 | 630,00 | 610,00 | 670,00 |
| ❑ 100 | 300,00 | 330,00 | 365,00 | 405,00 | 465,00 | 510,00 | 525,00 | 580,00 | 625,00 | 685,00 | 655,00 | 720,00 | 715,00 | 785,00 | 765,00 | 840,00 |
| ❑ 200 | 400,00 | 440,00 | 525,00 | 575,00 | 645,00 | 710,00 | 740,00 | 815,00 | 860,00 | 945,00 | 925,00 | 1,015,00 | 1,005,00 | 1,105,00 | 1,080,00 | 1,190,00 |
| ❑ 300 | 500,00 | 550,00 | 680,00 | 750,00 | 825,00 | 910,00 | 955,00 | 1,050,00 | 1,095,00 | 1,205,00 | 1,190,00 | 1,310,00 | 1,295,00 | 1,425,00 | 1,390,00 | 1,530,00 |
| ❑ 400 | 610,00 | 670,00 | 855,00 | 940,00 | 1,025,00 | 1,130,00 | 1,195,00 | 1,315,00 | 1,360,00 | 1,495,00 | 1,485,00 | 1,635,00 | 1,615,00 | 1,775,00 | 1,740,00 | 1,915,00 |
| ❑ 500 | 720,00 | 790,00 | 1,025,00 | 1,130,00 | 1,225,00 | 1,350,00 | 1,30,00 | 1,575,00 | 1,625,00 | 1,785,00 | 1,780,00 | 1,960,00 | 1,930,00 | 2,125,00 | 2,090,00 | 2,300,00 |

**Please note that orders will be processed only if a credit card number has been provided. For German authors, payment by direct debit is also possible.**

I wish to be charged in ❑ Euro ❑ USD

Prices include surface mail postage and handling. Customers in EU countries who are not registered for VAT should add VAT at the rate applicable in their country.

VAT registration number (EU countries only):
_____

❑ **American Express**
❑ **Visa/Barclaycard/Americard**

**Number (incl. check digits):**

_ _ _ _ _ _ _ _ _ _ _ _ _ _ _ _

**Valid until:** _ _ / _ _

**Date/Signature:** _____

**For authors resident in Germany: payment by direct debit:**
**I authorize Springer-Verlag to debit the amount owed from my bank account at the due time.**

**Account no.:** _____

**Bank code:** _____

**Bank:** _____

**Date/Signature:** _____

**Send receipt to:**

❑
Xiaobing Fan
Department of Radiology
University of Chicago

Chicago, 60637, USA

❑ _____
_____
_____
_____
_____

**Ship offprints to:**

❑
Xiaobing Fan
Department of Radiology
University of Chicago

Chicago, 60637, USA

❑ _____
_____
_____
_____
_____

# Metadata of the article that will be visualized in OnlineFirst

| | | |
|---|---|---|
| ArticleTitle | **Multi-slice dynamic contrast-enhanced MRI using P760 distinguishes between metastatic and non-metastatic rodent prostate tumors** | |
| Journal Name | Magnetic Resonance Materials in Physics, Biology and Medicine | |
| Corresponding Author | Family Name | **Fan** |
| | Particle | |
| | Given Name | **Xiaobing** |
| | Suffix | |
| | Organization | University of Chicago |
| | Division | Department of Radiology |
| | Address | 60637, Chicago, IL, USA |
| | Email | xfan@uchicago.edu |
| Author | Family Name | **Medved** |
| | Particle | |
| | Given Name | **Milica** |
| | Suffix | |
| | Organization | University of Chicago |
| | Division | Department of Radiology |
| | Address | 60637, Chicago, IL, USA |
| | Email | |
| Author | Family Name | **Foxley** |
| | Particle | |
| | Given Name | **Sean** |
| | Suffix | |
| | Organization | University of Chicago |
| | Division | Department of Radiology |
| | Address | 60637, Chicago, IL, USA |
| | Email | |
| Author | Family Name | **River** |
| | Particle | |
| | Given Name | **Jonathan N.** |
| | Suffix | |
| | Organization | University of Chicago |
| | Division | Department of Radiology |
| | Address | 60637, Chicago, IL, USA |
| | Email | |
| Author | Family Name | **Zamora** |
| | Particle | |
| | Given Name | **Marta** |
| | Suffix | |
| | Organization | University of Chicago |
| | Division | Department of Radiology |
| | Address | 60637, Chicago, IL, USA |
| | Email | |

| | | |
|---|---|---|
| Author | Family Name | **Karczmar** |
| | Particle | |
| | Given Name | **Gregory S.** |
| | Suffix | |
| | Organization | University of Chicago |
| | Division | Department of Radiology |
| | Address | 60637, Chicago, IL, USA |
| | Email | |
| Author | Family Name | **Corot** |
| | Particle | |
| | Given Name | **Claire** |
| | Suffix | |
| | Organization | Guerbet Laboratories |
| | Division | |
| | Address | 95943 Roissy Charles De Gaulle, Cedex, France |
| | Email | |
| Author | Family Name | **Robert** |
| | Particle | |
| | Given Name | **Philippe** |
| | Suffix | |
| | Organization | Guerbet Laboratories |
| | Division | |
| | Address | 95943 Roissy Charles De Gaulle, Cedex, France |
| | Email | |
| Author | Family Name | **Bourrinet** |
| | Particle | |
| | Given Name | **Philippe** |
| | Suffix | |
| | Organization | Guerbet Laboratories |
| | Division | |
| | Address | 95943 Roissy Charles De Gaulle, Cedex, France |
| | Email | |



| | | |
|---|---|---|
| Schedule | Received | 15 July 2005 |
| | Revised | |
| | Accepted | 25 November 2005 |



| | |
|---|---|
| Abstract | An intermediate molecular weight contrast agent P760 was used to investigate the ability of multi-slice dynamic contrast-enhanced MRI (DCE-MRI) to distinguish metastatic from non-metastatic rodent prostate tumors. Non-metastatic AT2.1 and metastatic AT3.1 prostate tumors originally derived from the Dunning prostate cancer model were implanted on the hind leg of Copenhagen rats. Multi-sliced DCE-MRI data were acquired on a SIGNA 1.5 T scanner and analyzed using a recently developed empirical mathematical model. The P760 multi-slice DCE-MRI data in combination with the empirical mathematical model successfully distinguished between metastatic and non-metastatic rodent prostate tumors. Specifically, fitting the data with the empirical model showed that metastatic tumors had significantly faster contrast media uptake ($p<0.001$) and slower washout rates ($p<0.01$) than non-metastatic tumors. |



| | |
|---|---|
| Keywords | Dynamic contrast enhanced MRI - Prostate tumor - P760 - Rat |
| Footnote Information | |

MAGMA (2005) ■: 1–7
DOI 10.1007/s10334-005-0022-y

RESEARCH ARTICLE

**Xiaobing Fan**
**Milica Medved**
**Sean Foxley**
**Jonathan N. River**
**Marta Zamora**
**Gregory S. Karczmar**
**Claire Corot**
**Philippe Robert**
**Philippe Bourrinet**

# Multi-slice dynamic contrast-enhanced MRI using P760 distinguishes between metastatic and non-metastatic rodent prostate tumors

Received: 15 July 2005
Accepted: 25 November 2005


X. Fan (✉) · M. Medved
S. Foxley · J.N.River · M. Zamora
G.S. Karczmar
Department of Radiology,
University of Chicago, Chicago,
IL 60637, USA
E-mail: xfan@uchicago.edu
Tel.: +1-773-7024710
Fax: +1-773-7021161

C. Corot · P. Robert · P. Bourrinet
Guerbet Laboratories, 95943 Roissy
Charles De Gaulle, Cedex, France

**Abstract** An intermediate molecular weight contrast agent P760 was used to investigate the ability of multi-slice dynamic contrast-enhanced MRI (DCE-MRI) to distinguish metastatic from non-metastatic rodent prostate tumors. Non-metastatic AT2.1 and metastatic AT3.1 prostate tumors originally derived from the Dunning prostate cancer model were implanted on the hind leg of Copenhagen rats. Multi-sliced DCE-MRI data were acquired on a SIGNA 1.5 T scanner and analyzed using a recently developed empirical mathematical model. The P760 multi-slice DCE-MRI data in combination with the empirical mathematical model successfully distinguished between metastatic and non-metastatic rodent prostate tumors. Specifically, fitting the data with the empirical model showed that metastatic tumors had significantly faster contrast media uptake ($p < 0.001$) and slower washout rates ($p < 0.01$) than non-metastatic tumors.

**Keywords** Dynamic contrast enhanced MRI · Prostate tumor · P760 · Rat

## Introduction

Dynamic contrast-enhanced magnetic resonance imaging (DCE-MRI) is a promising tool for clinical detection and diagnosis of tumors. Determination of tumor grade and detection of response to therapy may be achievable based on the physiological parameters derived from analysis of DCE-MRI data [1–4].

The physiological parameters of tumor can be derived from dynamic contrast enhanced MRI depend on the properties of the contrast agent used in an experiment [5–9]. Contrast agents with different molecular weights and volumes are extracted from the vasculature and removed by the kidneys at different rates. The commonly used low molecular contrast agent, Gd-DTPA, is extracted and washed out quickly, and these rapid processes require high temporal resolution imaging [10], often not allowing for full coverage of the tumor with high spatial resolution [11]. This is potentially problematic because tumors are often highly heterogeneous, on both micro- and macroscopic scales. Conversely, macromolecular contrast agents [12–16], such as albumin-(Gd-DTPA) can be used as blood pool agents, and have been demonstrated to be sensitive to vessel permeability and particularly, hyperpermeable tumor vasculature. Unfortunately, such macromolecular contrast agents are not yet approved for clinical use; common problems with these agents are potential immunogenicity and incomplete clearance from the body. Several intermediate contrast agents have recently been studied with MRI to assess tumor microvascular characteristics and changes in these characteristics during anti-angiogenesis treatment [7, 8, 17]. P760 is a contrast agent with an intermediate molecular weight of 5.29 kDA and mean diameter of 2.8 nm [18]. Such properties restrict diffusion through the endothelium, but allow free passage through the glomerular membrane. This indicates that P760 may be more sensitive to capillary permeability than Gd-DTPA, but with slow enough dynamics to allow multi-slice coverage of the whole tumor. However, P760 has not been used in lower-



1 0 3 3 4 0 0 0 2 2 | B | Despatch: 22.12.2005 | Journal : 10334 | No. of Pages : 7
Journal No. | Manuscript No. | Author's Disk received ☑ Used ☑ Corrupted ☐ Mismatch ☐ Keyed ☐

temporal resolution multi-slice DCE-MRI of tumors as of yet.

Numerous methods have been developed to analyze the dynamic contrast enhanced signal time curves obtained from MRI [19–22]. One such method, the two-compartment model (TCM), is commonly employed to extract important physiologic parameters related to perfusion rate and capillary permeability. The model's underlying approximation is that the contrast agent is exchanged between a vascular space and a single well-mixed extravascular space [23]. However, the TCM often does not accurately fit plots of contrast concentration as a function of time; particularly during the washout period. When the TCM is used to fit such plots over longer periods of time, for instance 15 min or more, it frequently yields unreliable results [24]. This likely happens because the tumor micro-environment is typically extremely heterogeneous and not well approximated by two well-mixed compartments [22]. Instead, three (or more) compartment models may be required to accurately describe the contrast concentration in the tumor over time. However, due to the complexity of the fitting algorithm, models with increasing numbers of compartments often fail to fit data obtained with limited signal to noise ratio. Such problems may be exacerbated with an intermediate molecular weight contrast agent, such as P760, because it has a relatively slow rate of diffusion and a significant extraction fraction. Consequently, it leaves the vasculature but equilibrates slowly among multiple compartments within the tumor micro-environment. To overcome the problems associated with the TCM, various mathematical models with limited number of parameters have been developed [25]. These provide the necessary mathematical flexibility to describe contrast uptake and washout for nearly all situations, yet are much less susceptible to problems associated with low signal to noise. One such model is our recently developed empirical mathematical model (EMM), which has been shown to accurately fit data obtained with both low molecular weight agents (Gd-DTPA) and higher molecular weight agents (P792) [26].

The goal of the work presented here was to investigate the potential of lower temporal resolution multi-slice DCE-MRI data using P760 to discriminate between rodent metastatic and non-metastatic tumors. DCE-MRI data were analyzed using the EMM to obtain accurate fits to the data, and to evaluate which parameters could reliably distinguish between metastatic and non-metastatic rodent prostate tumors.

## Methods

### Tumors and contrast agent

Twenty Copenhagen rats were inoculated with one of two R3327 prostate tumor cell lines to produce masses on their right hind limbs: metastatic AT3.1 cells ($n = 8$) or non-metastatic AT2.1 cells ($n = 12$). The AT3.1 cells line is a rapidly growing sub-line of the Dunning model which quickly metastasizes to the lung [27]. The AT2.1 cell line is also rapidly growing but non-metastatic. The doubling time for AT2.1 and AT3.1 cell lines is approximately 2.5 and 1.8 days, respectively [28]. To avoid excessive metastases to the lung, rats with AT3.1 tumors were imaged within two weeks of inoculation; rats with AT2.1 tumors, within three. Tumor dimensions were measured with calipers. Since the tumors were slightly irregular in shape, they were approximated as ellipsoids with estimated volumes of $\pi LWH/6$ ($L$, $W$ and $H$ represent the tumor's length, width, and height, respectively). Average volumes were $1.1 \pm 0.5\,\mathrm{cm}^3$ and $0.9 \pm 0.5\,\mathrm{cm}^3$ for the metastatic and non-metastatic tumors, respectively. A two tailed unequal variance $t$-test showed that there was no statistically significant difference in volumes ($p > 0.40$) between the two tumor types.

A low diffusion/intermediate molecular weight contrast agent, P760 (Guerbet Research, France) [18], was used in the MRI experiments. The relaxivity ($r_1$) for P760 in 37°C water at 1.5 T is $24.7\,\mathrm{mM}^{-1}\,\mathrm{s}^{-1}$ [18]. Doses of 0.05 mmol/kg of P760 were injected at a rate of ~0.01 ml/s. The bolus injection of the contrast agent as described had no measurable effect on the animals' blood pressure, heart rate or temperature.

### MRI experiments

Rats were anesthetized prior to MR imaging. They were placed in an air-tight box and immobilized using Isofluorane delivered for 1 min, followed by an intraperitoneal (IP) injection of ketamine hydrochloride (90 mg/kg) – xylazine (10 mg/kg). A catheter (PE 50 tubing) was inserted into the external jugular vein for contrast agent delivery. PE 50 tubing was inserted into the abdomen for continuous IP administration of ketamine (90 mg/kg) and xylazine (5 mg/kg) anesthesia. This was delivered at a dose of 0.35 ml/h per 250 g. Anesthetic was provided throughout the MR imaging. The temperature of the animals was monitored rectally with a temperature probe and maintained using a warm water blanket. All experimental protocols were approved by the University of Chicago Animal Care and Use Committee.

$T_1$-weighted spoiled gradient echo images were acquired using a SIGNA 1.5 T MRI scanner (TR/TE = ~ 20/6 ms, array size = 256 × 256, FOV = 16 cm, flip angle = 60°, readout bandwidth = 32 kHz, slice thickness = 3 mm, in-plane resolution = 625 $\mu$m, NEX = 2). The MRI signal was detected using a three-inch surface coil. Five slices were imaged across the tumor with a time resolution of ~ 50 s per scan.

### Empirical mathematical model

The concentration as a function of time, $C(t)$, following contrast media injection was calculated from estimated $T_1$ values obtained by comparing the signal intensity in the selected region of interest (ROI) to the pre-contrast control signal intensity in a reference tissue (muscle) of known $T_1$ [29,30]. Although five slices were imaged across the tumor, the two outer slices were generally at the edge of the tumor. Only the three central slices

typically had sufficient signal-to-noise ratio to allow calculation of the contrast media concentration as a function of time. In such cases, the two outermost slices were not used. The concentration versus time curves were fitted using the empirical mathematical model previously developed in this laboratory [26]:

$$C(t) = A \cdot \left(1 - \mathrm{e}^{-\alpha t}\right)^{q} \cdot \mathrm{e}^{-\beta t} \cdot \frac{1 + e^{-\gamma t}}{2} \qquad (1)$$

where $A$ is the upper limit of the maximum tracer concentration (generally larger than the actual maximum concentration), $\alpha$ is the rate of contrast uptake (1/min), $\beta$ is the overall rate of contrast washout (1/min), $\gamma$ is the initial rate of contrast washout (1/min), and $q$ is related to the curvature of $C(t)$ at the transition from first pass uptake to washout.

### Data analysis

For each slice imaged, ROIs were manually defined to include the tumor rim, tumor center, whole tumor, normal muscle (approximately 10 mm away from the tumor), and muscle proximal to the tumor. The 'tumor rim' was defined as the peripheral zone of strong contrast enhancement; the remaining central region was defined as the 'tumor center'. Concentrations of P760 as a function of time were determined from the ROIs for each experiment. Data from each slice were treated as independent for purposes of statistical analysis. Concentration curves $C(t)$ were fitted with Eq. (1) using a Levenberg–Marquardt non-linear, least-squares-fit algorithm [31]. For each parameter used in the model, a two-tailed unequal variance $t$-test was performed between non-metastatic and metastatic tumors to determine if they were significantly different. A confidence interval of 95% or greater ($p < 0.05$) was considered statistically significant.

## Results

Figure 1 shows typical dynamic P760 enhanced non-metastatic (top row) and metastatic (bottom row) tumors at 10, 20, 40 and 80 min after administration of the contrast agent. The two different tumor types had similar enhancement patterns, but different temporal dynamics. Typical contrast concentration versus time curves (shown in circles) for 'whole tumor' and 'normal muscle' ROIs, data fitted with the EMM (solid line) are shown in Fig. 2 for both non-metastatic and metastatic tumors (those shown in Fig. 1). The EMM fit the data very well. Figure 3 compares EMM fits to P760 concentration curves for non-metastatic and metastatic tumors (those shown in Fig. 1) for the 'tumor rim', 'tumor center', and 'muscle near tumor' ROIs. Differences between non-metastatic and metastatic contrast concentration vs. time curves are small during the first 15 min, increasing at later times.

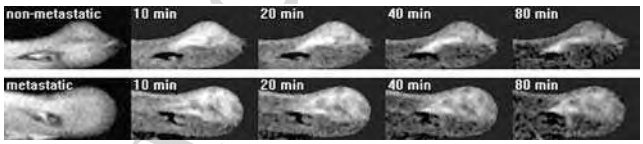


**Fig. 1** The $T_1$-weighted gradient echo images of representative non-metastatic (*top*) and metastatic (*bottom*) tumors, before and 10, 20, 40, and 80 min after contrast injection. The field-of-view is reduced from the original 16 × 16 cm to 4 × 2 cm

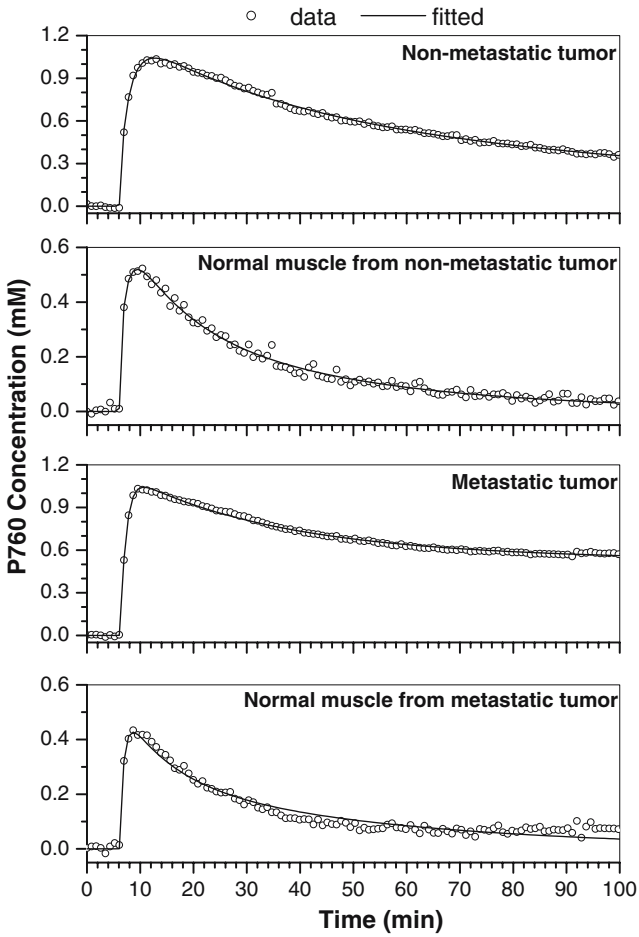


**Fig. 2** The empirical mathematical model (EMM) (*solid lines*) fits to the experimental P760 concentration versus time curve (*circles*) for representative non-metastatic and metastatic tumors (the tumors shown in Fig. 1). This is shown for both 'whole tumor' and 'normal muscle' region[illegible]erests (ROIs)

After fitting the curves with the EMM, the mean and standard deviation for each parameter was calculated for the two tumor types with the results summarized in Table 1. The average uptake rate, $\alpha$, was significantly larger ($p < 0.001$) in the metastatic tumors than in the non-metastatic tumors; however, the average washout rate, $\beta$, was lower ($p < 0.01$). This was true for both the 'tumor center' and 'whole tumor' ROIs. Figure 4 shows a plot of EMM parameters ($\alpha$ vs. $\beta$) for the 'whole tumor' ROI over all of the slices. There is good separation between the two types of tumors. This is reflected in the high statistical significance obtained using the $t$-test. The ratio between average washout

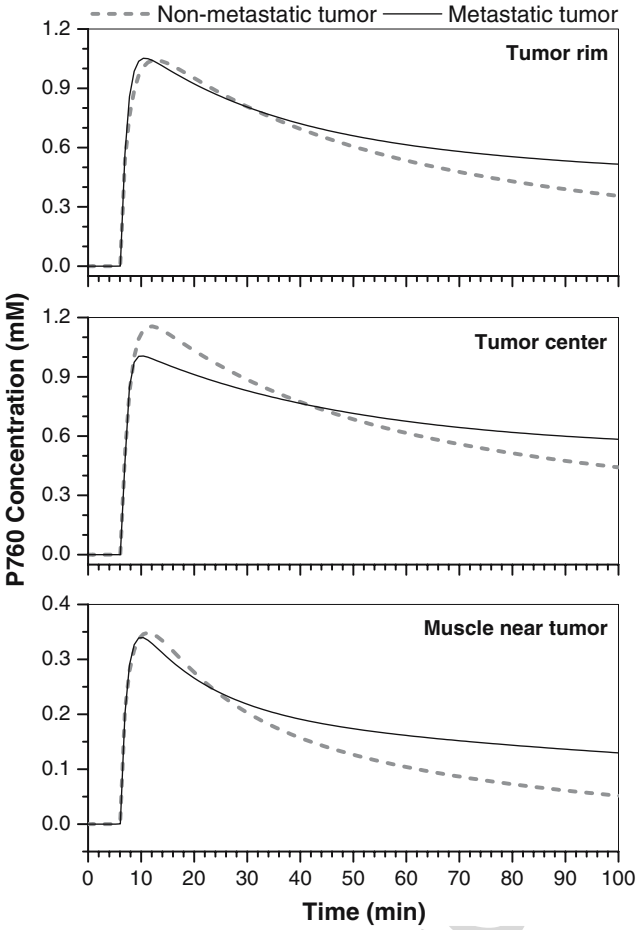


**Fig. 3** Comparison of EMM fitted P760 concentration versus time curves for non-metastatic and metastatic tumors in Fig. 1, shown for 'tumor rim', 'tumor center', and 'muscle near tumor' ROIs

rates, $\beta$, for the 'tumor rim' and the 'tumor center' ROIs was ~1.5 in metastatic tumors but only ~1.0 for non-metastatic tumors. Finally, $\beta$ was significantly different for the 'muscle near the tumor' in metastatic versus non-metastatic tumors ($p < 0.01$), indicating effects of tumor on adjacent normal tissue. For the muscle further away from the tumor there was no statistical difference in EMM parameters between non-metastatic and metastatic tumors.

## Discussion

This study showed that an intermediate molecular weight contrast agent can be used in multi-slice dynamic contrast enhanced MRI to cover the whole tumor, allowing for the discrimination between metastatic and non-metastatic rodent prostate tumors. The EMM accurately fit the contrast media concentration vs. time curves obtained using P760. This is not surprising, as it was demonstrated earlier that EMM accurately fit data obtained with both lower (Gd-DTPA) and higher (P792) molecular weight contrast agents [26]. The uptake rate $\alpha$ and the washout rate $\beta$ parameters in the EMM both differentiated between non-metastatic and metastatic rodent prostate tumors: the metastatic tumor had a significantly faster contrast uptake rate, and a significantly slower overall contrast agent washout rate than non-metastatic tumor. Statistically, the combination of these two independent parameters provided good separation between metastatic and non-metastatic tumors. The slower washout in metastatic tumors is inconsistent with previous studies of contrast media washout from breast cancers. These previous studies showed that higher grade tumors tend to have a more rapid washout [32]. This may simply be due

**Table 1** A summary of parameters obtained from the empirical mathematical model (EMM) to describe P760 uptake and washout over the tumor rim, tumor center, the whole tumor, normal muscle and muscle near tumor regions of interests (ROIs). Reported values are mean ± standard deviation for all slices. Bold numbers indicate a statistically significant difference between non-metastatic and metastatic tumors calculated by the two-tailed unequal variance $t$-test

| P760 | $A$ | $q$ | $\alpha$ (1/min) | $\beta$ (1/min) | $\gamma$ (1/min) |
|---|---|---|---|---|---|
| 12 Non-metastatic tumors (Total slices = 34) | | | | | |
| Tumor rim | 1.1 ± 0.5 | 1.7 ± 1.2 | **0.7 ± 0.3** | 0.014 ± 0.010 | 0.027 ± 0.064 |
| Tumor center | 1.1 ± 0.7 | 2.5 ± 1.7 | **0.9 ± 0.3** | **0.015 ± 0.016** | 0.020 ± 0.023 |
| Whole tumor | 1.1 ± 0.5 | 2.0 ± 1.4 | **0.8 ± 0.3** | **0.014 ± 0.010** | 0.025 ± 0.049 |
| Normal muscle | 0.6 ± 0.2 | 2.3 ± 1.8 | 1.2 ± 0.6 | 0.030 ± 0.015 | 0.080 ± 0.087 |
| Muscle near tumor | 0.6 ± 0.2 | 2.3 ± 1.9 | 1.0 ± 0.5 | **0.029 ± 0.015** | 0.039 ± 0.033 |
| 8 Metastatic tumors (Total slices = 26) | | | | | |
| Tumor rim | 1.2 ± 0.4 | 2.0 ± 1.6 | **0.9 ± 0.3** | 0.011 ± 0.006 | 0.014 ± 0.016 |
| Tumor center | 1.0 ± 0.4 | 3.0 ± 1.5 | **1.3 ± 0.4** | **0.007 ± 0.006** | 0.023 ± 0.021 |
| Whole tumor | 1.1 ± 0.4 | 2.5 ± 1.6 | **1.1 ± 0.3** | **0.008 ± 0.005** | 0.021 ± 0.017 |
| Normal muscle | 0.6 ± 0.2 | 2.0 ± 1.9 | 1.1 ± 0.7 | 0.028 ± 0.008 | 0.070 ± 0.038 |
| Muscle near tumor | 0.6 ± 0.2 | 1.8 ± 1.8 | 0.9 ± 0.5 | **0.020 ± 0.008** | 0.049 ± 0.032 |

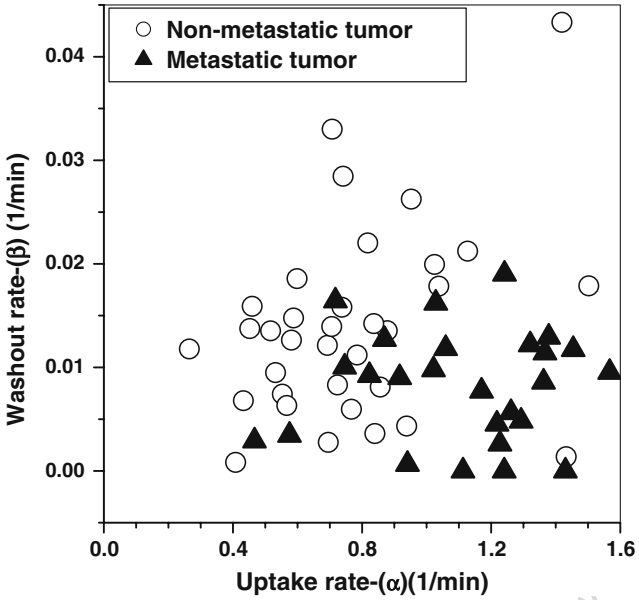


**Fig. 4** Uptake rate ($\alpha$) plotted vs. washout rate ($\beta$) for all slices in all metastatic (*triangles*) and non-metastatic (*circles*) tumors. Data are taken from the 'whole tumor' ROI

to differences between animal models and humans [33]. However, it may also reflect the fact that in these experiments contrast media washout was followed for much longer than is feasible in patient studies, and that the EMM provided very accurate fits to this extended washout.

The EMM parameters in the muscle near the tumor edge also showed significant differences between metastatic and non-metastatic tumors, demonstrating strong physiological effects of the tumor on the nearby tissue. This suggests that MRI can detect the influence of aggressive tumors on its surrounding tissue. The change in muscle uptake/washout may be due to invading tumor cells, neovasculature, or inflammation caused by tumor growth and invasion, all of which may be markers for tumor grade. Examination of the 'normal' tissue near a suspicious lesion could improve early detection of cancers and facilitate accurate diagnosis.

In the current study, multi-slice imaging was performed in order to cover the whole tumor, at the expense of temporal resolution. In our earlier study, a single slice was imaged with a much higher temporal resolution (5 s) [26]. While in the current study differences between $\alpha$ and $\beta$ in metastatic and non-metastatic tumors were found to be statistically significant, in the earlier study $A$ and $\beta$ were found to be the differentiating parameters (for both Gd-DTPA and P792). Since the molecular weight of P760 falls between the values for these two contrast agents, this change is likely due to the lower temporal resolution in this study which was necessary to accommodate the increase in the amount of data collected [10]. For data acquired at low temporal resolution, $A$ is very sensitive to the equilibrium distribution volume of the contrast agent. At high temporal resolution, $A$ primarily reflects first pass uptake of the contrast agent, which is proportional to perfusion [23, 34]. This difference has implications for clinical studies where lower temporal resolution is often chosen so that a large volume of tissue can be imaged [11].

P760 has a low rate of interstitial diffusion, with its molecular weight approximately 10 times higher and the molecular volume 30 times higher than those of Gd-DTPA. However, P760 contrast uptake and washout curves were more similar to those of Gd-DTPA than to those of P792. This is likely because the magnitude of the initial washout rate, $\gamma$, for P760 is closer to that of Gd-DTPA than to that of P792 [26]. For all three contrast agents, the metastatic rodent tumors had significantly slower washout rates than the non-metastatic tumors. The previous study also showed that for both Gd-DTPA and P792, metastatic tumors had, on average, a higher uptake rate, $\alpha$, than non-metastatic tumors. However, this was not a statistically significant result, probably due to the small sample population. Thus the current results are consistent with those of the previous study.

A number of improvements in the EMM approach are planned. Most importantly, future studies will derive the relationship between physiological parameters such as blood flow, capillary permeability and contrast media distribution volume, and the parameters used in the EMM. A deconvolution of the arterial input function determined from a reference tissue [35] from the contrast concentration curves will be performed prior to fitting, so that the unit impulse response curves can be compared between different experiments. Averaging over the ROIs performed in this study may have reduced the sensitivity of some parameters in the EMM to differences between metastatic and the non-metastatic tumors. This can be seen from visual inspection of contrast media uptake patterns in Fig. 1. Small areas within the ROIs showed large changes in signal intensity due to the rapid rate of contrast uptake while other areas showed comparatively little change. Due to the robust nature of EMM fitting, the signal-to-noise ratio should be sufficient to permit pixel-by-pixel analysis, and this approach will be utilized in future studies to refine the model and improve discrimination between metastatic and non-metastatic tumors.

In summary, we found that multi-slice DCE-MRI using P760 was able to successfully discriminate between non-metastatic and metastatic tumors. The lower temporal resolution necessary for whole tumor coverage reduced the statistical significance of one of the EMM parameters – the contrast media uptake rate – but overall, EMM provided excellent fits to experimental data and was effective in differentiating metastatic from non-metastatic primary tumors. This suggests that a similar

approach could be used in MRI examinations of patients, as has been done in using other mathematical models [25]. Further improvements could be achieved by using pixel-by-pixel analysis and correcting for the arterial input function variations.

**Acknowledgements** This work was supported in part by a grant from the Guerbet Laboratories, Roissy CDG Cedex, France, the Cancer Research Foundation, and the NCI (R21 CA089408–01A1).

## References


1. den Boer JA, Hoenderop RK, Smink J, Dornseiffen G, Koch PW, Mulder JH, Slump CH, Volker ED, de Vos RA (1997) Pharmacokinetic analysis of Gd-DTPA enhancement in dynamic three-dimensional MRI of breast lesions. J Magn Reson Imaging 7:702–715
2. Kuhl CK, Mielcareck P, Klaschik S, Leutner C, Wardelmann E, Gieseke J, Schild HH (1999) Dynamic breast MR imaging: are signal intensity time course data useful for differential diagnosis of enhancing lesions? Radiology 211:101–110
3. Padhani AR, Gapinski CJ, Macvicar DA, Parker GJ, Suckling J, Revell PB, Leach MO, Dearnaley DP, Husband JE (2000) Dynamic contrast enhanced MRI of prostate cancer: correlation with morphology and tumour stage, histological grade and PSA. Clin Radiol 55:99–109
4. Martincich L, Montemurro F, De Rosa G, Marra V, Ponzone R, Cirillo S, Gatti M, Biglia N, Sarotto I, Sismondi P, Regge D, Aglietta M (2004) Monitoring response to primary chemotherapy in breast cancer using dynamic contrast-enhanced magnetic resonance imaging. Breast Cancer Res Treat 83:67–76
5. Brix G, Kiessling F, Lucht R, Darai S, Wasser K, Delorme S, Griebel J (2004) Microcirculation and microvasculature in breast tumors: pharmacokinetic analysis of dynamic MR image series. Magn Reson Med 52:420–429
6. Turetschek K, Preda A, Novikov V, Brasch RC, Weinmann HJ, Wunderbaldinger P, Roberts TP (2004) Tumor microvascular changes in antiangiogenic treatment: assessment by magnetic resonance contrast media of different molecular weights. J Magn Reson Imaging 20:138–144
7. Preda A, Novikov V, Moglich M, Turetschek K, Shames DM, Brasch RC, Cavagna FM, Roberts TP (2004) MRI monitoring of Avastin antiangiogenesis therapy using B22956/1, a new blood pool contrast agent, in an experimental model of human cancer. J Magn Reson Imaging 20:865–873
8. Preda A, Novikov V, Moglich M, Floyd E, Turetschek K, Shames DM, Roberts TP, Corot C, Carter WO, Brasch RC (2005) Magnetic resonance characterization of tumor microvessels in experimental breast tumors using a slow clearance blood pool contrast agent (carboxymethyldextran-A2-Gd-DOTA) with histopathological correlation. Eur Radiol
9. Pathak AP, Artemov D, Ward BD, Jackson DG, Neeman M, Bhujwalla ZM (2005) Characterizing extravascular fluid transport of macromolecules in the tumor interstitium by magnetic resonance imaging. Cancer Res 65:1425–1432
10. Henderson E, Rutt BK, Lee TY (1998) Temporal sampling requirements for the tracer kinetics modeling of breast disease. Magn Reson Imaging 16:1057–1073
11. Kuhl CK, Schild HH, Morakkabati N (2005) Dynamic bilateral contrast-enhanced MR imaging of the breast: trade-off between spatial and temporal resolution. Radiology 236:789–800
12. Shames DM, Kuwatsuru R, Vexler V, Muhler A, Brasch RC (1993) Measurement of capillary permeability to macromolecules by dynamic magnetic resonance imaging: a quantitative noninvasive technique. Magn Reson Med 29:616–622
13. Weissleder R, Cheng HC, Marecos E, Kwong K, Bogdanov AJ (1998) Non-invasive in vivo mapping of tumour vascular and interstitial volume fractions. Eur J Cancer 34:1448–1454
14. Brasch RC, Daldrup H, Shames D, Wendland M, Okuhata Y, Rosenau W (1998) Macromolecular contrast media-enhanced MRI estimates of microvascular permeability correlate with histopathologic tumor grade. Acad Radiol 5 Suppl 1:S2–5
15. Turetschek K, Floyd E, Shames DM, Roberts TP, Preda A, Novikov V, Corot C, Carter WO, Brasch RC (2001) Assessment of a rapid clearance blood pool MR contrast medium (P792) for assays of microvascular characteristics in experimental breast tumors with correlations to histopathology. Magn Reson Med 45:880–886
16. Dafni H, Israely T, Bhujwalla ZM, Benjamin LE, Neeman M (2002) Overexpression of vascular endothelial growth factor 165 drives peritumor interstitial convection and induces lymphatic drain: magnetic resonance imaging, confocal microscopy, and histological tracking of triple-labeled albumin. Cancer Res 62:6731–6739
17. Turetschek K, Floyd E, Helbich T, Roberts TP, Shames DM, Wendland MF, Carter WO, Brasch RC (2001) MRI assessment of microvascular characteristics in experimental breast tumors using a new blood pool contrast agent (MS-325) with correlations to histopathology. J Magn Reson Imaging 14:237–242
18. Corot C, Port M, Raynal I, Dencausse A, Schaefer M, Rousseaux O, Simonot C, Devoldere L, Lin J, Foulon M, Bourrinet P, Bonnemain B, Meyer D (2000) Physical, chemical, and biological evaluations of P760: a new gadolinium complex characterized by a low rate of interstitial diffusion. J Magn Reson Imaging 11:182–191
19. Larsson HB, Stubgaard M, Frederiksen JL, Jensen M, Henriksen O, Paulson OB (1990) Quantitation of blood-brain barrier defect by magnetic resonance imaging and gadolinium-DTPA in patients with multiple sclerosis and brain tumors. Magn Reson Med 16:117–131
20. Brix G, Semmler W, Port R, Schad LR, Layer G, Lorenz WJ (1991) Pharmacokinetic parameters in CNS Gd-DTPA enhanced MR imaging. J Comput Assist Tomogr 15:621–628
21. Tofts PS (1997) Modeling tracer kinetics in dynamic Gd-DTPA MR imaging. J Magn Reson Imaging 7:91–101
22. Port RE, Knopp MV, Hoffmann U, S. M-Z, Brix G (1999) Multicompartment analysis of gadolinium chelate kinetics: blood-tissue exchange in mammary tumors as monitored by dynamic MR imaging. J Magn Reson Imaging 10:233–241

23. Tofts PS, Brix G, Buckley DL, Evelhoch JL, Henderson E, Knopp MV, Larsson HB, Lee TY, Mayr NA, Parker GJ, Port RE, Taylor J, Weisskoff RM (1999) Estimating kinetic parameters from dynamic contrast-enhanced T(1)-weighted MRI of a diffusable tracer: standardized quantities and symbols. J Magn Reson Imaging 10:223–232
24. Su MY, Jao JC, Nalcioglu O (1994) Measurement of vascular volume fraction and blood-tissue permeability constants with a pharmacokinetic model: studies in rat muscle tumors with dynamic Gd-DTPA enhanced MRI. Magn Reson Med 32:714–724
25. Moate PJ, Dougherty L, Schnall MD, Landis RJ, Boston RC (2004) A modified logistic model to describe gadolinium kinetics in breast tumors. Magn Reson Imaging 22:467–473
26. Fan X, Medved M, River JN, Zamora M, Corot C, Robert P, Bourrinet P, Lipton M, Culp RM, Karczmar GS (2004) New model for analysis of dynamic contrast-enhanced MRI data distinguishes metastatic from nonmetastatic transplanted rodent prostate tumors. Magn Reson Med 51:487–494
27. Tennant TR, Kim H, Sokoloff M, Rinker-Schaeffer CW (2000) The Dunning model. Prostate 43:295–302
28. Isaacs JT, Isaacs WB, Feitz WF, Scheres J (1986) Establishment and characterization of seven Dunning rat prostatic cancer cell lines and their use in developing methods for predicting metastatic abilities of prostatic cancers. Prostate 9:261–281
29. Medved M, Karczmar G, Yang C, Dignam J, Gajewski TF, Kindler H, Vokes E, MacEneany P, Mitchell MT, Stadler WM (2004) Semiquantitative analysis of dynamic contrast enhanced MRI in cancer patients: Variability and changes in tumor tissue over time. J Magn Reson Imaging 20:122–128
30. Workie DW, Dardzinski BJ, Graham TB, Laor T, Bommer WA, O'Brien KJ (2004) Quantification of dynamic contrast-enhanced MR imaging of the knee in children with juvenile rheumatoid arthritis based on pharmacokinetic modeling. Magn Reson Imaging 22:1201–1210
31. Press WH, Teukolsky SA, Vetterling WT, Flannery BP (1997) Numerical recipes in C: The art of scientific computing. Cambridge University Press, Oxford
32. Knopp MV, Weiss E, Sinn HP, Mattern J, Junkermann H, Radeleff J, Magener A, Brix G, Delorme S, Zuna I, van Kaick G (1999) Pathophysiologic basis of contrast enhancement in breast tumors. J Magn Reson Imaging 10:260–266
33. Bhujwalla ZM, Artemov D, Natarajan K, Ackerstaff E, Solaiyappan M (2001) Vascular differences detected by MRI for metastatic versus nonmetastatic breast and prostate cancer xenografts. Neoplasia 3:143–153
34. Evelhoch JL (1999) Key factors in the acquisition of contrast kinetic data for oncology. J Magn Reson Imaging 10:254–259
35. Kovar DA, Lewis M, Karczmar GS (1998) A new method for imaging perfusion and contrast extraction fraction: input functions derived from reference tissues. J Magn Reson Imaging 8:1126–1134

# Differentiation of Non-Metastatic and Metastatic Rodent Prostate Tumors with High Spectral and Spatial Resolution MRI

Xiaobing Fan[1], Jonathan N. River[1], Marta Zamora[1], Kirk Tarlo[3], Kenneth Kellar[3], Carrie Rinker-Schaeffer[2], and Gregory S. Karczmar[1+]

Departments of [1]Radiology and [2] Urology
University of Chicago
Chicago, IL 60637

and

[3] Nycomed Amersham
Princeton, NJ 08540

**SUBMITTED TO: Magnetic Resonance Medicine (MRM-100-4799)**

[+]**Address Correspondence To:**

Gregory Karczmar, Ph.D.
Associate Professor
Department of Radiology, MC2026
University of Chicago
5841 S. Maryland Ave.
Chicago, IL, USA 60637

Phone: 773-702-0214
Fax: 773-702-1161
Email: gskarczm@midway.uchicago.edu

# ABSTRACT

MR images can be acquired with high spectral and spatial resolution to precisely measure lineshapes of the water and fat resonances in each image voxel. Previous work suggests that the high resolution spectral information can be used to improve image contrast, signal-to-noise ratio, sensitivity to contrast agents and to physiologic and biochemical processes that affect local magnetic susceptibility gradients. The potential advantages of high resolution spectroscopic imaging (SI) suggest that it might be useful for early detection and characterization of tumors. The present experiments evaluate use of high resolution SI to discriminate between metastatic and non-metastatic rodent Dunning prostate tumors. SI datasets were obtained at 4.7 Tesla with in-plane resolution of 350-500 microns in a single 1.0 mm slice, and 6-8 Hz spectral resolution, before and after I.V. injection of an iron oxide contrast agent. Images of water signal peak height in non-metastatic tumors were smoother in the tumor interior than images of metastatic tumors ($p < .004$ by T-test) before contrast media injection. This difference was stronger in contrast enhanced images ($p < .0004$). In addition, the boundary between the tumor and muscle was more clearly demarcated in non-metastatic than metastatic tumors. Combinations of image texture, tumor edge morphology, and changes in $T_2^*$ following contrast media injection improved discrimination between metastatic and non-metastatic tumors. The data presented here do not demonstrate that effective discrimination between metastatic and non-metastatic tumors depends on the use of high resolution SI. However, the results suggest that SI and/or other MR methods that provide similar contrast might be used clinically for early and accurate detection of metastatic disease.

# INTRODUCTION

Sensitive and accurate non-invasive imaging methods are needed to detect breast and prostate cancer at an early stage and accurately identify metastatic disease. Screening measures such as blood tests for prostate-specific antigen have been useful for targeting groups with histological prostate disease. However only twenty percent of American men above the age of 50 with histological evidence of disease have clinically important disease, i.e., disease that may metastasize and result in death [1,2]. Similar considerations apply to breast cancer; breast lesions must be detected early and since the majority of suspicious lesions found by screening procedures are not dangerous, it is important to distinguish between those with high metastatic potential and those with little or no malignant potential [3]. MRI is a strong candidate for detection and evaluation of breast and prostate abnormalities because it has strong soft tissue contrast and is non-invasive. In addition, intravascular MR contrast agents can be used to detect high blood flow, vascular density, and capillary permeability that often characterizes metastatic lesions (e.g. [4-7]). However, despite a great deal of effort MRI studies of prostate cancer and breast cancer patients have not conclusively demonstrated the high sensitivity and specificity that would justify routine clinical use of this approach.

Improved approaches to data acquisition and analysis are needed to increase the sensitivity and specificity of MRI. Here we evaluate the potential of high spectral and spatial resolution MR imaging to improve detection and classification of suspicious lesions. High resolution spectroscopic imaging (referred to in the following as high resolution SI, or SI) is a natural extension of the pioneering work of Dixon et al. [8] and Glover et al. [9], demonstrating that spectral information at low resolution can greatly improve image quality by separating water and fat signals and correcting images for $B_o$ field inhomogeneities. More recently, images have

been acquired with increased spectral resolution to resolve the details of the water (and fat) lineshape in each image voxel [10-13]. For example we have obtained images with high spatial resolution and spectral resolution as high as 3 Hz at 4.7 Tesla [11,12,14-16]. The rationale for high resolution SI is that the water signal from living tissue is generally homogeneously broadened and often contains multiple resolvable components [14,16,17] due to local, sometimes microscopic magnetic susceptibility gradients. These gradients reflect local anatomy and physiology, as well as the effects of synthetic contrast agents [16,17]. The shape of the water resonance can be an important source of image contrast – for example, images can be synthesized with intensity proportional to the amplitude, resonance frequency, integral, and linewidth of the entire envelope of the water signal or of its individual components. Other features can also be used to produce images, e.g. the number of components in the water signal or the asymmetry of the water envelope. High resolution SI produces images with stronger $T_2^*$ contrast than is available in conventional gradient echo images because the proton signal can be followed for many hundreds of milliseconds, without the destructive interference between the various Fourier components of the water resonance that degrades gradient echo images at long TE. Work from several laboratories has suggested potential advantages of high resolution SI, including improved signal-to-noise ratio, image contrast, edge delineation, and increased sensitivity to contrast agents [10-14,18]. High resolution SI has also been used to improve detection of changes in local tumor blood oxygenation caused by tumor oxygenating therapies [11,14]. SI is particularly useful in tumors, where the proton signals *in vivo* are often complex due to deoxygenated blood, hemorrhage, sequestration of iron, and a generally inhomogeneous microenvironment [14,16,17].

The potential advantages of high resolution SI suggest that it may facilitate sensitive and accurate detection of cancer by MR. The purpose of the present work is to evaluate whether or not contrast-enhanced high resolution SI reliably discriminates between metastatic and non-metastatic cancer in a well defined, stable rodent tumor model. In the experiments reported here we used high resolution SI to image Dunning AT2.1 (non-metastatic) and AT3.1 (metastatic) prostate tumors implanted in the hind limbs of Copenhagen rats. We compared image texture, tumor boundaries, and effects of a superparamagnetic iron oxide contrast agent in the two cell lines.

# METHODS

## Tumors

Experimental protocols involving animals were approved by the University of Chicago Animal Care and Use Committee (Protocol # 70784R) and were consistent with federal, state, and local regulations. Metastatic (Dunning AT3.1) and non-metastatic (Dunning AT2.1) tumors were grown in the hind limbs of Copenhagen rats. R3327 prostatic cancer cell lines AT2.1 (n=8) (low metastatic potential) and AT3.1 (n=7) (high metastatic potential) [19,20] were grown in standard RPMI-1640 medium (Cellgro, Mediatech/CellGro, Herndon, VA) containing 8% fetal calf serum (Gibco-BRL, Inc.), penicillin (10,000u), streptomycin (100 ug/ml; Gibco-BRL, Inc.), and 250 nM dexamethasone (Sigma Chemical Co., St. Louis, MO). The tumor cells were subcutaneously injected ($2\times10^5$ cells per injection) into rat hind limbs using a 26 G needle. Rats were anesthetized with isofluorane during the injection.

## Contrast agent

NC100150 (Clariscan$^{TM}$, Nycomed-Amersham, Princeton, New Jersey and Amersham, UK) was injected I.V. at a dose of 2 mgs/kg. NC100150 is a superparamagnetic particulate, currently in phase III clinical trials, with average diameter (including iron core and oxidized starch coating) of 15 – 20 nanometers, $R_1$ of 8 $m\underline{M}^{-1} * sec^{-1}$, and $R_2$ of ~40 $m\underline{M}^{-1} * sec^{-1}$ at 4.7 Tesla [21]. The contrast agent had no measurable effects on animals' blood pressure, heart rate or temperature.

## Anesthesia, immobilization, and monitoring of rats during MR experiments

On the day of the MR experiment, anesthesia was initially induced with isofluorane, and a ketamine hydrochloride (90 mg/kg) - xylazine (10 mg/kg) mixture was then injected I.P. A catheter (PE 50 tubing) was inserted into the external jugular vein for injection of the contrast agent. During MR measurements, animals were anesthetized by continuous I.P. administration of ketamine (90 mg/kg per hr) and rompun (5 mg/kg per hr). The temperature of the animals was controlled using a warm water blanket, and in addition the magnet was continuously flushed with warm air using an animal cage dryer. To minimize motion artifacts, rats were secured to a Plexiglas board using vet wrap and tape. The tumor bearing leg was immobilized horizontally, placed in the Helmholtz detector coil and secured with tape. The long axis of the leg was placed perpendicular to the main magnetic field. A capillary tube filled with water was placed inside the coil above the tumor and was used as a marker for the midline of the tumor in MR images. Blood pressure was continuously measured during MR studies using a catheter (PE-50) implanted in the femoral artery attached to a pressure transducer and a Tektronix monitor. Animal temperature was continuously measured using a rectal thermometer (Fisher Scientific, Springfield, N.J.). Approximately 60 minutes were required to prepare and position the animal in the magnet.

## MR measurements

MR experiments were performed using a 4.7 Tesla GE/Bruker Omega scanner (Fremont, CA) equipped with self-shielded gradient coils. A Helmholtz coil was used for signal excitation and detection. The high resolution spectroscopic images were obtained using the approach developed by Brown *et al.* [22] and Maudsley *et al.* [23]; following slice selection, phase encoding gradient pulses were applied along two axes before detection of the proton free induction decay to provide spatial resolution. A single 1.0 mm thick slice through the center of the tumor was imaged with in-plane resolution of 350-500 microns (64×64 points) and frequency resolution of 6.0 - 8.0 Hz. The total acquisition time for each spectroscopic image was 11 - 14 minutes. Sequential images were collected before and after injection of contrast agent.

## Calculations of peak height and $T_2^*$-weighted images from absorption spectra

Water and fat spectra were corrected for truncation artifacts and the pure absorption spectra in each pixel were calculated using the method described by Fan *et al.* [24]. Images were calculated with intensity proportional to water signal peak height and $T_2^*$. With complex spectra such as those found in tumors [14,16,17] $T_2^*$ (or linewidth) is not well defined, but approximately $T_2^*$-weighted images were calculated from absorption spectra by measuring the inverse line width of the water signal at the half peak height. An additional empirical estimate of the linewidth was obtained by dividing the integral by the peak height of each resonance. Other parameters derived from water signal lineshape might enhance discrimination between metastatic and non-metastatic tumors. However, water signal peak height and linewidth can be determined with high signal-to-noise ratio and are sensitive to all of the Fourier components that contribute to the water resonance.

## Quantitative measures of image texture and edge delineation

To determine image texture, image intensity (*z*) was defined as a function (*f*) of the *x* and *y* locations of each pixel:

$$z = f(x, y). \tag{1}$$

The surface area of the function (*z*) was found numerically from the following equation,

$$S = \sum \sqrt{1 + f_x^2 + f_y^2}, \tag{2}$$

where the summation is over the region of interest (e.g. the tumor), $f_x = \partial f / \partial x$, and $f_y = \partial f / \partial y$. The function $\sqrt{1 + f_x^2 + f_y^2}$ exhibits maxima at the pixels where the derivatives of peak intensity with respect to spatial coordinates x and y are larger, for example, at the edge of the tumor. Therefore, this function could be used to display images that emphasize the variations of peak intensity. As a measure of the texture of the image, we defined the parameter '$S_r$',

$$S_r = 100.0 \cdot \left| S(\text{tumor}) - S_{xy} \right| / S_{xy}, \tag{3}$$

where $S$(tumor) is the surface area of the function, 'z' (arbitrary units), in the region of interest calculated from Equation 2, and $S_{xy}$ is the projection of $S$(tumor) onto the x-y plane. $S_r$ measures the variation in image intensity over the projected area. If image intensity in the region of interest is constant, $S_r$ is 0, whereas highly variable image intensity results in a large $S_r$. To minimize noise the peak height images (which have high signal-to-noise ratio and contrast) were used in the analysis. Since gain and other instrumental parameters were different for each experiment, the $S_r$ value directly calculated from the peak height image could not be compared between experiments. Therefore the intensity of peak height images was normalized by dividing by the average intensity in the muscle region for each experiment prior to

calculating $S_r$. Edge enhanced images were calculated from the peak height images by using the formula in Equation 2 without summation.

The ratio ($I_r$) of average image intensity in the tumor to average intensity in the muscle was defined as

$$I_r = I_{\text{average}}(\text{tumor}) \big/ I_{\text{average}}(\text{muscle}), \tag{4}$$

where $I_{\text{average}}(\text{tumor})$ is the average intensity of a region in the tumor, and $I_{\text{average}}(\text{muscle})$ is the average intensity in the selected muscle region. Since muscle was assumed to be the same in both non-metastatic and metastatic tumors, $I_r$ is a normalized measure of average intensity in the tumors.

As a measure of the irregularity of the tumor border, we calculated the ratio ($A_r$) of the tumor area to that of a circle that has the same circumference as the tumor,

$$A_r = A_c / A_{ROI}\ , \tag{5}$$

where $A_{ROI}$ is the tumor area with the boundary traced manually with IDL software (Research Systems, Inc., Boulder, CO), and $A_C$ is the area of the corresponding circle. Thus, $A_r$ is large if the tumor boundary is irregular, and close to 1 if the tumor boundary is smooth.

## Contrast agent kinetics

The average $T_2^*$ of the water resonance in the tumor reached a minimum immediately after NC100150 contrast agent injection. We calculated the maximum decrease in $T_2^*$ or increase in $1/T_2^*$ ($R_2^*$) averaged over the entire tumor – using only those pixels in which $T_2^*$ decreased. Changes in $R_2^*$ ($\Delta R_2^*$) are approximately proportional to the concentration of contrast agent in each voxel. Since the contrast agent is intravascular at early times after injection $\Delta R_2^*$ is sensitive to tumor blood volume. This is only a qualitative measure of tumor blood volume

because of leakage of the contrast media into the extravascular space and the fact that the low time resolution of the data did not permit extrapolation of $\Delta R_2^*$ to time '0'. Rapid diffusion-mediated exchange of magnetization between the intravascular and extravascular spaces [25] may also have reduced the accuracy of blood volume measurements.

Contrast media washout rate was measured based on the rate at which $R_2^*$ returned to the control value following the maximum increase (i.e. decrease in $T_2^*$). The concentration of NC100150 as a function of time, $C(t)$, generally reached a maximum in the first image obtained after injection (t ~ 10 minutes after injection) and then decayed monotonically toward '0'. $C(t)$ was modeled as an exponential decay curve starting where $C(t) = C_{max}$.

## Synthesis of gradient echo images

The purpose of the present work was to evaluate the use of high resolution SI to discriminate between metastatic and non-metastatic tumors. Statistically meaningful comparison of high resolution SI with conventional imaging is not supported by the present results. However, to obtain a crude qualitative comparison of SI with gradient echo imaging, gradient echo images were synthesized from SI datasets. To do this, points on each phase encoded proton free induction decay acquired between ~20 msec and ~25 msec after excitation were summed and a 2DFT with respect to the phase encoding gradient amplitude was used to obtain images. This simulates gradient echo images acquired with TE/TR of approximately 20 msec/140 msec and a bandwidth of ~12 kHz. The images were then analyzed to determine measures of texture as described above.

# RESULTS

Fig. 1 and Fig. 2 show all control peak height images (A), edge enhanced images (B), and difference images (C) (immediately after contrast injection minus before injection) for non-metastatic and metastatic tumors, respectively. The images are displayed in the order the experiments were performed from the most recent '1' to earliest '12'. The orientations of the imaging slices are sagital, i.e. perpendicular to the long axis of the legs, except that image 12 in Fig. 1, and images 6, 8, and 12 in Fig. 2 are axial. (Note that the long axis of the leg is perpendicular to main field.) A summary of estimated tumor growth rates and tumor cross-sectional areas (determined from images) is given in Table 1. The numbers in column '1' correspond to the image numbers in Figs. 1 and 2. The average tumor growth rate and cross-sectional area are less in non-metastatic tumors (0.07±0.02 $cm^3$/day and 0.85±0.14 $cm^{2,}$ respectively) compared to metastatic tumors (0.11±0.02 $cm^3$/day and 1.20±0.16 $cm^2$, respectively (mean ± standard error)). However, these differences are not significantly different. Size and growth rate did not correlate with any of the MR parameters measured.

Regions of interest for the interior of each tumor and for the entire tumor (i.e. excluding and including the edge of the tumor, respectively) were traced manually from the edge enhanced images. Equation 3 was then used to calculate $S_r$(tumor interior) and $S_r$(entire tumor) from images obtained immediately before contrast media injection and at the time after contrast media injection when $\Delta R_2^*$ was largest. These parameters are listed for each tumor studied in Table 1. Various combinations of parameters were used to generate 2-dimensional plots to improve separation of metastatic and non-metastatic tumors. Fig. 3 shows $S_r$(tumor interior, before contrast agent injection; $S_r$ is given in arbitrary units) for all 24 tumors plotted against the values of $S_r$ obtained after contrast injection. Before contrast agent injection $S_r$(interior) was significantly larger in the metastatic tumors than the non-metastatic tumors (see Table 2), i.e., the

surface variations are much greater in metastatic tumors ($p < 0.004$ by two-tailed T-test). After contrast agent injection the separation between the distributions of metastatic and non-metastatic tumors improved to $p < 0.0004$. Although the differences between metastatic and non-metastatic tumors were highly statistical significant, classification of individual metastatic and non-metastatic tumors based on $S_r$ was not completely reliable. Fig. 3 demonstrates significant overlap between the two distributions.

The edge enhanced images suggest that the non-metastatic tumors generally have a more clearly demarcated boundary between the tumor and muscle/skin than the metastatic tumors. At the present spatial resolution, edges were difficult to define precisely, but an approximate measure of the sharpness of tumor edges was obtained by subtracting $S_r$(interior) from $S_r$(entire tumor) (see Table 2) to give approximately $\sim S_r$(tumor rim). $\sim S_r$(tumor rim) was significantly larger in non-metastatic tumors ($2.6 \pm 0.5$) than in metastatic tumors ($0.8 \pm 0.3$; $p<.007$ by T-test) before contrast injection. A two dimensional plot of $S_r$(interior) with contrast agent vs. $\sim S_r$(tumor rim) without contrast agent (Figure 4) gives excellent separation between non-metastatic and metastatic tumors - only one non-metastatic tumor falls within the distribution of metastatic tumors.

The average of maximum $T_2^*$ changes before and just after injection of contrast in the tumor and selected muscle regions were calculated and are listed in Table 1 for all the experiments. These changes were calculated based only on those pixels in which $T_2^*$ decreased (see below) in an attempt to emphasize those regions with very high vascular density. Fig. 5 shows the $S_r$(interior) values just after injection of contrast agent as a function of average maximum $T_2^*$ changes. The average maximum $T_2^*$ changes in non-metastatic tumors were higher (see Table 2) and more spatially uniform than those in metastatic tumors. Therefore the combination of maximum $T_2^*$ changes and $S_r$ measurements tends to separate the metastatic and

non-metastatic tumors (Fig. 5), although there is some overlap between the distributions. Contrast media washout rates were not significantly different in non-metastatic and metastatic tumors and combinations of washout kinetics and various texture parameters did not help to separate the two populations.

The values for '$S_{r\text{diff}}$' were also calculated for difference images, i.e. water signal peak height in the first image after contrast injection minus control peak height. These $S_{r\text{diff}}$ values do not clearly distinguish metastatic and non-metastatic tumors because of the very large range of values for metastatic tumors (Table 2). The $I_r$ values (average intensity relative to muscle) and the changes in $I_r$ after contrast media injection do not effectively discriminate between metastatic and non-metastatic tumors. The difference in average values of $A_r$ (irregularity of tumor border) between the metastatic and non-metastatic tumors is also very small (Table 2). Tumor growth rate and tumor size did not correlate well with any of the measures of image texture, tumor architecture, or contrast media dynamics (see Table 1).

The response to the contrast agent within the tumors (but not in muscle) is heterogeneous both among pixels and among spectral components within each voxel [16,17]; there are both increases and decreases in water signal peak height. Analysis of the linewidth of the water resonance in each voxel demonstrates that these early changes are due primarily to changes in linewidth ($T_2^*$) rather than changes in the water signal integral.

In metastatic tumors during the first ~10 minutes after contrast media injection $T_2^*$ decreased in 65% of voxels and increased in 35%. In the voxels with decreased $T_2^*$ the average decrease was 3.2 ± 0.4 msec while in the voxels with increased $T_2^*$ the average increase was 2.3 ± 0.4 msec (errors are standard error of the mean). In non-metastatic tumors $T_2^*$ decreased in 76% of voxels and increased in 24%. The average decrease was 4.8 ± 0.9 msec and the average

increase was 1.4 ± 0.3 msec. Thus, decreases in $T_2^*$ or increases in water signal linewidth were predominant, but more so in non-metastatic tumors than in metastatic tumors.

Gradient echo images synthesized from SI datasets also distinguished between metastatic and non-metastatic tumors based on the image texture. $S_r$ derived from the synthesized gradient echo images was greater in the interior of metastatic tumors than in the interiors of non-metastatic tumors. The difference was statistically significant at the $p < 0.06$ level without contrast agent, and at the $p < 0.02$ with contrast agent.

## DISCUSSION

Surface areas of 3D representations of tumor images (intensity versus xy position) were used as a measure of image texture. The texture of tumor interiors ($S_r$ or $S_{r\text{diff}}$) was significantly 'rougher' in metastatic tumors than in non-metastatic tumors. Differentiation between metastatic and non-metastatic tumors based on texture improved greatly after I.V. injection of the contrast agent. The regions of largest $S_r$ tended to coincide with the regions where decreases in $T_2^*$ were largest following contrast media injection. As a result, the contrast agent accentuated $S_r$, perhaps because regions with high $S_r$ are regions with dense vasculature where the intravascular contrast agent causes large susceptibility gradients. A combination of image texture analysis ($S_r$ after contrast) and blood volume measurement (maximum change in $T_2^*$ after contrast injection) was also effective in distinguishing metastatic and non-metastatic tumors.

Tumor edges were more clearly defined in non-metastatic than in metastatic tumors. The differences were difficult to define precisely because at the present spatial resolution, tumor rims could not be accurately segmented. Nevertheless the approximate values calculated for $S_r$(tumor rim) combined in a 2-dimensional plot with $S_r$(interior) gave excellent separation between

metastatic and non-metastatic tumors. The rather poorly defined edges of metastatic tumors suggest effects of the metastatic tumors on surrounding tissue – perhaps due to infiltration. The very clear separation between the two tumor populations reported here, particularly in Fig. 4, is based on studies of a small number of tumors (12 metastatic and 12 non-metastatic). The sensitivity and specificity implied by the current results may not persist when much larger numbers of tumors are imaged. Nevertheless, the results are encouraging and suggest that a combination of texture and hemodynamic measurements obtained from contrast enhanced high resolution SI may provide optimal separation of metastatic and non-metastatic tumors.

NC100150 had spatially and spectrally heterogeneous effects on $T_2^*$. Although decreases in $T_2^*$ were predominant, there were significant increases in $T_2^*$ in some tumor regions. The prevalence and magnitude of $T_2^*$ increases were greater on average in metastatic than in non-metastatic tumors. There are a number of potential explanations for this effect. NC100150 at the correct concentration can decrease water signal line width by matching magnetic susceptibility between two adjacent regions (26). This is most likely to occur in regions with large veins or dense vasculature with high deoxyhemoglobin levels where plasma NC100150 matches the magnetic susceptibility due to deoxyhemoglobin inside the red blood cells – or where intravascular NC100150 matches high extravascular magnetic susceptibility due to extravasated hemoglobin. Alternatively, apparent changes in $T_2^*$ can occur if the $T_1$ of a narrow component of an inhomogeneously broadened water resonance is increased relative to other components of the resonance (11). Further investigation is needed to properly characterize this phenomenon.

Although we found highly statistically significant differences between metastatic and non-metastatic tumors, there was significant overlap between the two distributions. If similar methods were used in a clinical setting, many metastatic tumors could be reliably identified, but some metastatic tumors would be missed since they fall within or close to the non-metastatic

distribution. This degree of overlap between uniform, stable, highly metastatic and non-metastatic rodent tumors calls into question whether clinical MRI, as currently practiced, can distinguish between malignant and benign lesions in a highly variable population of human patients. Although rodent tumors are far from perfect models for human disease, they share fundamental characteristics of human tumors, e.g., metastatic tumors in both species have regions of high angiogenic activity, rapid and irregular growth, and invasion of surrounding tissue [19,20]. Thus, the present results obtained with rodent tumors are relevant to human disease. As in the case of the present results, hemodynamic and/or textural analysis in studies of breast lesions in patients often yields a relatively narrow distribution for benign lesions, and a broad distribution for metastatic lesions [27]. More work is necessary to increase understanding of why some metastatic tumors fall within the normal tumor distribution and some do not – and what data acquisition and analysis methods should be used to increase our power to resolve the two populations of tumors.

We anticipate that there are several ways in which the sensitivity and specificity of high resolution SI could be increased :

1. The sensitivity and specificity of high resolution SI might increase if measurements of image texture and blood volume excluded necrotic and dormant tumor regions since these regions are not actively metastatic. Many of the tumors shown in Figs. 1 & 2 clearly contain such regions, e.g., regions that do not take up the contrast agent. These regions tend to have relatively low values of the texture parameter, $S_r$. For example, image intensity does not change greatly following contrast media injection in large portions of non-metastatic tumors 4 and 6 and metastatic tumors 4, 6, and 12 and the images are fairly smooth in these regions. Such regions could, in principle, be automatically identified based on response to contrast media but the spatial resolution of the images in the current datasets does not allow accurate segmentation.

Spatial resolution can be increased through the use of much faster spectroscopic imaging methods (see below).

**2.** The sensitivity and specificity of high resolution SI might also be improved through use of additional features of the water signal lineshape. The results presented here are based on water signal peak height in each voxel. Peak height is sensitive to relatively subtle changes in water signal lineshape, since it is determined by the combined contributions of all the Fourier components of the water signal. However, other features of the water resonance might provide improved discrimination between metastatic and non-metastatic tumors. For example, images could be synthesized from the amplitudes, linewidths, or resonance frequencies of individual components of the water signal, asymmetry of various components, or higher moments of the water resonance.

3. Further improvement could come through imaging multiple slices through tumors. Due to the time required for acquisition of phase encoded spectroscopic images, only single slice in each tumor was imaged. This could lead to sampling artifacts, i.e. the imaged slice may not always have accurately represented the entire tumor. In the future, fast imaging with higher spatial resolution over larger volumes (obtained using echo planar spectroscopic imaging methods, see below) will allow more detailed examination of the whole tumor.

4. Improved sensitivity and specificity of dynamic, contrast enhanced SI after injection of contrast agent might be achieved using fast spectroscopic imaging methods (also known as echo planar spectroscopic imaging [28-30]). This approach provides SI datasets with much higher temporal, spatial, and spectral resolution [12,13] than that achieved with the conventional phase encoding method used here. Thus, temporal resolution could be increased during the early phase of contrast media uptake. During the later phase of contrast media distribution, larger volumes of tissue could be imaged with higher spatial resolution. This is achieved at the cost of some

decrease in signal-to-noise ratio [12]. However the SI datasets do not appear to be signal-to-noise ratio limited, and work in this laboratory [12] and other laboratories [10,13] demonstrates that fast spectroscopic imaging provides high quality MR images.

The purpose of the present experiments was to evaluate the utility of high resolution SI for accurate classification of metastatic v.s. non-metastatic tumors, rather than to compare SI with conventional MRI methods. Therefore the question of whether SI distinguishes metastatic and non-metastatic tumors more reliably than conventional MRI was not directly addressed by the present experiments. The very qualitative comparison of gradient echo imaging and SI reported here suggests that both approaches can distinguish between metastatic and non-metastatic tumors based on textural parameters - but that SI identifies metastatic tumors with a higher level of confidence. However, the synthetic gradient echo images did not have optimal signal-to-noise ratio, and both the gradient echo and spectroscopic images had sub-optimal spatial and temporal resolution. Work is currently underway to thoroughly compare the two approaches under optimal conditions and to determine whether the putative advantages of high resolution SI are in part responsible for the strong statistical differences between metastatic and non-metastatic tumors reported here.

## CONCLUSIONS

The results of the present study of rodent prostate tumors suggest that contrast enhanced high resolution spectroscopic imaging can discriminate between metastatic and non-metastatic tumors based on measures of image texture, tumor edges, and contrast agent dynamics. SI may be particular useful in this context because the water resonance in tumors is often complex and

has multiple resolvable components – and because effects of superparamagnetic contrast agents are likely to be spectrally heterogeneous [16,17].

## ACKNOWLEDGEMENTS

Support for this work was provided by the American Cancer Society (CCE-86272), the National Cancer Institute (1RO1CA76476 & 1RO1CA78803), and Nycomed Amersham, Princeton, NJ. GSK thanks Dr. Dennis Fujii for many helpful discussions and Dr. Martin Lipton for advice and support.

## Reference


1. Rinker-Schaeffer CW, Partin AW, Isaacs WB, Coffey DS, Isaacs JT. Molecular and cellular changes associated with the acquisition of metastatic ability by prostatic cancer cells. Prostate 1994;25:249-265.
2. Garnick M. The dilemmas of prostate cancer. Scientific American 1994:52 -59.
3. Moody-Ayers SY, Wells CK, Feinstein AR. 'Benign' tumors and 'early detection' in mammography-screened patients of a natural cohort with breast cancer. Arch Intern Med ;160:1109-1115.
4. Frouge C, Guinebretier J-M, Contesso G, Di Paola R, Blery M. Contrast Enhancement in Dynamic Magnetic Resonance Imaging of the Breast and Tumor Angiogenesis. Investigative Radiology 1994;29:1043-1049.
5. Furman-Haran E, Margalit R, Grobgeld D, Degani H. Dynamic contrast-enhanced magnetic resonance imaging reveals stress- induced angiogenesis in MCF7 human breast tumors. Proc Natl Acad Sci U S A 1996;93:6247-6251.
6. Heywang S, Hahn D, Schmidt H. Magnetic Resonance Imaging of the Breast Using Gd-DTPA. J Comput Assist Tomogr 1986;10:681-686.
7. Pham CD, Roberts TP, van Bruggen N, Melnyk O, Mann J, Ferrara N, Cohen RL, Brasch RC. Magnetic resonance imaging detects suppression of tumor vascular permeability after administration of antibody to vascular endothelial growth factor. Cancer Invest 1998;16:225-230.
8. Dixon WT. Simple Proton Spectroscopic Imaging. Radiology 1984;153:189-194.
9. Glover GH. Multipoint Dixon Technique for Water and Fat proton and Susceptibility Imaging. Journal of Magnetic Resonance Imaging 1991;1:521-530.

10. Hilaire L, Wehrli FW, Song HK, Hopkins JA. High-speed spectroscopic imaging at 4T for R2* measurement of individual spectral components. International Society for Magnetic Resonance in Medicine 1999:257.

11. Oikawa H, Al-Hallaq HA, Lewis MZ, River JN, Kovar DA, Karczmar GS. Spectroscopic imaging of water resonance with short repetition time to study tumor response to hyperoxia. Magn. Reson. Med. 1997;38:27-32.

12. Kovar DA, Al-Hallaq HA, Zamora MA, River JN, Karczmar GS. Fast spectroscopic imaging of water and fat resonances to improve the quality of MR images. Acad Radiol 1998;5:269-275.

13. Sarkar S, Heberlein K, Metzger GJ, Zhang X, Hu X. Applications of high-resolution echoplanar spectroscopic imaging for structural imaging. J Magn Reson Imaging 1999;10:1-7.

14. Al-Hallaq HA, Zamora M, Fish BL, Farrell A, Moulder JE, Karczmar GS. MRI measurements correctly predict the relative effect of tumor oxygenating agents on hypoxic fraction in rodent BA1112 tumors. Int J Radiat Oncol Biol Phys 2000;in press.

15. Kuperman V, River JN, Karczmar GS. Chemical Shift Imaging Study of Tumor Response to Hyperoxia. International Society for Magnetic Resonance in Medicine 1994;3:1333.

16. Karczmar GS, Fan X, Al-Hallaq HA, Zamora M, River JN, Rinker-Schaeffer C, Zaucha M, Tarlo K, Kellar K. Uptake of a Superparamagnetic Contrast Agent Imaged by MR with High Spectral and Spatial Resolution. Magnetic Resonance in Medicine 2000;43:633-639.

17. Karczmar GS, Fan X, Al-Hallaq H, River JN, Tarlo K, Kellar K, Zamora M, Rinker-Schaeffer C, Lipton MJ. Functional and Anatomic Imaging of Tumor Vasculature: High

Resolution MR Spectroscopic Imaging Combined with a Superparamagnetic Contrast Agent. Academic Radiology 2000;in press.

18. Karczmar GS, V.Y. K, Lewis MZ, River JN, Lubich L, Halpern H. High Resolution Spectroscopic Images of Tumors. ISMRM 1995.

19. Tennant TR, Kim H, Sokoloff M, Rinker-Schaeffer CW. The dunning model. Prostate ;43:295-302.

20. Lucia MS, Bostwick DG, Bosland M, Cockett AT, Knapp DW, Leav I, Pollard M, Rinker-Schaeffer C, Shirai T, Watkins BA. Workgroup I: rodent models of prostate cancer. Prostate 1998;36:49-55.

21. Kellar KE, Fujii DK, Gunther WH, Briley-Saebo K, Bjornerud A, Spiller M, Koenig SH. NC100150 Injection, a preparation of optimized iron oxide nanoparticles for positive-contrast MR angiography. J Magn Reson Imaging 2000 May;11:488-494.

22. Brown TR, Kincaid BM, Ugurbil K. NMR chemical shift imaging in three dimensions. Proc Natl Acad Sci U S A 1982;79:3523-3526.

23. Maudsley AA, Hilal SK, Perman WH, Simon HE. Spatially resolved high resolution spectroscopy by "four-dimensional" NMR. Journal of Magnetic Resonance 1983;51:147-152.

24. Fan X, River JN, Zamora M, Rinker-Schaeffer C, Karczmar GS. Calculation of pure absorption images from spectroscopic data increases image contrast and resolution. International Society for Magnetic Resonance im Medicine 1999.

25. Bauer WR, Hiller KH, Roder F, Rommel E, Ertl G, Haase A. Magnetization exchange in capillaries by microcirculation affects diffusion-controlled spin-relaxation: a model which describes the effect of perfusion on relaxation enhancement by intravascular contrast agents. Magn Reson Med 1996;35:43-55.

26. Shuter B, Wang SC, Roche J, Briggs G, Pope JM. Relaxivity of Gd-EOB-DTPA in the normal and biliary obstructed guinea pig. J Magn Reson Imaging 1998;8:853-861.

27. Kuhl CK. MRI of breast tumors. Eur Radiol ;10:46-58.

28. Posse S, Tedeschi G, Risinger R, Ogg R, Le Bihan D. High speed 1H spectroscopic imaging in human brain by echo planar spatial-spectral encoding. Magn Reson Med 1995;33:34-40.

29. Doyle M, Mansfield P. Chemical Shift Imaging: A Hybrid Approach. Magnetic Resonance in Medicine 1987;5:255-261.

30. Mansfield P. Spatial Mapping of the Chemical Shift in NMR. Magnetic Resonance in Medicine 1984;1:370-386.

**Table 1.** Summary of the tumor growth rate, tumor area, relative surface area ($S_r$), average intensity ratio of tumor to muscle ($I_r$), and the average maximum $T_2^*$ changes in tumor and muscle before and just after injection of contrast agent. $\Delta T_2^*$ was calculated using only those pixels in which $T_2^*$ decreased.

| | Tumor growth rate ($cm^3$/day) | Imaging tumor area ($cm^2$) | Relative surface area of interior & entire tumor ($S_r$) | Intensity ratio of interior & entire tumor to muscle ($I_r$) | Average max $T_2^*$ change for tumor & muscle (ms) |
|---|---|---|---|---|---|
| **Non-Metastatic Tumors** | | | | | |
| 1 | 0.05 | 0.87 | 2.77 & 4.35 | 1.61 & 1.42 | 8.20 & 2.84 |
| 2 | 0.07 | 0.50 | 4.32 & 7.62 | 2.01 & 1.76 | 6.77 & 3.53 |
| 3 | 0.03 | 0.50 | 4.12 & 6.40 | 1.72 & 1.45 | 1.37 & 2.44 |
| 4 | 0.05 | 1.11 | 1.13 & 1.36 | 0.75 & 0.64 | 1.71 & 2.18 |
| 5 | 0.01 | 0.23 | 4.34 & 7.28 | 1.91 & 1.58 | 6.18 & 1.92 |
| 6 | 0.20 | 0.45 | 4.53 & 10.93 | 2.64 & 2.07 | 3.67 & 2.54 |
| 7 | 0.10 | 0.68 | 3.10 & 5.91 | 1.83 & 1.52 | 4.52 & 2.61 |
| 8 | 0.10 | 0.57 | 4.49 & 9.05 | 2.02 & 1.63 | 9.09 & 2.58 |
| 9 | 0.14 | 1.19 | 4.15 & 5.78 | 1.99 & 1.73 | 9.08 & 2.53 |
| 10 | 0.02 | 1.06 | 3.99 & 6.90 | 1.78 & 1.41 | 2.20 & 3.00 |
| 11 | 0.04 | 2.05 | 1.71 & 3.07 | 1.30 & 1.22 | 1.78 & 1.55 |
| 12 | 0.03 | 1.03 | 2.71 & 3.52 | 0.97 & 0.98 | 2.67 & 2.52 |
| **Metastatic Tumors** | | | | | |
| 1 | 0.12 | 1.21 | 4.33 & 5.36 | 1.96 & 1.70 | 2.06 & 3.08 |
| 2 | 0.06 | 0.48 | 5.26 & 3.81 | 1.38 & 1.04 | 2.66 & 2.61 |
| 3 | 0.04 | 0.50 | 4.77 & 5.45 | 1.28 & 1.16 | 3.55 & 3.14 |
| 4 | 0.14 | 1.05 | 4.08 & 5.71 | 1.64 & 1.52 | 0.92 & 2.98 |
| 5 | 0.25 | 1.27 | 6.33 & 8.19 | 2.19 & 1.81 | 2.93 & 1.90 |
| 6 | 0.03 | 1.34 | 7.58 & 10.34 | 2.50 & 1.76 | 2.70 & 1.08 |
| 7 | 0.07 | 1.67 | 11.40 & 10.69 | 2.01 & 1.60 | 5.09 & 2.72 |
| 8 | 0.15 | 1.60 | 8.55 & 9.94 | 2.04 & 1.76 | 4.69 & 4.35 |
| 9 | 0.21 | 1.30 | 17.86 & 17.87 | 2.95 & 2.26 | 3.03 & 7.36 |
| 10 | 0.05 | 0.60 | 5.36 & 6.76 | 1.52 & 1.30 | 4.48 & 2.47 |
| 11 | 0.11 | 2.42 | 6.72 & 7.27 | 1.55 & 1.41 | 3.72 & 1.51 |
| 12 | 0.04 | 0.99 | 5.15 & 5.37 | 1.45 & 1.24 | 2.06 & 2.09 |

**Table 2.** Average values of parameters with standard errors of the means for non-metastatic and metastatic tumors.

| Calculated Parameter | Non-Metastatic Tumor | | Metastatic Tumor | |
|---|---|---|---|---|
| | No contrast agent | With contrast agent | No contrast agent | With contrast agent |
| †$S_r$(interior tumor) | 3.45±0.33 | 4.84±0.63 | 7.28±1.13 | 9.59±0.93 |
| $S_r$(entire tumor) | 6.01±0.77 | 7.20±1.17 | 8.06±1.10 | 10.24±0.95 |
| †$S_r$(tumor rim) | 2.6±0.5 | 2.4±0.6 | 0.8±0.3 | 0.6±0.5 |
| $I_r$(interior tumor) | 1.71±0.15 | 1.66±0.16 | 1.87+0.14 | 2.03±0.15 |
| $I_r$(entire tumor) | 1.45±0.11 | 1.37±0.11 | 1.55±0.10 | 1.65±0.11 |
| †$T_2^*$(tumor) early changes | 4.77±0.86 | | 3.16+0.35 | |
| $T_2^*$(muscle) early changes | 2.52±0.15 | | 2.94±0.47 | |
| †$S_{rdiff}$(interior tumor) | 40.83±5.26 | | 158.33±58.31 | |
| †$S_{rdiff}$(entire tumor) | 52.17±6.70 | | 141.64±48.52 | |
| $A_r$ | 1.78±0.12 | | 1.98+0.23 | |

†The parameters for metastatic and non-metastatic tumors were significantly different.

**FIGURE CAPTIONS:**

**Figure 1.** Images of non-metastatic tumors: (A) control peak height images, (B) edge enhanced images, and (C) difference images ('first image after contrast media injection' minus 'control images before contrast injection').

**Figure 2.** Metastatic tumors: (A) control peak height images, (B) edge enhanced images, and (C) difference images ('first image after contrast media injection' minus 'control images before contrast injection').

**Figure 3.** Image texture**,** $S_r$ (arbitrary units) in tumor interiors for metastatic and non-metastatic tumors; $S_r$ before contrast media injection is plotted against $S_r$ after contrast media injection. The manually chosen dotted line suggests the optimal separation between the two tumor populations.

**Figure 4.** Image texture, $S_r$ (interior) measured after contrast media injection plotted against ~$S_r$(tumor rim) measured before contrast media injection. The manually chosen dotted line suggests the optimal separation between the two tumor populations.

**Figure 5.** Image texture, $S_r$ over the interior of tumor after contrast agent injection as a function of the average maximum $T_2^*$ changes over tumor just after injection of contrast agent. The manually chosen dotted line suggests the optimal separation between the two tumor populations.

**Figure 1**

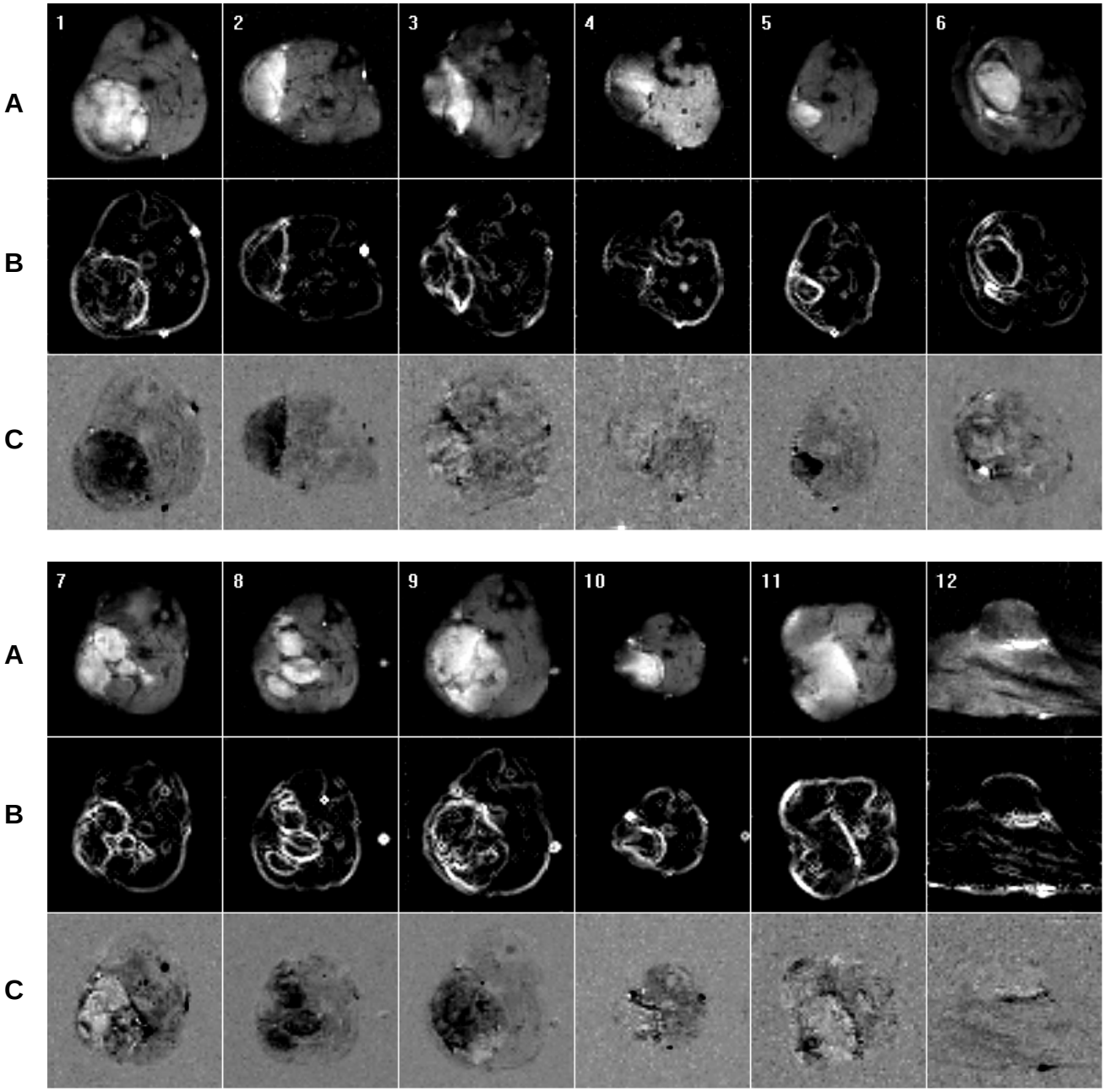

**Figure 2**

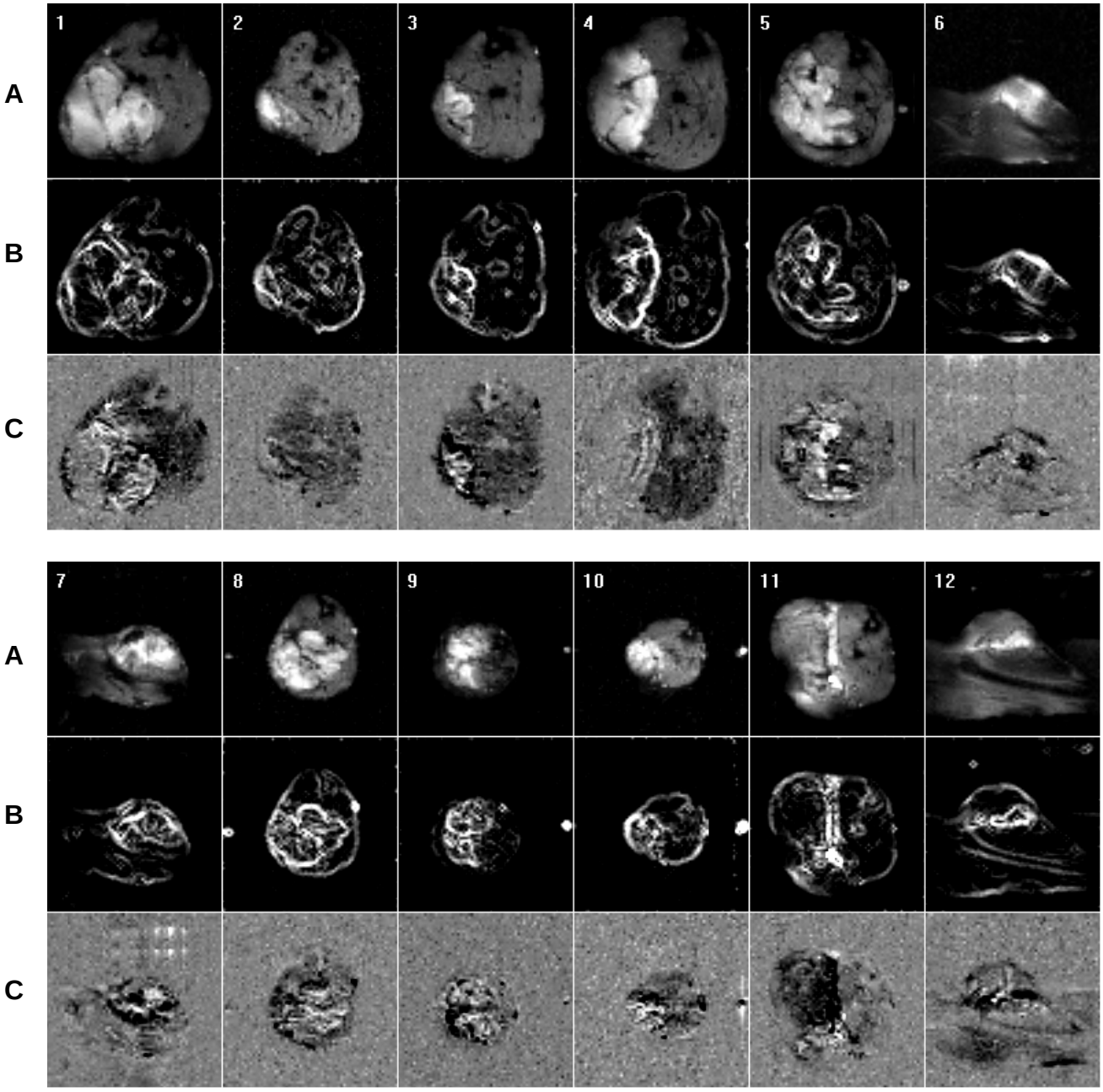

**Figure 3**

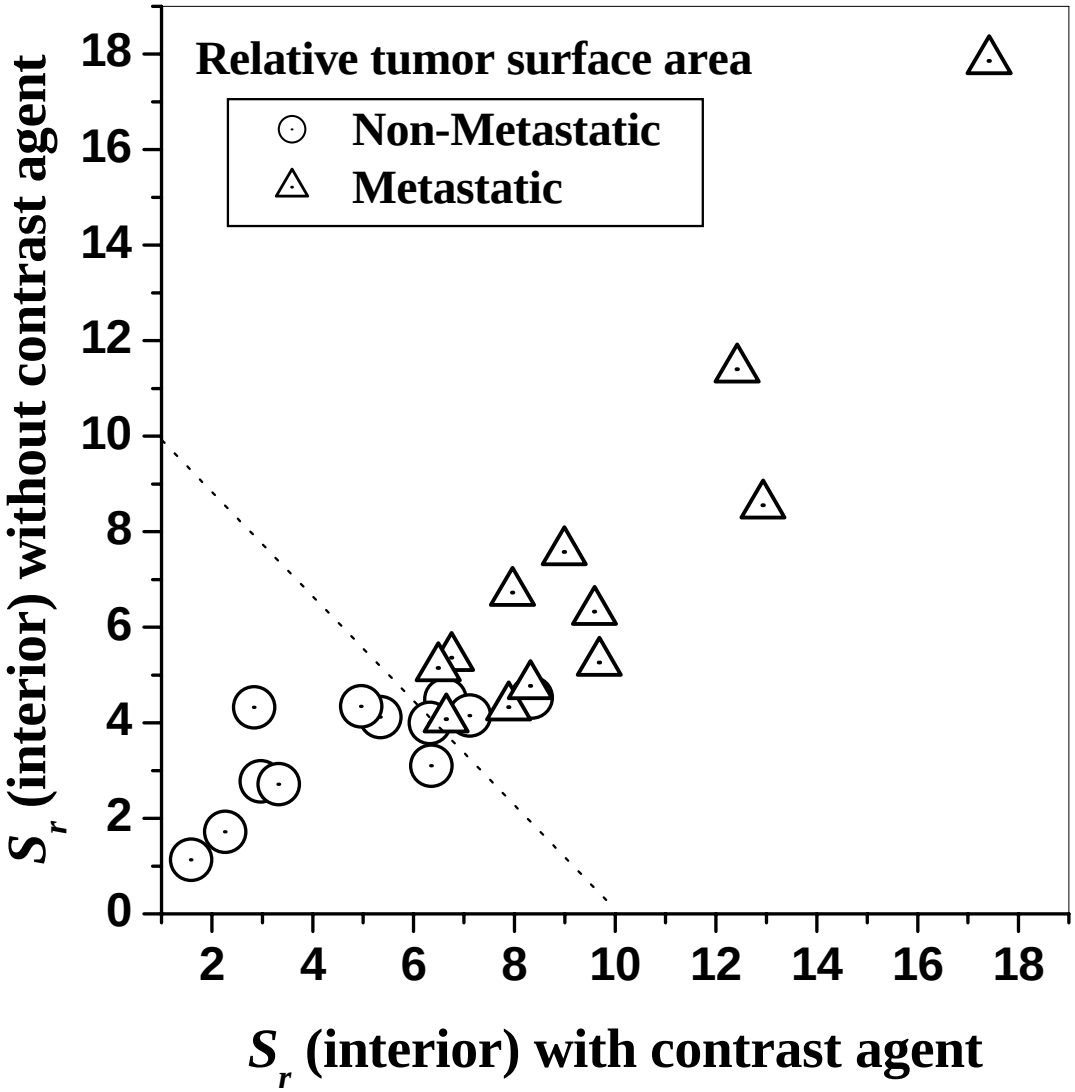
Relative tumor surface area
Non-Metastatic
Metastatic
$S_r$ (interior) without contrast agent
$S_r$ (interior) with contrast agent
0
2
4
6
8
10
12
14
16
18

**Figure 4**

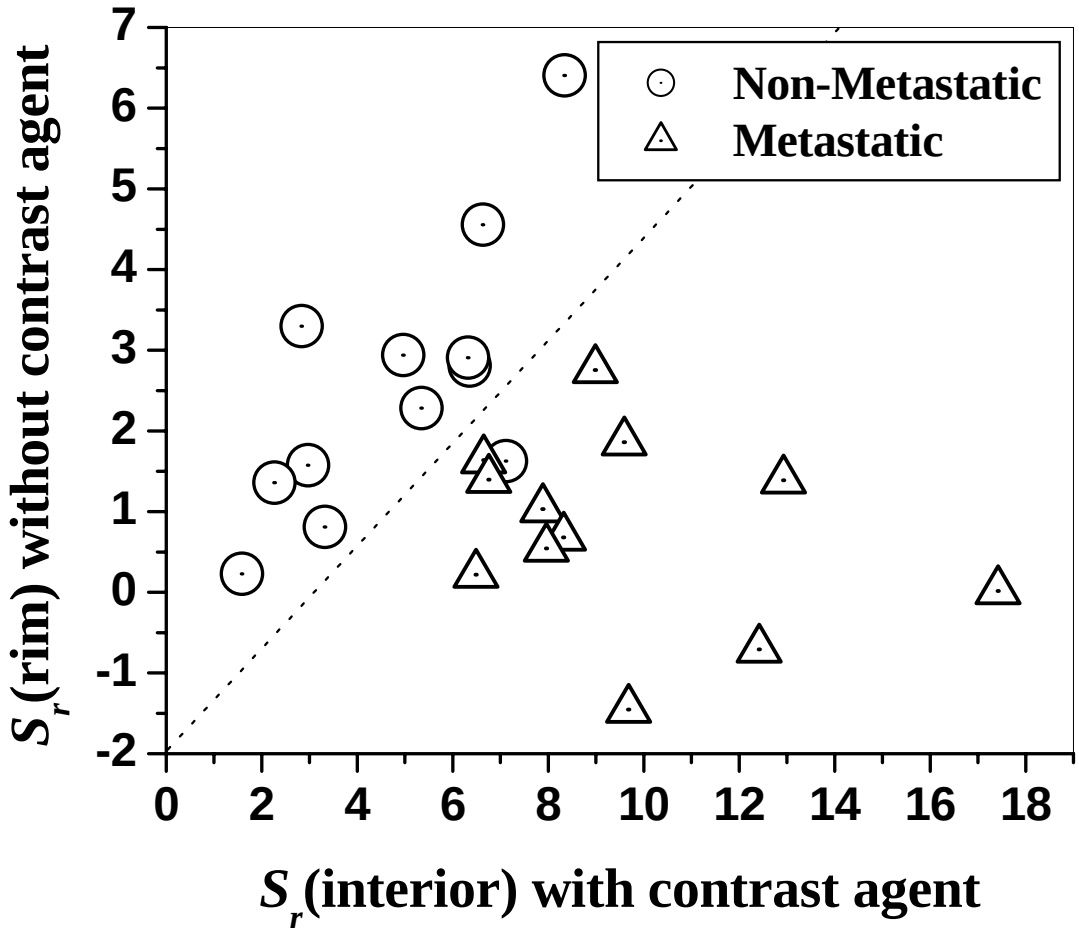
Non-Metastatic
Metastatic
$S_r$(rim) without contrast agent
$S_r$(interior) with contrast agent
7
6
5
4
3
2
1
0
-1
-2
0
2
4
6
8
10
12
14
16
18

**Figure 5**

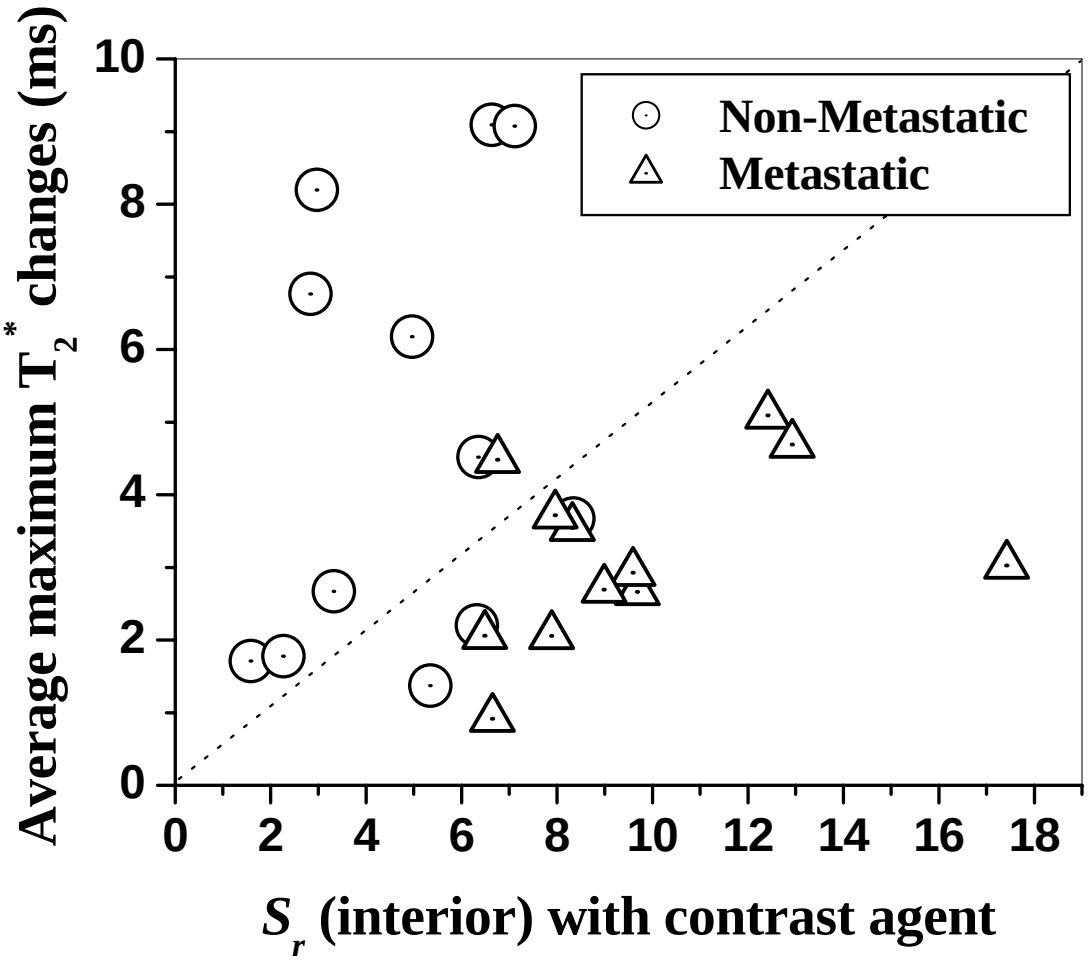
Average maximum $T_2^*$ changes (ms)
$S_r$ (interior) with contrast agent
Non-Metastatic
Metastatic
0
2
4
6
8
10
12
14
16
18

Magnetic Resonance in Medicine 52:193–196 (2004)

# Fourier Components of Inhomogeneously Broadened Water Resonances in Breast: A New Source of MRI Contrast

Milica Medved,[1] Gillian M. Newstead,[1] Xiaobing Fan,[1] Weiliang Du,[1] Yiping P. Du,[3] Peter M. MacEneaney,[1] Rita M. Culp,[1] Frederick Kelcz,[4] Olufunmilayo I. Olopade,[2] Marta A. Zamora,[1] and Gregory S. Karczmar[1]*

**High spectral and spatial resolution (HiSS) MR data were acquired at 1.5 T using echo-planar spectroscopic imaging from patients with suspicious breast lesions. The water resonances in small voxels are inhomogenously broadened and often have distinct components. Images were calculated with intensity proportional to the Fourier components of the water resonance in each voxel at different offsets from the peak frequency. The results demonstrate that in breast the off-peak Fourier component images of water are qualitatively different from those derived from the peak height of the water resonance. These differences most likely reflect underlying anatomy or physiology. In conventional images, the superposition of the various Fourier components of the water signal may cause loss of detail. The synthesis of water Fourier component images from high spectral and spatial resolution data may provide a new form of contrast, and increase sensitivity to subvoxel physiology and anatomy. Magn Reson Med 52: 193–196, 2004. © 2004 Wiley-Liss, Inc.**

**Key words: high spectral and spatial resolution MRI; MRI of breast; magnetic susceptibility imaging; subvoxel anatomy and physiology; image contrast**

The water resonance from small voxels in tissue is often inhomogeneously broadened, and sometimes contains multiple resolved components (1–5). These distinct components can be identified in water signal line shapes from single voxels in high spectral and spatial resolution (HiSS) images (5,6). In addition, distinct components can be identified based on spectrally inhomogeneous changes in the water resonance caused by changes in blood deoxyhemoglobin (1,7,8) or injected contrast agents (3,5,9,10). A priori arguments and experimental evidence suggest that the distinct components of the water resonance come from subvoxelar, perhaps microscopic (3,5,9,10) environments that cannot be resolved by conventional imaging.

If the components of the water resonance represent specific subvoxel anatomic and physiologic features, it follows that images of these components may provide unique and potentially useful information. The purpose of this report is to demonstrate that HiSS imaging in human breast generates reproducible images of different Fourier components (Fourier component images, FCIs) of the water resonance from very small voxels, and that there are marked differences between different FCIs. The work described here does not attempt to correlate the information in FCIs with patient diagnosis, but rather to evaluate contrast in these novel images.

## PATIENTS AND METHODS

### Patient Population

Data were acquired from women with suspicious breast lesions found on mammography. Standard clinical MRI scans were prescribed for these patients prior to biopsy primarily to determine whether there was disease extending beyond the focal abnormality identified on mammograms. A total of 13 patients was included in this study, of which five were confirmed by biopsy to have invasive ductal carcinoma (IDC), two to have ductal carcinoma in situ (DCIS), three to have IDC and DCIS, one to have IDC with sclerosing adenosis, and one to have fibroadenoma. In one patient, a lumpectomy scar was imaged.

### Data Acquisition

HiSS scans were incorporated into these standard exams, pre- and post-contrast agent administration. In addition, several volunteers with no breast abnormalities were scanned without the use of contrast agent. In studies of a limited number of patients (n = 4) with IDC, consecutive HiSS images were acquired 30–40 min postcontrast injection, when the changes due to contrast agent washout are negligible between the scans. Subjects were scanned under a protocol approved by the Institutional Review Board after informed consent was obtained.

Images were obtained on a 1.5 T clinical MRI scanner (General Electric, Milwaukee, WI) equipped with ECHO SPEED PLUS™ gradients with maximum slew rate of 120 mT/m/s and maximum amplitude of 23 mT/m, using a dedicated phased array breast coil. HiSS images were acquired from single selected slices using echo planar spectroscopic imaging (EPSI) (11,12). Immediately before the HiSS images were acquired, shimming was performed using the standard GE protocol, in which gradient echo im-

[1]Department of Radiology, University of Chicago, Chicago, Illinois.

[2]Department of Medicine, University of Chicago, Chicago, Illinois.

[3]Department of Psychiatry, University of Colorado Health Sciences Center, Boulder, Colorado.

[4]Department of Radiology, University of Wisconsin at Madison, Madison, Wisconsin.

Grant sponsor: NCI; Grant numbers: 1RO1CA76476; 1RO1CA78803; Grant sponsor: Army Breast Cancer Research Program; Grant number: BC981147; Grant sponsors: Paul C. Hodges Society, Falk Medical Research Trust (to O.I.O.), Doris Duke Distinguished Clinical Scientist (to O.I.O.).

*Correspondence to: Gregory S. Karczmar, Ph.D., Department of Radiology, MC 2026, University of Chicago, 5841 S. Maryland Ave., Chicago, IL 60637. E-mail: gskarczm@midway.uchicago.edu

Received 22 July 2003; revised 19 December 2003; accepted 4 February 2004.

DOI 10.1002/mrm.20115
Published online in Wiley InterScience (www.interscience.wiley.com).

ages with several echoes are taken in all three planes and phase differences between echoes are used to calculate adjustments to shim currents. The same shim and gain parameters were used to obtain both pre- and post-contrast HiSS images.

The EPSI sequence was composed of slice selection (slice thickness 4 mm) followed by phase encoding (256 phase-encoding steps) and acquisition of 128 gradient echoes using trapezoidal gradient pulses with alternating polarity. A "crusher" gradient was applied at the end of the echo train to eliminate artifacts due to residual transverse magnetization. Each gradient echo was sampled either at 256 (due to hardware limitations) or at 384 points (after a system upgrade). The data were digitized at a bandwidth of ± 62.5 kH and the time between the centers of gradient echoes was ~3.0 ms. The proton free induction decay (FID) was sampled for a total of 384 ms and the time between excitations (TR) was 500 ms. The resulting data had an in-plane spatial resolution of less than 1 mm (field-of-view 24 cm or less) and spectral resolution of ~2.6 Hz. The spatial resolution was the same in both readout and phase-encoding direction, resulting in a reduced field-of-view in the latter when a 384 × 256 image was acquired. The spectral bandwidth (~333 Hz) was sufficient to resolve the water and fat resonances, which are separated by ~220 Hz at 1.5 T. Both spectral and spatial resolutions were sufficient to avoid significant truncation artifacts. Sagittal slices were imaged with the readout gradient applied in the A/P direction to minimize artifacts due to respiratory and cardiac motion.

The shimming and data acquisition protocol was tested by imaging water phantoms containing 2 mM copper sulfate using the EPSI pulse sequence with the same parameters as those used for breast imaging (described above). The water resonance in all image voxels sampled was a symmetrical Lorentzian with line width of less than 2 Hz. No artifacts due to poor shimming or eddy currents were detected.

### Data Analysis and Synthesis of Images

A 3D Fourier transform with respect to two *k*-space axes and the evolution of the FID (5,6,13–15) provided high-resolution spectra of the water and fat resonances associated with each voxel in the image. The highest intensity spectral component was identified in each voxel, and the one in the voxel with the highest signal was identified as either water or fat signal. Based on the frequency offset from this seed pixel, the highest peak in the neighboring voxel containing the highest signal was identified as either water or fat. Frequency foldback was accounted for, as well as the possibility of N/2 ghosting in the spectral dimension. This process was repeated using a region-growing program until all the voxels had been classified, and hence the fat and water frequency map obtained. This robust algorithm relies on the fact that there are no sharp macroscopic gradients within the breast, and is described in detail in our earlier publication. (15)

For examination of spectra from individual voxels, the water line from each voxel was phased by requiring that the integral of the imaginary spectrum in the narrow vicinity of the spectral peak equals zero. We found this to be equivalent to a requirement that the complex phase of the spectrum be zero at the peak frequency. However, the phasing algorithm in its present form sometimes results in errors. Therefore, magnitude spectra were used for image synthesis. Water signal peak height images provide a combination of $T_1$ and $T_2^*$ weighting. The $T_2^*$ weighting was dominant in these data because the FID sampling time of 384 ms provided strong $T_2^*$ contrast, while the TR of 500 ms provided only moderate $T_1$ weighting.

After the highest intensity spectral component was identified, images were synthesized with intensity proportional to the amplitude of the water spectrum at various offsets from the peak in increments of 2.6 Hz (i.e., 1 frequency bin). These images are referred to in the following as FCIs (Fourier component images).

## RESULTS

Figure 1 shows a postcontrast image of a breast with a high-grade infiltrating ductal carcinoma (Fig. 1a), with the lesion outlined and enlarged in Fig. 1b. In Fig. 1b the locations of eight representative voxels are indicated and water spectra from these voxels are shown in Fig. 1c–j. The solid and dashed lines correspond to two datasets acquired consecutively, 40 min postcontrast. The underlying spectra acquired in the two scans are highly reproducible in intensity and structure. For example, water resonances with two resolvable components in one dataset show two very similar resolvable components in the second dataset.

The complexity of the water resonance in many voxels is reflected in images of the Fourier components of the water resonance. FCIs at 5–30 Hz from the peak of the water resonance often contain features, well above the noise level, that are different from images of the peak of the water resonance (at 0 Hz). In particular, $FCI_{+10}$ (the FCI generated at 10 Hz offset from the main peak) shows marked differences from $FCI_0$ more consistently then other FCIs. Figure 2 shows a $T_1$-weighted image (Fig. 2a), acquired precontrast injection in three patients with suspicious breast lesions. Pre-contrast FCIs at 0 Hz ($FCI_0$) (Fig. 2b) and +10 Hz ($FCI_{+10}$) (Fig. 2c) from the peak of the water resonance are shown in detail for the 60 × 60 voxel area surrounding the lesion, as outlined in Fig. 2a.

To highlight the variations in contrast among FCIs, the $FCI_{+10}$'s were subtracted from the corresponding $FCI_0$'s, and the differences are shown in Fig. 2d. Before subtraction, the average image intensity of each FCI within the region outlined in Fig. 2a was normalized to 1.0. As a result, the differences between the normalized images of the lesion and surrounding tissue emphasize differences in image contrast rather than image intensity. The difference images show coherent structures that are well above the noise level—which can be estimated from the variations in image intensity in regions where there is very little water signal. In particular, the dark structures correspond to features present in the off-zero FCI, but not in the peak height image ($FCI_0$), indicating a non-Lorentzian water line shape. Some structures are elongated and appear to be blood vessels. In addition, there are frequent "black dots" in and near lesions, which may come from blood vessels perpendicular to the image slices. The blood vessels may

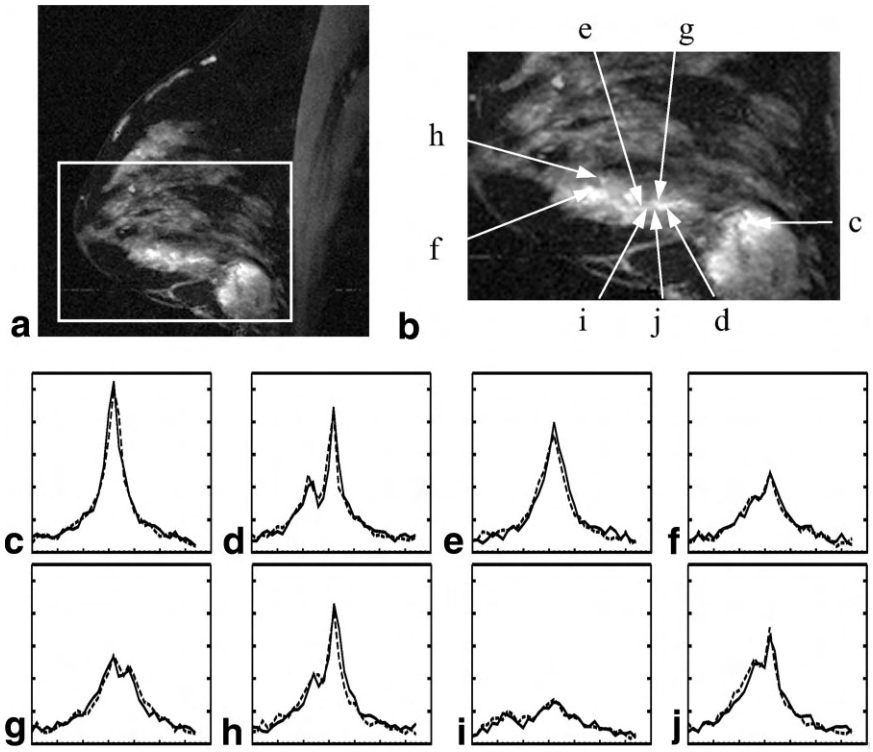


FIG. 1. **a:** A sagittal, water peak height HiSS image for a patient with a high-grade invasive ductal carcinoma lesion. **b:** The lesion outlined in **a** is enlarged to show the position of voxels for which the water spectra are shown in (**c–j**). **c–j:** Spectra from two repeated measurements are shown for comparison (solid and dashed lines), for the eight voxels noted in **b**.

have a different relative intensity in $FCI_0$ and $FCI_{+10}$, due to the magnetic susceptibility of deoxyhemoglobin.

## DISCUSSION

Previous work demonstrated that high spectral and spatial resolution imaging provides strong $T_2^*$ contrast while showing excellent anatomic detail relative to conventional MRI (5,6,14,16,17). The present work suggests that Fourier component imaging can be an additional, novel source of contrast in HiSS data. The preliminary results presented here demonstrate that FCIs at different offsets from the peak of the water resonance differ markedly. This would not be the case if the water resonance in each voxel was a homogeneously broadened Lorentzian. It is not known at present whether the same features seen in FCIs could also be emphasized using more commonly used contrast mechanisms, i.e., $T_1$, $T_2$, $T_2^*$, diffusion, or magnetization transfer-weighting. If the FCIs provide an independent contrast mechanism, HiSS MRI could be combined with other methods for contrast enhancement to increase the amount of information offered by MRI. The present results do not indicate whether Fourier component images are clinically useful, as there is no evidence as yet that FCIs of cancers are different from FCIs of benign lesions. More work is required to optimize acquisition and processing of FCI images before clinical applications can be evaluated.

Motion artifacts are a potential source of error in the calculations of FCIs because they can cause contamination of the water spectrum in each voxel by water signals from

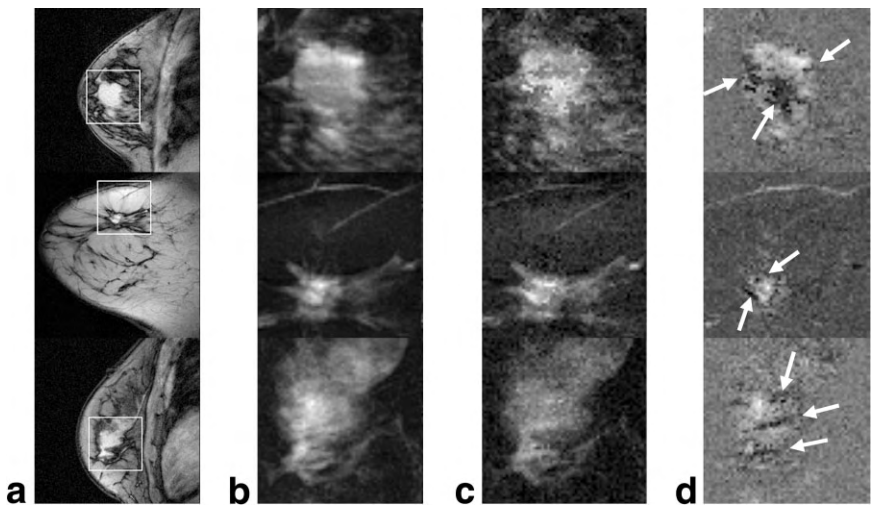


FIG. 2. Pre-contrast $T_1$-weighted (**a**) images for three patients with breast lesions (diagnosis, top to bottom: intraductal and invasive ductal adenocarcinoma, infiltrating ductal carcinoma, fibroadenoma). Precontrast FCIs for 0 Hz (**b**) and +10 Hz (**c**), as well as their difference (**d**), for the region outlined in **a**. Arrows in **d** point to new features that appear in off-zero FCIs.

nearby voxels. Since the contaminating signal may be at a different frequency from the local water resonance, this could lead to broadening of the water resonance, and in some cases might appear as an off-resonance component. However, in our experience this artifact is easily observable in the phase-encoding direction in water peak height ($FCI_0$) images, and is of much lower signal intensity than the main image. The HiSS images presented here do not show any such aliasing, and Fig. 1c-j shows that resolved water components are of comparable intensity. Therefore, the water components we detect are unlikely to result from motion artifacts.

It is not likely that the spectrally inhomogeneous broadening could be caused by imperfect shimming. In the small voxels used in HiSS MRI, the macroscopic $B_0$ gradients across each voxel are small and, to a very good approximation, linear, and are likely to produce modest broadening of the water resonance, but no "peak splitting." $B_0$ generally varies slowly and smoothly within the breast, and we do not observe large gradients in the vicinity of voxels with complex water signals. Finally, the Fourier component images in Fig. 2 often show discrete, elongated structures that have the appearance of blood vessels, which would not be seen if the water line structure resulted simply from poor shimming. It is more likely that the peak splitting and inhomogeneous broadening are the result of subvoxelar variations in magnetic susceptibility. For example, at 1.5 T deoxyhemoglobin in a capillary can cause a gradient of 30 Hz over a distance of 5 μ, which is equivalent to ~15 Gauss/cm, and hemosiderin may cause even larger gradients. It is plausible that each FCI may represent a discrete subvoxelar environment with characteristic magnetic susceptibility—analogous to the chemical shift imaging of metabolites where images of the signal at a specific frequency produce images of a specific metabolite (18,19). Thus, HiSS MR may be able to resolve subvoxelar environments, inaccessible via conventional imaging, potentially increasing sensitivity to subvoxelar anatomy and physiology. This hypothesis must be tested by direct correlation of Fourier component images with histology.

In conclusion, we show that the various Fourier components of the water resonances in small voxels can produce images with differing contrast and anatomic detail. This contrast is likely the result of subvoxelar breast anatomy or physiology, a contrast mechanism that likely cannot be duplicated using other methods. The present results do not identify the sources of contrast in FCI images, and do not indicate whether Fourier component images are clinically useful. However, the FCIs shown here reveal new features that could potentially aid the evaluation of suspicious breast lesions.

## ACKNOWLEDGMENTS

G.S.K. thanks Dr. Alan Koretsky and Dr. Charles Springer for helpful advice and the American Cancer Society volunteers of Will and Grundy Counties, Illinois, for enthusiastic support.

## REFERENCES

1. Al-Hallaq HA, Fan X, Zamora M, River JN, Moulder JE, Karczmar GS. Spectrally inhomogeneous BOLD contrast changes detected in rodent tumors with high spectral and spatial resolution MRI. NMR Biomed 2002;15:28–36.
2. Karczmar GS, Fan X, Al-Hallaq HA, Zamora M, River JN, Rinker-Schaeffer C, Zaucha M, Tarlo K, Kellar K. Uptake of a superparamagnetic contrast agent imaged by MR with high spectral and spatial resolution. Magn Reson Med 2000;43:633–639.
3. Karczmar GS, Fan X, Al-Hallaq H, River JN, Tarlo K, Kellar KE, Zamora M, Rinker-Schaeffer C, Lipton MJ. Functional and anatomic imaging of tumor vasculature: high-resolution MR spectroscopic imaging combined with a superparamagnetic contrast agent. Acad Radiol 2002;9 Suppl 1:S115–118.
4. Karczmar GS, Du W, Medved M, Bick U, MacEneany P, Du YP, Fan X, Zamora M, Lipton M. Spectrally inhomogeneous effects of contrast agents in breast lesion detected by high spectral and spatial resolution MRI. Acad Radiol 2002;9 Suppl 2:S352–354.
5. Du W, Du YP, Bick U, Fan X, MacEneaney PM, Zamora MA, Medved M, Karczmar GS. Breast MR imaging with high spectral and spatial resolutions: preliminary experience. Radiology 2002;224:577–585.
6. Kovar DA, Al-Hallaq HA, Zamora MA, River JN, Karczmar GS. Fast spectroscopic imaging of water and fat resonances to improve the quality of MR images. Acad Radiol 1998;5:269–275.
7. Al-Hallaq HA, Zamora M, River JN, Karczmar GS. MR correctly predicts the relative effect of two tumor oxygenating agents on hypoxic fraction in rodent BA1112 tumors. In: Proc 7th Annual Meeting ISMRM, Philadelphia, 1999. p 496.
8. Oikawa H, Al-Hallaq HA, Lewis MZ, River JN, Kovar DA, Karczmar GS. Spectroscopic imaging of the water resonance with short repetition time to study tumor response to hyperoxia. Magn Reson Med 1997;38: 27–32.
9. Naritomi H, Kanashiro M, Sasaki M, Kuribayashi Y, Sawada T. In vivo measurements of intra- and extracellular Na+ and water in the brain and muscle by nuclear magnetic resonance spectroscopy with shift reagent. Biophys J 1987;52:611–616.
10. Zhong K, Li X, Shachar-Hill Y, Picart F, Wishnia A, Springer CSJ. Magnetic susceptibility shift selected imaging (MESSI) and localized (1)H(2)O spectroscopy in living plant tissues. NMR Biomed 2000;13: 392–397.
11. Doyle M, Mansfield P. Chemical shift imaging: a hybrid approach. Magn Reson Med 1987;5:255–261.
12. Mansfield P. Spatial mapping of the chemical shift in NMR. Magn Reson Med 1984;1:370–386.
13. Fan X, Du W, MacEneaney P, Zamora M, Karczmar G. Structure of the water resonance in small voxels in rat brain detected with high spectral and spatial resolution MRI. J Magn Reson Imag 2002;16:547–552.
14. Kovar DA, Karczmar GS. Fast spectroscopic imaging of water and fat proton resonances improves image contrast and signal-to-noise ratio. In: Proc 5th Annual Meeting ISMRM, Vancouver, 1997. p 1834.
15. Medved M, Du W, Zamora MA, Fan X, Olopade OI, MacEneaney PM, Newstead G, Karczmar GS. The effect of varying spectral resolution on the quality of HiSS MR images of the breast. J Magn Reson Imag 2003;18:442–448.
16. Kuperman V, River JN, Karczmar GS. High resolution spectroscopic images of tumors. In: Proc 3rd Annual Meeting ISMRM, Nice, 1995.
17. Sarkar S, Heberlein K, Metzger GJ, Zhang X, Hu X. Applications of high-resolution echoplanar spectroscopic imaging for structural imaging. J Magn Reson Imag 1999;10:1–7.
18. Brown TR, Kincaid BM, Ugurbil K. NMR chemical shift imaging in three dimensions. Proc Natl Acad Sci USA 1982;79:3523–3526.
19. Maudsley AA, Hilal SK, Perman WH, Simon HE. Spatially resolved high resolution spectroscopy by "four-dimensional" NMR. J Magn Reson 1983;51:147–152.

Magnetic Resonance in Medicine

What is RSS?

**Volume 49, Issue 6, Pages 1113-1120**

**Published Online:** 16 May 2003




Full Paper

# Reduction of spectral ghost artifacts in high-resolution echo-planar spectroscopic imaging of water and fat resonances

Weiliang Du [1], Yiping P. Du [2], Xiaobing Fan [1], Marta A. Zamora [1], Gregory S. Karczmar [1 *]

[1]Department of Radiology, University of Chicago, Chicago, Illinois

[2]Department of Psychiatry and Radiology, University of Colorado Health Sciences Center, Denver, Colorado

**email:** Gregory S. Karczmar (gskarczm@midway.uchicago.edu)

[*]Correspondence to Gregory S. Karczmar, Department of Radiology, MC 2026, University of Chicago, 5841 S. Maryland Ave., Chicago, IL 60637

**Funded by:**

- NCI; Grant Number: RO1CA75476, RO1CA78803
- Army Breast Cancer Research Program; Grant Number: DAMD 17-99-1-9121
- General Electric

**Keywords**

artifact • odd and even echoes • echo-planar spectroscopic imaging • spectral ghost artifacts • high spectral and spatial resolution imaging

**Abstract**

Echo-planar spectroscopic imaging (EPSI) can be used for fast spectroscopic imaging of water and fat resonances at high resolution to improve structural and functional imaging. Because of the use of oscillating gradients during the free induction decay (FID), spectra obtained with EPSI are often degraded by Nyquist ghost artifacts arising from the inconsistency between the odd and even echoes. The presence of the spectral ghost lines causes errors in the evaluation of the true spectral lines, and this degrades images derived from high-resolution EPSI data. A technique is described for reducing the spectral ghost artifacts in EPSI of water and fat resonances, using echo shift and zero-order phase corrections. These corrections are applied during the data postprocessing. This technique is demonstrated with EPSI data acquired from human brains and breasts at 1.5 Tesla and from a water phantom at 4.7 Tesla. Experimental results indicate that the present approach significantly reduces the intensities of spectral ghosts. This technique is most useful in conjunction with high-resolution EPSI of water and fat resonances, but is less applicable to EPSI of metabolites due to the complexity of the spectra. Magn Reson Med 49:1113-1120, 2003. © 2003 Wiley-Liss, Inc.

Received: 8 October 2002; Revised: 13 January 2003; Accepted: 6 February 2003

**Digital Object Identifier (DOI)**

10.1002/mrm.10485 About DOI

**Article Text**

The desire to shorten imaging time has stimulated the use of fast alternating gradients in many MRI methods. Echo-planar spectroscopic imaging (EPSI) uses an alternating readout gradient for simultaneous encoding of the chemical shift

dimension and one spatial dimension, and phase-encoding gradients for the other spatial dimensions. This strategy was first proposed by Mansfield ([1]) and has been successfully advanced by Posse et al. ([2][3]) and other workers for metabolite imaging ([4-9]), water and fat structural imaging ([10-14]), and functional imaging ([3][15][16]).

Compared to conventional phase-encoded spectroscopic imaging (SI), EPSI has the advantage of significantly reduced scan time; however, it places strong demands on the MR system, especially the gradient hardware. Inconsistency (i.e., discontinuity in magnitude and phase) between the odd and even echoes often arises because of the use of the echo-planar gradients. This effect is well known in echo-planar imaging (EPI). In EPI, the inconsistency causes Nyquist image ghosts in the phase-encoding dimension, since the odd and even echoes represent interlaced phase-encoded lines in *k*-space ([17]). Because the odd and even echoes encode the spectral dimension in EPSI, the signal inconsistency causes Nyquist ghosts in resulting spectra. The spectral ghosts are detrimental in two ways. First, the ghost peak of one true peak may appear on top of or near a second true peak, impeding accurate quantification of the latter peak and altering the lineshape. Second, the intensity of the true peak is reduced because of the "energy leakage" from the true peak to the ghost peak. The spectral ghosts are especially problematic when EPSI is used for high spectral and spatial (HISS) imaging ([10][11][16]) where the goal is to obtain detailed water and fat spectra for anatomic and functional imaging.

A number of techniques have been proposed for the reduction of spectral ghost artifacts. One widely used and effective method is to separate the odd and even echoes in data processing ([2][13][15]). Unfortunately, this sacrifices half of the spectral bandwidth, which is already small in high spatial resolution EPSI. Alternatively, the odd and even echoes are combined for processing using the interlaced Fourier transform method ([6]) or the Fourier shift method ([18]). These techniques address the issue of nonuniform temporal sampling arising from the evolution of the free induction decay (FID) during each gradient echo. With these approaches, it is implicitly assumed that data are precisely sampled along a theoretically determined trajectory in *k*-*t*-space. In other words, the odd and even echoes are properly aligned and no corrections are made to the data at the center of *k*-space. In practice, this assumption is often invalid. Echo misalignments and distortions often lead to Nyquist ghosts in images obtained with EPI ([17]), and should be accounted for. Corrections for echo misalignment have been developed for EPSI by measuring the *k*-*t* trajectory and interpolating data at the desired locations ([6][13]). The main drawback of this method is the complicated procedure required for *k*-*t* trajectory measurement.

In this article, we present a new method to reduce the spectral ghost artifacts in EPSI by correcting the echo misalignment and phase discontinuities between the odd and even echoes. This approach is conceptually an extension of the echo shifting and phase correcting method that has been effective in removing inconsistency between the odd and even echoes for EPI data ([17]). The echo misalignment is corrected by shifting the "centers of mass" (CM) of the odd and even echoes, and a zero-order phase correction is then applied to the odd echoes to minimize the spectral ghost intensity. This method takes advantage of the high SNR signals at the *k*-space center to measure inconsistencies in position and phase between the odd and even echoes. All corrections are made during data postprocessing, i.e., without the need for additional reference scans.

This technique has been applied to high spatial resolution EPSI data obtained from human brains and breasts at 1.5 Tesla, and from a water phantom at 4.7 Tesla. The MR images were acquired using an EPSI sequence without water or fat suppression. Water and fat spectra obtained with the present method and the conventional FFT method were compared to demonstrate the effectiveness of the new method.

## MATERIALS AND METHODS

### Data Acquisition

#### EPSI Pulse Sequence

The EPSI pulse sequence we implemented was a gradient-recalled multiecho sequence with 64 or 128 gradient echoes excited along the *x* dimension using trapezoidal readout gradients. The second spatial dimension (*y*) was provided by phase-encoding gradients between excitation and detection.

To provide sufficient spectral bandwidth, we collected the EPSI data in multiple ($N_{int}$) acquisitions. In each acquisition (or interleaf) the temporal offset of the echo train from the excitation pulse was incremented by $\Delta$t. This effectively reduced the time interval between adjacent gradient echoes (i.e., echo spacing, or $T_{esp} = N_{int}\Delta t$), and thus increased the spectral bandwidth by a factor of $N_{int}$.

#### Phantom Studies

Phantom experiments were performed on a 4.7 Tesla magnet (Omega; GE/Bruker, Fremont, CA). The phantom was a bottle of copper sulfate solution with an inner diameter of 24 mm. EPSI scans were performed through a 1-mm-thick axial slice with an in-plane resolution of 0.38 × 0.38 $mm^2$ and a field of view (FOV) of 48 mm. The readout gradient consisted of 64 alternating lobes, each of which had two linear ramps (0.5 ms each) and a plateau (3.2 ms). Data were sampled only during the plateau phase of the gradient. The echo train lasted for 270 ms, yielding spectral resolution of 3.7 Hz.

Interleaved EPSI datasets ($N_{int}$ = 2) were acquired with an echo train offset of 2.1 ms so that the combination of the two interleaves resulted in a spectral bandwidth of 473 Hz. Each EPSI interleaf was acquired in 128 s (TR = 1 s).

### Human Studies

Healthy volunteers were imaged on a 1.5 Tesla MR scanner (Signa; GE Medical Systems, Milwaukee, WI), following a protocol approved by the University of Chicago Institutional Review Board. EPSI images were obtained in an axial slice through the brains ($N$ = 8) or in a sagittal slice through the breasts ($N$ = 2, female). Imaging parameters were: TR = 500 ms, sampling bandwidth = ±62.5 kHz, slice thickness = 4 mm, FOV = 24 cm, spectral bandwidth = 333 Hz, matrix size = 256 ($x$) × 256 ($y$) 128 (f), and $N_{int}$ = 1. The EPSI scan was acquired in 128 s.

### Postprocessing

#### Echo Misalignment

In an ideal EPSI experiment, the center of $k$-space (i.e., the $k_x$ = 0 point) is traversed repeatedly with a constant time interval (Fig. 1a). Because of the opposite directions of the trajectories along $k_x$ caused by the alternating readout gradients, the odd (or even) echoes must be reversed during data processing; however, the alignment of the $k_x$ = 0 points does not change in the ideal situation. Two types of echo misalignments occur in practice due to various scanner- or sample-related imperfections. In the first type (Fig. 1b), the echo train is temporally shifted relative to the start of data acquisition, due to system timing errors, imperfection of gradient hardware ([6][13]), and uncompensated eddy currents ([19][20]). The reversal of the odd echoes translates this temporal shift in the echo train into a relative misplacement along $k_x$ between the odd and even echoes. This misplacement generates spectral ghost artifacts when the echoes are used to produce spectra. In the second type of echo misalignment (Fig. 1c), the odd and even echoes are unevenly spaced within the echo train. This misalignment may be due to background gradients resulting from improper shimming, local susceptibility inhomogeneity, and eddy currents ([21]), or to an inaccurate dephasing gradient applied along $k_x$ before the alternating readout gradients. As a result, the FID signals are not uniformly sampled at all $k$-space positions, including the $k_x$ = 0 point, which introduces apparent magnitude and phase discontinuities between the odd and even samples, and thus generates spectral ghosts.

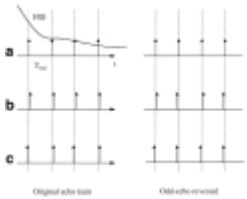


**Figure 1. Misalignment of the gradient echoes before (left) and after (right) the reversal of the odd echoes. The short arrows indicate the position of $k_x$ = 0 point in each echo. a: Ideal alignments. b: A temporal shift of the entire echo train. c: Uneven spacing between adjacent echoes.**
**[Normal View 8K | Magnified View 18K]**

#### Echo Shift Correction

Previous EPSI studies either assumed an ideal echo misalignment ([18]) (i.e., no corrections are made to signals at $k$-space center) or corrected the first type of echo misalignment described above based on a predetermined $k$-space trajectory ([6][13]). In this study we corrected for the first type of echo misalignment by shifting the positions of the odd and even echoes using the information derived from the EPSI data itself. The raw data in the form of echo trains were grouped into a 3D signal matrix, $S(k_x, k_y, n)$, where $n$ indexed the echoes (0, 1, 2, . . .) in the echo train and the odd echoes ($n$ = 1, 3, . . .) were reversed. Then the $k$-space center ($k_x$ = 0, $k_y$ = 0) was approximated as the CM of the $k$-space signals for each echo, using the following formula:

$$CM_{kx}(n) = \frac{\sum_{k_x,k_y} k_x \cdot |S(k_x, k_y, n)|}{\sum_{k_x, k_y} |S(k_x, k_y, n)|} \quad (1)$$

$$CM_{ky}(n) = \frac{\sum_{k_x,k_y} k_y \cdot |S(k_x, k_y, n)|}{\sum_{k_x, k_y} |S(k_x, k_y, n)|},$$

The differences between the CMs of the first five even echoes and the CMs of the immediately adjacent five odd echoes (after reversal of odd echoes) were calculated and averaged. These echoes were used because of their relatively high signal-to-noise ratio (SNR). Half of the averaged difference was used to shift the original echo train (i.e., before the odd echoes were reversed). Shifts that were smaller than one data point were performed using the Fourier shift theorem (i.e., data were Fourier transformed, a linear phase term was added, and then data were inversely Fourier transformed). The shifted echo train data were then regrouped into the matrix $S(k_x, k_y, n)$ for further processing.

### Phase Correction

Echo misalignment of the second type described above led to nonuniform sampling of FID signals at all *k*-space points. Instead of assuming a uniform sampling at $k_x = 0$ and correcting the phases of the signals at other *k*-space points ([6][18]), we used a constant phase factor to correct for the phases of the odd echo signals at all *k*-space points. The phase factor was derived from the EPSI data itself, as follows:

1. For each echo *n*, the middle point (presumably, $k_x = k_y = 0$) of the signal matrix *S* was extracted. A function, named $FID_{k00}(n)$, was formed with the extracted samples and was Fourier transformed. In the EPSI data from water phantom and human brains, two peaks arose in the resulting spectrum that were exactly half of the spectral bandwidth apart. The peak with larger magnitude was identified as the "true" water peak, while the other peak was regarded as the "ghost" peak. In the case of breast EPSI, the resulting spectrum often consisted of a relatively strong fat peak, a relatively strong water peak ~216 Hz away (~3.4 ppm) from the fat peak, and two smaller peaks located half of the spectral bandwidth away from the fat peak and the water peak, respectively. We picked the peak with the largest magnitude (either the fat peak or the water peak) as the "true" peak, and the peak at half of spectral bandwidth away from this peak as the "ghost" peak.
2. The magnitudes of the true peak and the ghost peak were quantified as a summation of spectral intensities over a narrow neighborhood (e.g., 3-5 bins wide). Baseline was removed prior to the spectral summation, by subtracting a smoothed spectrum (boxcar length of ~15 bins) from the original spectrum. The ratio of the magnitude of the ghost peak to the magnitude of the true peak is herein referred to as the "ghost-to-true ratio" (GTR).
3. A phase angle $\phi$ was chosen from the range ($-\pi$, $\pi$). A phase term $e^{-j2\pi\phi}$ was multiplied to the signals of the odd echoes at all *k*-space points. Steps 1 and 2 were repeated and the GTR was reevaluated.
4. The amount of phase correction was found using a Golden Section algorithm such that GTR was minimized.

### Interleaved Acquisition

The correction methods described above were also extended to correct for the global phase changes in interleaved EPSI data. Each interleaf was treated separately with the echo shift and phase corrections described above. Then the interleaves were combined and a zero-order phase correction was applied to each interleaf (i.e., all echoes in that interleaf) except the first interleaf, in order to force the phase of every interleaf to be consistent with the first one. This zero-order phase correction was similar to the phase correction described above, except that the minimization problem in step ([4]) became multidimensional ($N_{int}$-1). An IDL (Research Systems, Boulder, CO) routine employing the Powell's minimization algorithm was used in this task.

### Method Evaluation

The EPSI spectrum in each pixel was obtained with a 3DFT following the echo shift and phase corrections. Images were formed with intensities proportional to the magnitude of the true peak, the magnitude of the ghost peak, and their ratio (GTR) using uncorrected and corrected spectra in each pixel. These variables were also reported quantitatively. To take the variation of these variables across the image into account, we pooled the measurements from all pixels with maximum spectral intensity 10 times above the noise level. Since these variables (e.g., GTR) did not necessarily follow a Gaussian distribution, we reported the median of pooled data along with the 20% and 80% quantiles as an estimate of the range of the measured variables.

## RESULTS

### Phantom

The CM calculated from the phantom EPSI data exhibits oscillatory displacements between the odd and even echoes in the readout ($k_x$) direction (Fig. 2a). Oscillation in CM is not seen in the phase-encoding ($k_y$) direction in the same EPSI data. Conventional phase-encoded SI (i.e., no readout gradients) of the same slice under the same shim conditions shows similar overall trends of CM shifts, but no oscillatory pattern in either the $k_x$ or the $k_y$ dimensions. This excludes the possibility that the relative echo shift in the readout direction ($k_x$) is due to the nature of the imaged object, or to off-resonance effects such as background gradients. The echo misalignment is evidently related to the alternating readout gradient and relevant data acquisition. A temporal offset (66 μs, or 2.65 data points) was used for the echo shift correction. As a result, the CM of the corrected EPSI data shows a reduced amplitude of oscillation and approaches the CM obtained with the conventional SI data (Fig. 2a). Also, the shape of the corrected $FID_{k00}$ shows much better agreement with the $FID_{k00}$ measured with the conventional SI (Fig. 2b).

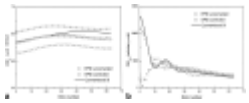

**Figure 2. Echo shift correction in EPSI data obtained from a water phantom. a: $CM_{kx}$ (defined in Methods) as a function of the index of the echoes in uncorrected EPSI (cross), EPSI with echo shift correction (circle), and conventional phase-encoded SI (solid line). b: The magnitude of $FID_{k00}$ from uncorrected EPSI, corrected EPSI, and**

**conventional SI.**
**[Normal View 14K | Magnified View 37K]**

For the first interleaf of the phantom EPSI data, the GTR was minimized with a phase correction of $\phi$ = 40.7°. For the second interleaf, the GTR was minimized with $\phi$ = 41.8°. To combine the two interleaves, a phase correction of 0° was found to be necessary to correct for all echoes from the second interleaf. Nonzero phase corrections were made to the interleaves in other EPSI scans (data not shown here).

The EPSI data were also reconstructed without echo shift and phase corrections. A true water peak and three ghost peaks were found in the uncorrected spectra from most pixels. Figure 3 shows images synthesized from the peak height of the true water peak and the peak heights of the ghost peaks. Bright and dark streak patterns are evident in all uncorrected images. Where the signal intensity is strong in the ghost peaks (areas of hyperintensity in b, c, and d), the signal intensity is weak in the true water peak (areas of hypointensity in a). These artifacts are removed in the corrected peak height image (e). The intensities of the ghost peaks drop substantially (b vs. f, c vs. g, d vs. h) as the intensities of the true peaks increase (a vs. e), especially in pixels that originally had strong spectral ghosts. Table 1 summarizes the reduction of spectral ghosts in one- and two-interleaf EPSI datasets obtained with the water phantom.

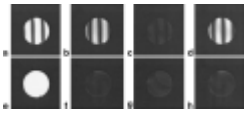

**Figure 3. Images synthesized from interleaved ($N_{int}$ = 2) EPSI data without (upper panels) and with (lower panels) echo shift and phase corrections. From left to right, image intensity is proportional to the magnitude of the spectral peak at $f_0$ (a ande), $f_0 + bw/4$ (b andf), $f_0 + bw/2$ (c andg), and $f_0 + bw \cdot 3/4$ (d andh), where $bw$ is the spectral bandwidth, $f_0$ is the frequency of the true water peak. The alternating readout gradient was applied in the horizontal direction.**
**[Normal View 17K | Magnified View 78K]**

**Table 1. Reduction of the Spectral Ghost Peaks With the Echo Shift Correction and/or Phase Correction in EPSI Scans of a Water Phantom at 4.7 T***

| | One-interleaf EPSI | | | | Two-interleaf EPSI | |
|---|---|---|---|---|---|---|
| | Uncorrected | Echo shift correction only | Phase correction only | Echo shift and phase correction | Uncorrected | Echo shift and phase correction |
| Magnitude of true peak | 3.40 (1.22, 5.01) | 4.93 (4.76, 5.31) | 3.46 (1.19, 5.13) | 5.26 (5.09, 5.64) | 4.31 (1.66, 6.22) | 6.36 (6.17, 6.75) |
| Magnitude of ghost peak | 3.65 (1.30, 5.15) | 1.38 (1.11, 1.61) | 3.63 (1.32, 5.08) | 0.15 (0.06, 0.24) | 2.14 (0.94, 2.84) | 0.22 (0.17, 0.31) |
| Ghost-to-true ratio[a] | 1.05 (0.25, 4.31) | 0.28 (0.23, 0.32) | 1.03 (0.25, 4.07) | 0.027 (0.011, 0.046) | 0.49 (0.15, 1.76) | 0.035 (0.027, 0.048) |

*** The data presented are 50% (i.e., median) and 20%, 80% quantiles (in parenthesis) of the measurements obtained over an ROI covering most area of the phantom.**

**[a] Ghost-to-true ratio is defined as the ratio of magnitude of the ghost peak to the magnitude of the true water peak (also see Materials and Methods).**

Human Brain and Breast

Figure 4 demonstrates the effectiveness of the correction method on the EPSI data obtained from human brain. The ghost peaks are reduced to noise level in all pixels. The magnitudes of the true water peak increase nonuniformly across the image after the corrections. The increase is relatively large at locations where the spectral ghost is strong (near the edges of the brain). Table 2 shows the quantitative results of spectral ghost reduction. The EPSI datasets are corrected with an echo shift of approximately 0-7 μs and a zero-order phase of approximately -4° to 2°. The median of GTR before correction ranges from 2.4% (volunteer 5) to 27% (volunteer 2), with an average of approximately 12%. After the corrections, the median of GTR decreases to between 2% and 5%, with an average of 3.5%. The original GTRs are large in volunteers 2 and 4; therefore, the corrections are relatively large and lead to a remarkable decrease (sixfold) in the GTR.

The original GTR is small in volunteer 5 and is not reduced after corrections.

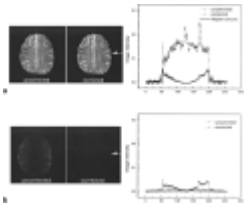

**Figure 4. Reduction of spectral ghosts in EPSI data of human brain. Image intensity is proportional to the magnitudes of the true water peak (a) or the ghost peak (b). All images are displayed with an identical windowing setting. On the right are profiles of the image intensities through a horizontal line indicated by the arrows.**
**[Normal View 46K | Magnified View 164K]**

**Table 2. Echo Shift Correction, Zero-Order Phase Correction, and Reduction of Spectral Ghost Peaks in EPSI Scans of Normal Human Brains at 1.5T***

| Volunteer | Echo train shift in time (μs) | Phase correction on odd echoes (degree) | Ghost-to-true ratio | |
|---|---|---|---|---|
| | | | Uncorrected | Corrected |
| 1 | 3.6 | -0.34 | 0.099 (0.032, 0.204) | 0.019 (0.012, 0.028) |
| 2 | 6.0 | -2.09 | 0.268 (0.093, 0.561) | 0.041 (0.025, 0.065) |
| 3 | 2.7 | -3.46 | 0.095 (0.049, 0.191) | 0.049 (0.034, 0.068) |
| 4 | 6.7 | -1.98 | 0.212 (0.077, 0.411) | 0.035 (0.022, 0.065) |
| 5 | 0.2 | 1.68 | 0.024 (0.013, 0.039) | 0.027 (0.015, 0.041) |
| 6 | 2.8 | 0.00 | 0.091 (0.049, 0.179) | 0.047 (0.032, 0.065) |
| 7 | 4.7 | 1.59 | 0.105 (0.041, 0.213) | 0.036 (0.023, 0.054) |
| 8 | 2.5 | 1.62 | 0.053 (0.029, 0.106) | 0.028 (0.019, 0.040) |

*** The data presented are 50% (i.e., median) and 20%, 80% quantiles (in parenthesis) of the measurements obtained over an ROI covering most area of the brain.**

The reduction of spectral ghosts in the EPSI data of human breast is illustrated in Fig. 5. In pixel 1 (which contains approximately equal amounts of fat and water tissues), the uncorrected spectrum clearly shows a ghost peak from the fat resonance and a weak ghost peak from the water resonance. In pixel 2 (which contains primarily fat), a single ghost peak is seen in the uncorrected spectrum. The magnitudes of the ghost peaks in these pixels are reduced to noise level after the corrections. Although spectra from many pixels in the breast, such as those shown in Fig. 5, were greatly improved by the correction, spectral ghosts in some pixels were not attenuated. Thus, the method in its current form is not as robust in the breast, where fat and water signals are present, as it is in the brain, where only the water peak is significant.

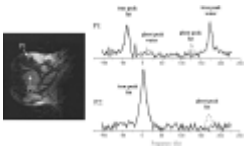

**Figure 5. Reduction of spectral ghosts in EPSI data of human breast. Left: An EPSI peak height image. Right: Spectra from two selected pixels (P1 and P2 in the image) calculated with (solid) and without (dash) echo shift and phase corrections.**
**[Normal View 31K | Magnified View 106K]**

## DISCUSSION

In the present work, a method for reducing spectral ghosts in EPSI of water and fat resonances is demonstrated. This method uses the EPSI data from the center of *k*-space to correct the relative misplacement and zero-order phase difference between the odd and even echoes. In contrast to the commonly used technique that separates the odd and even echoes for image reconstruction, the present method removes the ghost peaks without reducing the spectral

bandwidth to half. The savings on spectral bandwidth is particularly important for high spatial resolution EPSI applications, where the spectral bandwidth is usually limited by a relatively long duration of each gradient echo. Compared to other techniques that measure *k*-space trajectories to determine echo misalignments, the corrections are made during data processing, i.e., without the need for additional scans. This technique can be readily implemented with various EPSI sequences, such as 3D EPSI ([9]) and multishot EPSI ([22]).

EPSI data obtained without corrections display an interesting pattern of spectral ghost artifacts. The relative magnitudes of the ghost peaks vary significantly with respect to position in the echo-planar readout (*x*) direction, but do not vary as much in the phase-encoding direction (Figs. 3 and 4). The change in the ghost magnitude reflects a spatial variation in the extent of inconsistency between the odd and even echoes in the *x* direction, due to complicated echo shifts and distortions in the $k_x$ direction. The inconsistency is severe at locations where large background gradients are present (e.g., near the edges of the brain in Fig. 4). Therefore, a global phase shift cannot by itself remove the artifacts from all pixels. In this work, the zero-order phase correction is used in combination with an echo shift correction. According to the Fourier theorems, an echo shift correction in the $k_x$ direction is equivalent to a linear or first-order phase correction in the *x* direction. In essence, the echo shift correction is an extension of linear phase correction ([17]), which is widely used in EPI for removing image ghosts, to the task of removing spectral ghosts in EPSI. A nonlinear phase correction may better compensate for the effects of static field inhomogeneity on the data inconsistency, but it demands additional reference scans ([17]) and/or more sophisticated data processing techniques.

The zero-order phase correction is performed after the echo shift correction, i.e., after the linear phase discontinuity along the *x* direction is removed and only a residual constant phase discontinuity is left between the odd and even echoes. Despite its simplicity, the zero-order phase correction is effective: ghost intensity decreased from 0.28 to 0.027 in the water phantom experiments (see Table 1). The residual spectral ghosts are probably due to the fact that the phase evolution of the FID during each gradient echo is neglected in this study. During the echo-planar readout, the $k_x$-*t*-space is traversed in a zigzag fashion. Therefore, the sampling in time is not uniform for most of *k*-space points. This can generate spectral ghost artifacts. In the presence of a large off-resonance effect, it is necessary to make phase corrections for each *k*-space point ([6][18]). In our EPSI implementations for imaging water resonance in the phantom and human brains, the off-resonance effect is reasonably small. This is supported by the observation of the negligible magnitudes of residual ghost peaks after echo-shifting and phase correction (Fig. 4b). Further, the present method was also demonstrated to be useful for data acquired with interleaved EPSI. As with other multishot techniques ([23][24]), the signal varies from one acquisition to another. The zero-order phase correction provides a "self-navigated" way to trace and correct for the phase drift in the interleaved EPSI data.

The present method was developed for high-resolution functional and anatomic imaging of water and fat; therefore, it is more difficult to apply this method to water- and fat-suppressed EPSI of metabolites. First, the method may be sensitive to the noise in the data because of the low SNR nature of metabolite imaging. Second, multiple chemical shifts change the signal patterns in *k*-space. As a result, the determination of the *k*-space center using the CM technique may not be accurate. Third, the ghost from one true line may overlap another true line. In this case, it becomes difficult to minimize the ghost intensity using the method described above. Finally, a constant phase correction that minimizes the ghost from one true line may not reduce the ghosts from other lines. Despite these limitations, the correction still works well on the high-resolution EPSI data obtained from human breast (Fig. 5). With the current implementation, the correction is applied directly to the water/fat EPSI data. For metabolite EPSI, it might be possible to calculate the amount of correction from a reference scan in which water signal is not suppressed. Then the correction could be applied to the metabolite EPSI data, assuming that the inconsistency between the odd and even echoes is accurately measured with the reference scan. This hypothesis was not validated in this work, and requires further investigation.

It is interesting to note that significantly larger echo shift and phase corrections are necessary for the EPSI data obtained at 4.7 T compared to 1.5 T. Thus, the correction is more beneficial for the 4.7 T data. This is probably because of a relatively better performance of echo-planar gradients and relatively smaller background gradients on the lower field. The results from EPSI measurements may be used to characterize the system inaccuracies and eddy-current effects for EPI applications ([25][26]). For example, the oscillatory pattern of the CM of the gradient echoes is a sensitive indicator of system timing errors (Fig. 2a). In addition, the linear or nonlinear trend in the CM may be used to guide adjustment of shims to reduce background gradients.

In conclusion, a new method for reducing spectral ghost artifacts in EPSI of water and fat resonances is presented. This method uses an echo shift and zero-order phase correction to remove the inconsistency between the odd and even echoes. The spectral ghost artifacts are reduced significantly, as demonstrated in phantom and in vivo EPSI of water and fat resonances at 1.5 T and 4.7 T. A further reduction of spectral ghosts in EPSI is expected when this technique is combined with other reconstruction strategies, such as nonlinear phase correction ([17]) and interlaced Fourier transform ([6][18]).

**References**

1 Mansfield P. Spatial mapping of the chemical shift in NMR. *Magn Reson Med* 1984; **1**: 370-386. Links

2 Posse S, Tedeschi G, Risinger R, Ogg R, Le Bihan D. High speed 1H spectroscopic imaging in human brain by echo planar spatial-spectral encoding. *Magn Reson Med* 1995; **33**: 34-40. Links

3 Posse S, Dager SR, Richards TL, Yuan C, Ogg R, Artru AA, Muller-Gartner HW, Hayes C. In vivo measurement of regional brain metabolic response to hyperventilation using magnetic resonance: proton echo planar spectroscopic imaging (PEPSI). *Magn Reson Med* 1997; **37**: 858-865. Links

4 Matsui S, Sekihara K, Kohno H. Spatially resolved NMR spectroscopy using phase-modulated spin-echo-trains. *J Magn Reson* 1986; **67**: 476-490. Links

5 Webb P, Spielman D, Macovski A. A fast spectroscopic imaging method using a blipped phase encode gradient. *Magn Reson Med* 1989; **12**: 306-315. Links

6 Metzger G, Hu X. Application of the interlaced Fourier transform to echo-planar spectroscopic imaging. *J Magn Reson* 1997; **125**: 166-170. Links

7 Hyder F, Renken R, Rothman DL. In vivo carbon-edited detection with proton echo-planar spectroscopic imaging (ICED PEPSI): [3,4-(13)CH(2)]glutamate/glutamine tomography in rat brain. *Magn Reson Med* 1999; **42**: 997-1003. Links

8 Richards TL, Corina D, Serafini S, Steury K, Echelard DR, Dager SR, Marro K, Abbott RD, Maravilla KR, Berninger VW. Effects of a phonologically driven treatment for dyslexia on lactate levels measured by proton MR spectroscopic imaging. *Am J Neuroradiol* 2000; 21. Links

9 Ebel A, Soher BJ, Maudsley AA. Assessment of 3D proton MR echo-planar spectroscopic imaging using automated spectral analysis. *Magn Reson Med* 2001; **46**: 1072-1078. Links

10 Du W, Du YP, Bick U, Fan X, MacEneaney PM, Zamora MA, Medved M, Karczmar GS. High spectral and spatial resolution MR imaging of breast - preliminary experience. *Radiology* 2002; **224**: 577-585. Links

11 Kovar DA, Al-Hallaq HA, Zamora MA, River JN, Karczmar GS. Fast spectroscopic imaging of water and fat resonances to improve the quality of MR images. *Acad Radiol* 1998; **5**: 269-275. Links

12 Kuroda K, Mulkern RV, Oshio K, Panych LP, Nakai T, Moriya T, Okuda S, Hynynen K, Joles FA. Temperature mapping using the water proton chemical shift: self-referenced method with echo-planar spectroscopic imaging. *Magn Reson Med* 2000; **43**: 220-225. Links

13 Sarkar S, Heberlein K, Metzger GJ, Zhang X, Hu X. Applications of high-resolution echoplanar spectroscopic imaging for structural imaging. *J Magn Reson Imaging* 1999; **10**: 1-7. Links

14 Yang QX, Demeure RJ, Dardzinski BJ, Arnold BW, Smith MB. Multiple echo frequency-domain image contrast: improved signal-to-noise ratio and T2 (T2*) weighting. *Magn Reson Med* 1999; **41**: 423-428. Links

15 Barth M, Reichenbach JR, Venkatesan R, Moser E, Haacke EM. High-resolution, multiple gradient-echo functional MRI at 1.5 T. *Magn Reson Imaging* 1999; **17**: 321-329. Links

16 Du YP, Du W, Uftring SJ, Fan X, Karczmar GS. fMRI with high spectral and spatial resolution echo-planar spectroscopic imaging at 1.5T. In: Proceedings of the 9th Annual Meeting of ISMRM, Glasgow, Scotland, 2001. p 1254.

17 Bruder H, Fischer H, Reinfelder HE, Schmitt F. Image reconstruction for echo planar imaging with nonequidistant *k*-space sampling. *Magn Reson Med* 1992; **23**: 311-323. Links

18 Hanson LG, Schaumburg K, Paulson OB. Reconstruction strategy for echo planar spectroscopy and its application to partially undersampled imaging. *Magn Reson Med* 2000; **44**: 412-417. Links

19 Takahashi A, Peters T. Compensation of multi-dimensional selective excitation pulses using measured *k*-space trajectories. *Magn Reson Med* 1995; **34**: 446-456. Links

20 Haacke EM, Brown RW, Thompson MR, Venkatesan R. *Magnetic resonance imaging: physical principles and sequence design*. New York: John Wiley and Sons; 1999. p 846-848.

21 Jezzard P, Barnett AS, Pierpaoli C. Characterization of and correction for eddy current artifacts in echo planar diffusion imaging. *Magn Reson Med* 1998; **39**: 801-812. Links

22 Tyszka JM, Mamelak AN. Volumetric multishot echo-planar spectroscopic imaging. *Magn Reson Med* 2001; **46**: 219-227. Links

23 Hu X, Kim SG. Reduction of signal fluctuation in functional MRI using navigator echoes. *Magn Reson Med* 1994; **31**: 495-503. Links

24 Glover GH, Lai S. Self-navigated spiral fMRI: interleaved vs. single-shot. *Magn Reson Med* 1998; **39**: 361-368. Links

25 Chen NK, Wyrwicz AM. Correction for EPI distortions using multi-echo gradient-echo imaging. *Magn Reson Med* 1999; **41**: 1206-1213. Links

26 Schmithorst VJ, Dardzinski BJ, Holland SK. Simultaneous correction of ghost and geometric distortion artifacts in EPI using a multiecho reference scan. *IEEE Trans Med Imaging* 2001; **20**: 535-539. Links